



UNIVERSITY OF MESSINA

DEPARTMENT OF ENGINEERING

PHD IN ENGINEERING AND CHEMISTRY OF MATERIALS AND CONSTRUCTION

XXXIV CYCLE

**SYNTHESIS AND CHARACTERIZATION OF BIOMATERIALS
FOR ENGINEERING APPLICATIONS**

**PHD THESIS OF:
CONSUELO CELESTI**

**TUTOR:
PROF.SSA ANNAMARIA VISCO**

**CO-TUTOR:
PROF. ALESSANDRO PISTONE**

**HEAD OF THE PH.D. COURSE:
PROF. GIOVANNI NERI**

2018-2021

TABLE OF CONTENTS

Abstract	I
1. Introduction	1
1.1 Biomaterials	1
1.1.1 Absorbable polymers and their applications	4
1.1.2 Non absorbable polymers and their applications	8
1.2 Outline of Thesis	12
References	16
2. Carbon-based nanomaterials for drug delivery	20
2.1 Methods for the synthesis of GQDs	24
2.2 Application of GQD in drug delivery	28
3. Chitosan-based hydrogel for tissue engineering	41
3.1 Characteristics of an ideal scaffold	45
3.2 Applications in tissue engineering	48
References	56
4. Coatings against Marine Fouling	65
4.1 Homogenous surfaces	72
4.2 Heterogeneous surfaces	78
References	84
5. Results And Discussion	91
5.1 Synthesis and characterization of an smart nanovector for cancer-targeted drug delivery based on Graphene Quantum Dots	93
5.1.1 Characterizations	95

TABLE OF CONTENTS

5.2 Synthesis and characterization of Eco-Friendly 1,3-Dipolar Cycloaddition Reactions on Graphene Quantum Dots in Natural Deep Eutectic Solvent	103
5.2.1 Characterizations	104
5.3 Synthesis and characterization of Chitosan-Hydroxyapatite-Magnetite Hierarchical Scaffolds	111
5.3.1 Characterizations	112
5.4 Synthesis and characterization of Chitosan/PAMAM/Hydroxyapatite	120
5.4.1 Characterizations	121
5.5 Synthesis and characterization of functionalized polyhedral oligosilsesquioxane (POSS) based on Chitosan	132
5.5.1 Characterizations	134
5.6 Effect of propionaldehyde and lauraldehyde on APTES-based protective coatings.	139
5.6.1 Characterizations	140
5.7 Effect of glutaraldehyde on APTES based protective coatings.	157
5.7.1 Characterizations	157
6. Conclusions And Future Remarks	170
7. Experimental Section	175

ABSTRACT

The main objective of my PhD work was to study several classes of next-generation biomaterials, which are materials designed and developed to interact with biological systems, as they are bioactive and compatible with human tissue, and show a good degree of biodegradability. They are eco-friendly, renewable, and non-polluting and find use in medicine, tissue engineering, biosensors and virus detection. Specifically, this PhD thesis is divided into three sections, based on the materials studied, which find their applications in the biomedical and environmental fields.

The first section refers to the development of carbon-based nanomaterials for drug delivery. In detail, graphene quantum dots (GQD), the last member of the graphene family have been investigated as drug delivery systems for anticancer therapy. Their strong size-dependent photoluminescence and the presence of many reactive groups on the surface of the graphene surface allowed their multimodal conjugation with therapeutic agents and targeting ligands, making them valuable agents for innovative targeted therapies for cancer treatment.

The second section is focused on the development of new synthetic hydrogels based on chitosan useful for the tissue regeneration. Tissue engineering is an important therapeutic strategy for present and future medicine. The goal is to restore, regenerate, maintain, or improve function in defective tissue or lost tissue due to different disease conditions. The use of novel biodegradable and bioresorbable chitosan-based hydrogel formulations for controlled drug delivery has enabled the development of biocompatible biopolymer scaffolds that can promote tissue regeneration.

The third section concerns the design of eco-friendly and innovative antifouling coatings. Marine biofouling generally refers to the undesirable accumulation of biological organisms on surfaces in contact with seawater. This natural phenomenon represents a major economic concern for marine industries, and in the last few decades, many efforts have been spent into developing efficient antifouling (AF) surfaces (coatings) combining advances in materials science and recent knowledge of marine chemistry and biology. In this context, polysiloxanes with controlled hydrophilicity represent a valuable and environmentally friendly alternative to currently used marine coating.

1. INTRODUCTION

1.1 Biomaterials

Biomaterials are in general engineered materials able to interact with biological systems for applications in in different fields encompassing biology, medicine, environmental and material science. Their goal is twofold: the improvement of knowledge about the functioning of biological systems and the development of new diagnostic, therapeutic and rehabilitative methodologies and devices as well as new biocompatible and eco-friendly substrates.

The use of biomaterials has a long history. One of the earliest examples is a wood-and-skin prosthesis found on an Egyptian mummy 3,000 years ago. It has evolved over the years in response to advances in science and technology. Throughout history, humans have made increasingly effective devices to diagnose and treat disease and to relieve, rehabilitate or compensate for disability or injury. They are often biodegradable and some are bioabsorbable, meaning they are gradually eliminated from the body after performing a function.[1]

To date, they have entered our daily lives through a variety of application areas, from the proliferation of implantable medical devices, such as pacemakers and artificial limbs, to more futuristic technologies such as stem cell engineering and 3D printing of biological organs, to diagnostic and monitoring devices. (Fig. 1)

Biomaterials can be classified by considering their chemical nature, thus one can distinguish between: [2]

- Metallic; iron-based and non-iron-based alloys or other more or less pure metals (Titanium)
- Ceramics; metal oxides produced in powder or glass form
- Organic; synthetic or natural macromolecules.

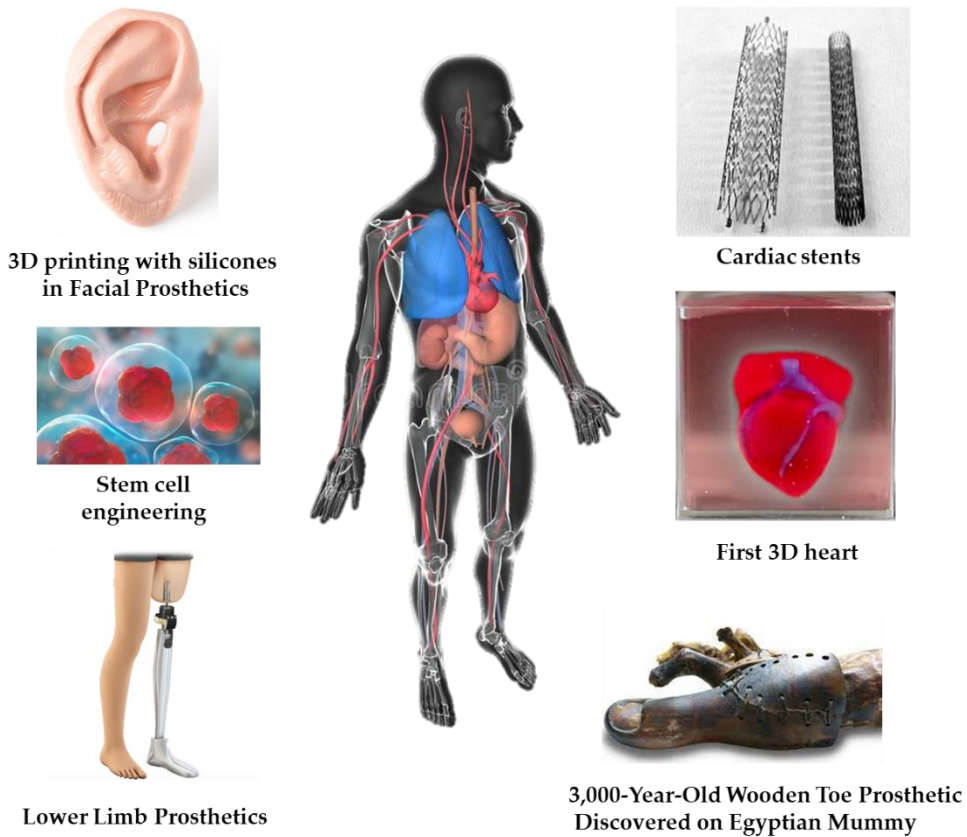


Figure 1. Biomaterials Development

All of these classes have found, and still find, a wide range of application, for many years, and industrial and academic efforts have been made in this exciting field of research.

Despite great success in a variety of biomedical applications, the design of such implantable devices is not yet fully optimal. This interdisciplinary research area ranges from physics and chemistry through molecular biology

engineering to medicine. The unifying property of biomaterials is biocompatibility. The commonly cited definition of biocompatibility was granted by the European Society for Biomaterials in 1986 as *"The ability of a material to function with an appropriate host response in a specific application"* [3]. An example of biocompatibility is that of orthopedic joint replacements. Traditional titanium joint replacement is considered biocompatible because it does not cause toxicity by replacing joint function. The ultimate goal of biocompatible materials, in the field of regenerative medicine, is to reconstruct any tissue or organ in situ from scratch. For example, optimal joint replacement would temporarily replace joint function, and over time degrade while being replaced by new healthy host-formed bone tissue.

Among these different classes of polymers, the large family of biopolymers is of great interest in the field of tissue engineering because of their biodegradability, osteoconductive and osteoinductive properties, and the ability to be moulded into a specific shape. This has only been possible through nanoscale engineering of cell-biomaterial interaction, which is revolutionizing modern implant therapy.

Certainly, the most significant advantages related to the use of polymeric biomaterials are their great biocompatibility, the ability to achieve important changes in their chemical composition, as well as in their physical-mechanical properties and surface characteristics; they have low coefficients of friction, and they also have the ability to incorporate biomolecules or active compounds.

They are capable of forming direct interactions and stable bonds with a living tissue, which can freely cover the entire surface. These biomaterials can also

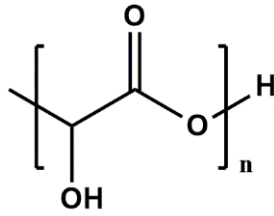
have some disadvantages, such as the release of potentially hazardous compounds (monomers, catalysts, and additives), ease of absorption of water and biomolecules, and relatively low mechanical properties for some applications.

To date, many efforts are being made to solve these well-known problems in both research and industrial settings, given the high application potential of polymers in the biological field.

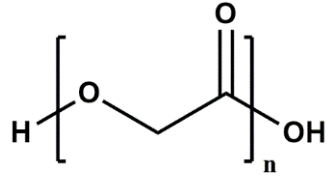
The main distinction that can be made between polymeric biomaterials is based on their ability to biodegrade in the substrate with which they are in contact. They can then be basically divided into absorbable or not absorbable polymers, having different properties and applications, but both of high commercial and scientific interest.

1.1.1 Absorbable polymers and their applications

By definition, a bioresorbable material is a material that undergoes progressive degradation within the biological system without causing unwanted reactions or toxic effects. This degradation is caused by phenomena such as cell phagocytosis, physical dissolution due to biological fluids and enzymatic degradation. Examples of these materials are polylactic acid (PLA) and polyglycolic acid (PGA), (Fig. 2) and some ceramics containing calcium phosphate.



Poly(lactic acid)



Poly(glycolic acid)

Figure 2. Poly(lactic acid) (PLA) and Poly(glycolic acid) (PGA) chemical structure.

Although the specific characteristics of a bioresorbable material vary depending on the intended application, the material must meet a number of requirements of a general nature general requirements, such as being sufficiently versatile in terms of production techniques, remaining unchanged for a time equal to that of the desired therapy, not cause inflammatory reactions that require its removal from the body, and finally after its absorption, the body must not retain memory of the foreign body received. In other words, the body must not retain any memory of the foreign body received.

Natural polymers represented by biomacromolecules also legitimately belong to this category. Chitosan and hyaluronic acid (Fig. 3), have found wide use in the biomedical field as simple and effective drug delivery systems, being able to influence the rate of release.

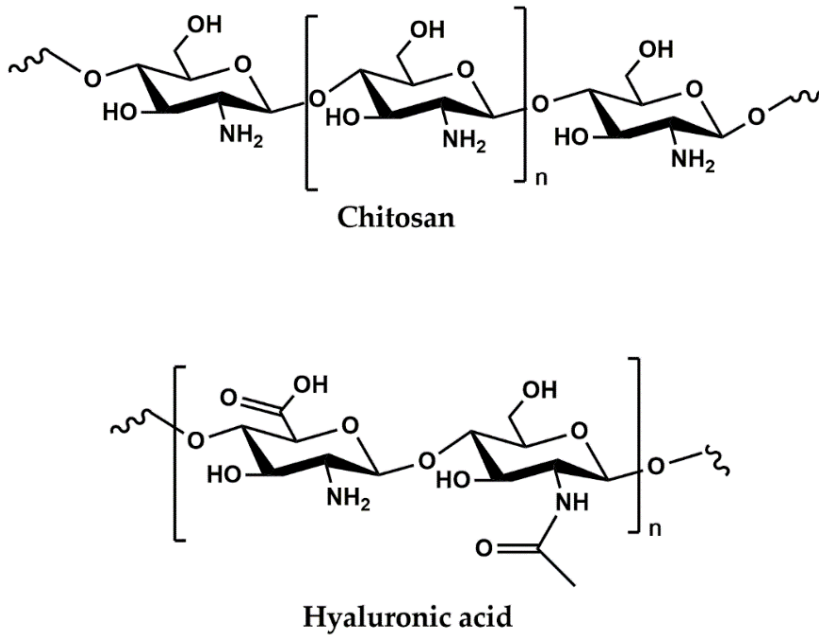


Figure 3. Chitosan and hyaluronic acid chemical structures.

Among the countless applications of these polymers, we find their use as tissue engineering scaffolds and as drug delivery systems.

A scaffold provides the necessary support for cells to proliferate and maintain their differentiated function, and its architecture defines the final anatomical shape of the new tissue. Many of the polymers mentioned can be used to produce these systems. PGA, PLA and natural macromolecules such as collagen or chitosan represent the wide range of materials suitable for this application.

In addition, a polymeric scaffold material must be chosen that degrades and resorbs at a controlled rate while the specific tissue cells embedded within these matrices can diffuse, although all of this is obviously related to the type of tissue that is to be regenerated.

Another application of these polymers as previously mentioned involves the new technology of drug delivery, which involves the systematic release of a

pharmaceutical agent to maintain a therapeutic level of the drug in the body for an extended period of time. It is well known that administering the entire dose of drug in a single portion, can lead to high plasma concentrations, sometimes close to toxicity, of the drug. The real therapeutic effect is obtained, in fact, by maintaining an appropriate plasma concentration in the long term, and providing the drug only where and when it is needed.

An important class of materials widely investigated in the biomedical field are carbon-based nanomaterials. These materials are used both as fillers to be included in polymers in the biomedical devices, as substrates in the sensory field, and as systems for drug delivery, bioimaging and for applications in therapeutic and regenerative medicine. Carbon-based nanomaterials, mainly in the form of fullerene (0D), nanotubes (1D), and graphene (2D), (Fig. 4) play a key role because of their unique physical and chemical properties, such as their hollow structure, high surface-to-volume ratio, electrical conductivity, thermal conductivity, mechanical strength and corrosion resistance, and the ability to easily functionalize them to change their intrinsic properties. Functionalization can increase their solubility and biocompatibility under physiological conditions. Nanomaterials can be further conjugated to specific biomolecules such as polymers, peptides, proteins, nucleic acids, and other therapeutic agents, which can target specific cell types, tissues, and organs.

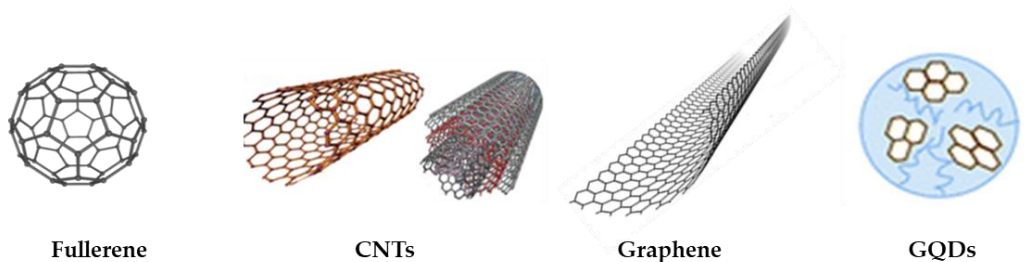


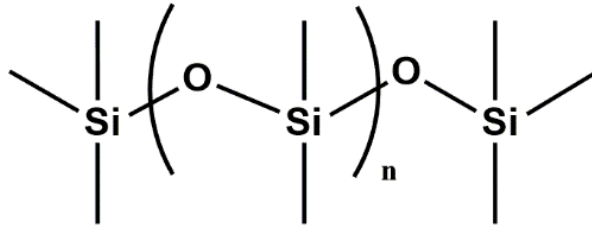
Figure 4. Carbon based nanomaterials

This can be achieved by incorporating the therapeutic agent into a degradable and resorbable polymeric vehicle, releasing the agent continuously as the matrix erodes over time or otherwise being eliminated through excretion pathways. The degradation rate of the material can thus be considered a key factor in governing drug release kinetics, improving the therapeutic value of the treatment.

1.1.2 Non absorbable polymers and their applications

The incorporation of a therapeutic agent into a degradable and resorbable polymeric vehicle, allows the release of the agent continuously as the matrix erodes over time or otherwise being eliminated through excretion pathways. The degradation rate of the material can thus be considered a key factor in governing drug release kinetics, improving the therapeutic value of the treatment. There are several non-biodegradable polymers, such as polyolefins, polyesters, poly(urethanes), poly(acrylates) or copolymers such as poly(ethylene vinyl acetate), that have been used for years as a valuable support in the field of medicine and biological research.[4–6] Applications of polyolefins find use as bone substitutes, but also as drug delivery control devices. They also provide flexibility to product design, manufacturing, sterility and integrity. Synthetic polyesters possess high moisture resistance,

excellent mechanical and thermal properties, and environmental stability. Polyesters are used to make films, capacitor components, and liquid crystal displays. In addition, composites based on polyester resin and glass fibers have been used in automobile and boat body parts. The main applications of poly(acrylates) are coatings, paints, textiles, leather finishing, automotive products, tape adhesives, and oil and high temperature resistant elastomers. They are also used as co-monomers to increase the plasticity of rigid and brittle plastics. Poly(ethylene vinyl acetate) can be used in adhesives, sealants, and coatings, but it also has applications in the biomedical industry as bone, cartilage, vascular, and neural scaffolds. Flexibility, resilience, toughness and transparency increase with increasing vinyl acetate content. Poly(siloxanes) or silicones are organosilicon polymeric materials composed of silicon and oxygen atoms (Fig. 4). The side chains can be methyl, vinyl, or phenyl groups, and are responsible for the properties of the polymer. Poly(siloxanes) are widely used in both medical and environmental fields due to their unique combination of thermal stability, biocompatibility, chemical inertness, and elastomeric properties.[7]



Poly(siloxanes)

Figure 4. Poly (siloxanes) chemical structure.

PDMS is thermally stable, optically transparent, acts as a thermal and electrical insulator, and quite stable chemically and has a rapid degradation rate in the natural environment that differentiates it from other polymers, as well as presenting no environmental problems. [8]

Among the limitations closely related to its application in the biomedical field is the difficulty of wetting its surface with aqueous solvents. This is due to the fact that PDMS has a hydrophobic surface [9] due to its methyl groups, which can lead to the attachment of organic molecules and solvents. [10] Precisely because of this limitation, many efforts have been devoted to improve the surface and wetting properties of PDMS. [11–13]

Among the most important properties of PDMS are permeability and elasticity. Siloxanes exhibit higher permeability than most elastomers. This characteristic of PDMS makes it advantageous for various industrial applications.

The good elastic capacity of silicones comes from the fact that the Si-O structure is more flexible than other conventional polymers that have C-C carbon structures. PDMS offers good elasticity due to the fact that it exists in a very compact form. Thus, when subjected to a tensile force, the polymer

stretches by releasing its tension and then returns to its initial state when the load is removed. This property is affected by the number of cross-links that exist; the more cross-linked the PDMS is, the less elastic it will be.[14]

1.2 Outline of Thesis

Among the biomaterials discussed above, I have been involved in three types of materials used in the biomedical and environmental sectors during my PhD studies, all of which are of an organic nature. In detail, I studied carbon-based nanomaterials for drug delivery, chitosan-based composites for tissue engineering, and (3-Aminopropyl) triethoxysilane based coatings against marine biofouling.

With regards to carbon-based nanomaterials, those characterized by the structure of graphene, such as graphene oxide (GO), carbon nanotubes (CNTs), fullerenes, and graphene quantum dots (GQDs) have received significant interest in cancer therapy due to their small size (typically in the range of 1-100 nm) and unique chemical and physical properties [15]. Materials such as GQDs (Fig. 5) can be considered as biomaterials due to their biocompatibility and low toxicity since they are only composed of organic materials, and can be obtained from biomasses [16]. Moreover, their relative toxicity depends on the particle size, surface functional groups, oxygen content, surface charges, and impurities.[17]

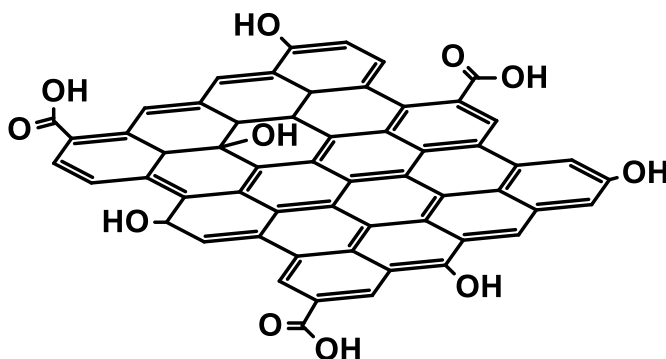


Figure 5. Representative image of GQDs

Chitosan, the N-deacetylated derivative of chitin that forms the exoskeleton of crustacean shells, belongs to the polysaccharide family and has structural similarity to glycosaminoglycan (Fig. 6). Chitosan has been extensively studied as a natural biomaterial for many biomedical applications due to its biocompatibility, biodegradability, antimicrobial properties and functionality. These properties make chitosan a potential biomaterial for many biomedical applications [18]. Furthermore, due to its cationic nature and profuse amine and hydroxyl functional groups on the molecular chain, chitosan is an excellent candidate as a biomaterial to transport proteins and other active molecules through physical or chemical means [19].

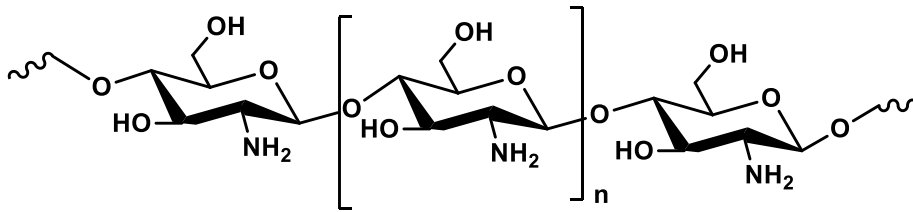


Figure 6. Chitosan structure

Equally fascinating is the study of fouling as a biological event, although in a strictly anthropocentric view it is mostly considered as a damage, as it poses serious problems in engineering and marine industry, with really high costs. Fouling on the bottom of boats increases friction with the water making navigation slower and reducing maneuverability, which leads to increased fuel consumption [20]. In addition, boats can be structurally damaged over time, especially wooden boats, but also iron boats, due to the corrosive activity of many bacteria that "attack" metal [21]. To prevent fouling, special coatings are used that often contain toxic substances that are highly harmful to the environment. This is the case of the so-called organotins, the best known of which is TBT (tributyltin), considered to be the

most toxic chemical compound ever deliberately released into the seas. The effects of the substance, known since the 1970s, when it was identified as a disease agent in an oyster farm in France, are hormonal. Subsequently, the activity of the compound has been detected in numerous marine organisms, in which it accumulates, ultimately posing serious risks to human health through the food chain [22].

In 1990 the IMO (International Maritime Organization) officially recognized the serious environmental risk associated with the use of this substance, but only Japan has unilaterally adopted rules prohibiting its use. After years of pressure from environmental organizations, in particular WWF, in 1999 the IMO adopted a resolution banning globally the use of organotins as antifouling biocides in marine paints as of January 2003, while by 2008 the use of organotin-treated ships will be banned. [23]

A particular approach has been to identify coating substances that can promote the removal of fouling by water during navigation, such as fluoro-urethane compounds associated with silicone coatings [24]. Finally, a number of marine organisms have been identified as producers of antifouling substances, paving the way for the study of natural biocides (Fig. 7) [25].

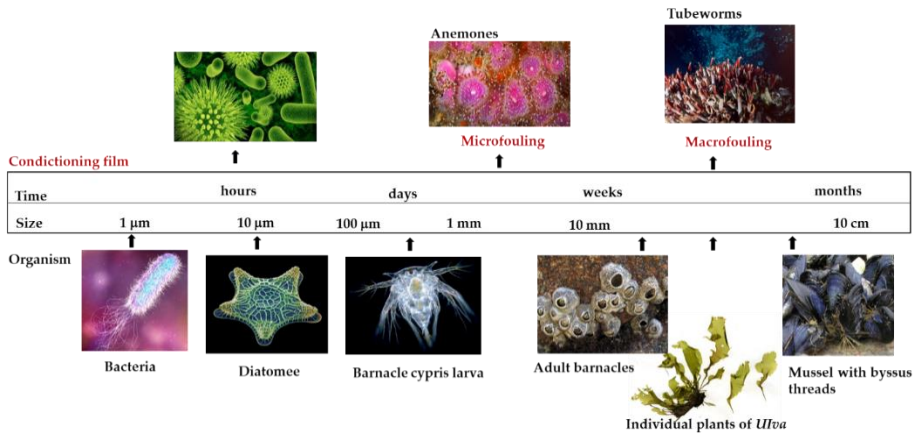


Figure 7. Marine organisms as producers of antifouling substances.

Among the different fouling-resistant coatings the silicone elastomers and in particular poly(dimethyl siloxane) (PDMS) elastomers demonstrated to prevent the adhesion of marine organisms. Unfortunately, they usually swollen in marine environment, leading to poor mechanical properties which limit their applications. Therefore, new alternative approaches for the development of environmentally effective antifouling systems are still required.

REFERENCES

1. More, R.; Haubold, A.; Bokros, J. *Chapter: Biomaterials Science: An Introduction to Materials in Medicine*; 1996; ISBN 0125824602.
2. Insua, A.; Monje, A.; Wang, H.L.; Miron, R.J. Basis of bone metabolism around dental implants during osseointegration and peri-implant bone loss. *J. Biomed. Mater. Res. - Part A* **2017**, *105*, 2075–2089, doi:10.1002/jbm.a.36060.
3. Bioengineering, D. Review Tissue-biomaterial interactions. **1987**, *22*, 3421–3445.
4. Zur, G.; Linder-Ganz, E.; Elsner, J.J.; Shani, J.; Brenner, O.; Agar, G.; Hershman, E.B.; Arnoczky, S.P.; Guilak, F.; Shterling, A. Chondroprotective effects of a polycarbonate-urethane meniscal implant: Histopathological results in a sheep model. *Knee Surgery, Sport. Traumatol. Arthrosc.* **2011**, *19*, 255–263, doi:10.1007/s00167-010-1210-5.
5. Colaris, M.J.L.; de Boer, M.; van der Hulst, R.R.; Cohen Tervaert, J.W. Two hundreds cases of ASIA syndrome following silicone implants: a comparative study of 30 years and a review of current literature. *Immunol. Res.* **2017**, *65*, 120–128, doi:10.1007/s12026-016-8821-y.
6. Nunes-Pereira, J.; Ribeiro, S.; Ribeiro, C.; Gombek, C.J.; Gama, F.M.; Gomes, A.C.; Patterson, D.A.; Lanceros-Méndez, S. Poly(vinylidene fluoride) and copolymers as porous membranes for tissue engineering applications. *Polym. Test.* **2015**, *44*, 234–241, doi:10.1016/j.polymertesting.2015.05.001.
7. Rahimi, A.; Mashak, A. Review on rubbers in medicine: Natural, silicone and polyurethane rubbers. *Plast. Rubber Compos.* **2013**, *42*, 223–230, doi:10.1179/1743289811Y.0000000063.
8. Martin, S.; Bhushan, B. Transparent, wear-resistant,

- superhydrophobic and superoleophobic poly(dimethylsiloxane) (PDMS) surfaces. *J. Colloid Interface Sci.* **2017**, *488*, 118–126, doi:10.1016/j.jcis.2016.10.094.
9. Vlachopoulou, M.E.; Petrou, P.S.; Kakabakos, S.E.; Tserepi, A.; Beltsios, K.; Gogolides, E. Effect of surface nanostructuring of PDMS on wetting properties, hydrophobic recovery and protein adsorption. *Microelectron. Eng.* **2009**, *86*, 1321–1324, doi:10.1016/j.mee.2008.11.050.
10. Abate, A.R.; Lee, D.; Do, T.; Holtze, C.; Weitz, D.A. Glass coating for PDMS microfluidic channels by sol-gel methods. *Lab Chip* **2008**, *8*, 516–518, doi:10.1039/b800001h.
11. Makamba, H.; Kim, J.H.; Lim, K.; Park, N.; Hahn, J.H. Surface modification of poly(dimethylsiloxane) microchannels. *Electrophoresis* **2003**, *24*, 3607–3619, doi:10.1002/elps.200305627.
12. Abbasi, F.; Mirzadeh, H.; Katbab, A.A. Modification of polysiloxane polymers for biomedical applications: A review. *Polym. Int.* **2001**, *50*, 1279–1287, doi:10.1002/pi.783.
13. Zhou, J.; Ellis, A.V.; Voelcker, N.H. Recent developments in PDMS surface modification for microfluidic devices. *Electrophoresis* **2010**, *31*, 2–16, doi:10.1002/elps.200900475.
14. Kuncová-Kallio, J.; Kallio, P.J. PDMS and its suitability for analytical microfluidic devices. *Annu. Int. Conf. IEEE Eng. Med. Biol. - Proc.* **2006**, 2486–2489, doi:10.1109/IEMBS.2006.260465.
15. Tian, P.; Tang, L.; Teng, K.S.; Lau, S.P. Graphene quantum dots from chemistry to applications. *Mater. Today Chem.* **2018**, *10*, 221–258, doi:10.1016/j.mtchem.2018.09.007.

16. Wang, D.; Chen, J.F.; Dai, L. Recent advances in graphene quantum dots for fluorescence bioimaging from cells through tissues to animals. *Part. Part. Syst. Charact.* **2015**, *32*, 515–523, doi:10.1002/ppsc.201400219.
17. Shang, W.; Zhang, X.; Zhang, M.; Fan, Z.; Sun, Y.; Han, M.; Fan, L. The uptake mechanism and biocompatibility of graphene quantum dots with human neural stem cells. *Nanoscale* **2014**, *6*, 5799–5806, doi:10.1039/c3nr06433f.
18. Khor, E.; Lim, L.Y. Implantable applications of chitin and chitosan. *Biomaterials* **2003**, *24*, 2339–2349, doi:10.1016/S0142-9612(03)00026-7.
19. Agnihotri, S.A.; Mallikarjuna, N.N.; Aminabhavi, T.M. Recent advances on chitosan-based micro- and nanoparticles in drug delivery. *J. Control. Release* **2004**, *100*, 5–28, doi:10.1016/j.jconrel.2004.08.010.
20. Yang, W.J.; Neoh, K.G.; Kang, E.T.; Teo, S.L.M.; Rittschof, D. Polymer brush coatings for combating marine biofouling. *Prog. Polym. Sci.* **2014**, *39*, 1017–1042, doi:10.1016/j.progpolymsci.2014.02.002.
21. Callow, J.A.; Callow, M.E. Trends in the development of environmentally friendly fouling-resistant marine coatings. *Nat. Commun.* **2011**, *2*, 210–244, doi:10.1038/ncomms1251.
22. Turner, A.; Glegg, G. TBT-based antifouling paints remain on sale. *Mar. Pollut. Bull.* **2014**, *88*, 398–400, doi:10.1016/j.marpolbul.2014.08.041.
23. Sur, C.; Nagar, A.; Singh, D.K.; Chakraborty, I.N.; Kiser, P. Focus on o&m. *Power* **2006**, *150*, 15–23.
24. Krishnan, S.; Weinman, C.J.; Ober, C.K. Advances in polymers for anti-biofouling surfaces. *J. Mater. Chem.* **2008**, *18*, 3405–3413, doi:10.1039/b801491d.

-
25. Abarzua, S.; Jakubowski, S. ' MARINE ECOLOGY PROGRESS SERIES Mar Ecol Prog Ser Biotechnological investigation for the prevention of biofouling. I. Biological and biochemical principles for the prevention of biofouling. **1995**, *123*, 301–312.

2. CARBON-BASED NANOMATERIALS FOR DRUG DELIVERY

Carbon-based materials are fascinating materials that even today, after decades of research, still draw the attention of the scientific community and industry. A variety of hybridization allows the formation of many different carbon structures such as graphene, graphite, diamond, fullerene, carbon nanotubes, etc. Graphite and diamond are two of the most popular pure solid crystalline structures.[1] The carbon atoms in the diamond cubic structure have a tetrahedral coordination to their four closest neighbors in a sp^3 hybrid electronic configuration. The graphite structure consists equivalent planar layers. Each carbon atom in a plane is bonded to three of the closest neighbors in the plane by sp^2 orbitals. Because of the strong in-plane sp^2 bonds and very weak (Van der Waals) interlayer bonds, graphite can be considered as a two-dimensional structure. The basic unit of graphite is a carbon layer, called graphene.[2]

In 1991, Iijima discovered multiple-walled carbon nanotubes (MWNT) from the carbon soot produced by arc discharge. MWNT is described as almost one-dimensional (1D) for the same reason that graphite is almost two-dimensional (2D), i.e. the carbon tubes nested in the multi-walled structure are weakly coupled (like graphite layers) and the properties of the system are essentially those of an isolated nanotube [3]. About two years later, Iijima *et al.* observed single-walled carbon nanotubes (SWNTs), i.e. a very long cylindrical carbon cage with a single wall of carbon atoms. All these forms of carbon materials have a crystalline structure but possess different properties depending on the binding order of the carbon atoms [4].

In 2004, Geim *et al.*, used a very different approach to obtain graphene, leading to a revolution in carbon nanomaterials field. They started with three-dimensional graphite and extracted a single sheet using a technique called micromechanical cleavage, which consist in using sticky tape to split graphene layers. Graphene is the name given to a flat two-dimensional monolayer of carbon atoms tightly packed into a two-dimensional (2D) honeycomb lattice and is a key building block for graphite materials (graphite, carbon nanotubes, fullerene, etc.) [5]. Graphene, has exceptionally high crystalline and electronic quality and, despite its short history, has already revealed an abundance of potential new applications in many areas including electronics, medicine, energy, environment and transportation.

Recent advances in nanotechnology have shown great promise in revolutionizing cancer therapy, generating novel theranostic therapies that could enable more efficient targeted delivery of anticancer agents while minimizing their distribution in healthy tissues, as well as the development of novel imaging agents for the diagnosis of many types of cancer and image-guided therapy [6]. Organic and inorganic nanoscale materials such as biodegradable synthetic polymers, lipids, mesoporous silica nanoparticles, micelles, dendrimers, magnetic iron oxide nanoparticles, and carbon-based nanomaterials have been applied to the delivery of anticancer agents, including low molecular weight drugs and macromolecules such as proteins, peptides, or genes [7]. Among the different classes of nanomaterials, carbon-based nanomaterials characterized by the presence of graphene structure, have attracted great interest in biomedical applications, including drug delivery, biosensing, biomedical imaging, stem cell technology, and

photothermal therapy, not only because of their small size (typically in the 1 nm to 1 μm range) but also because of their unique optical properties and large surface area. [8–10] (Fig. 1) This fascinating connection between nanoscience and biology mainly originates from the similar size between nanomaterials and some biomolecules whose functions are critical for life such as proteins (1-100 nm) and DNA with 2-3 nm width. Because nanoparticles are composed of materials designed at the atomic or molecular level, they are generally small in size. [11]

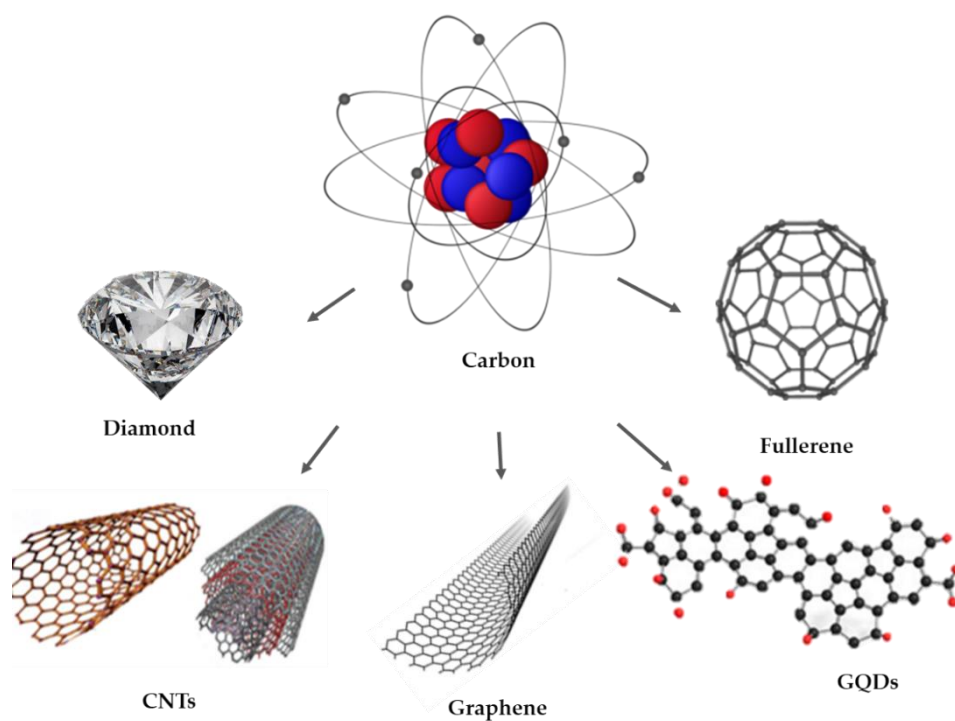


Figure 1. Well-known carbon materials

The intrinsic size-dependent photoluminescence of GQDs allows their monitoring in biological compartments. In addition, these nanomaterials possess a large surface-to-volume ratio and versatile surface functionalization due to the presence of many reactive groups on the surface

of GQDs that allow their multimodal conjugation with various functional groups and biologically active molecules [12]. When compared with other carbon-based nanomaterials, GQDs from graphene sources exhibit particularly unusual physicochemical properties, such as low toxicity, chemical inertness, water solubility, and biocompatibility, which make them ideal nano-carriers for drug delivery [13]. GQDs can be loaded with drugs and labeled with tumor-targeting ligand units that are able to specifically recognize tumor receptors exposed on the surface of cancer cells, generating novel therapeutics that are able to enable more efficient targeted delivery of anticancer agents while minimizing their distribution in healthy tissues, as well as the development of novel imaging agents for *in vitro* and *in vivo* diagnosis of different types of cancer [14]. The π -electron conjugated surface allows supramolecular or covalent binding of hydrophobic molecules to the graphene surface, which enables efficient delivery of water-insoluble drugs in aqueous biological environments[15]. More interestingly, recent work has shown that GQD can be internalized primarily by caveolae-mediated endocytosis and efficiently accelerate the nuclear accumulation of drugs, such as doxorubicin or cisplatin and also greatly enhance the DNA cleavage activity and cytotoxicity of these drugs.[16]In addition to their drug delivery capability, some nano systems have shown the ability to be activated by two or more stimuli for more controlled and improved drug release at the tumor site, thereby minimizing drug delivery and toxicity to healthy tissues.[17] In addition, doping GQDs with different heteroatoms such as nitrogen, phosphorus, or boron have been shown to tune their photophysical behavior through electron transfer processes, opening new avenues for their

application as solar cells and optoelectronic devices.[18]Compared to other nanopatterns and traditional polymers such as polyethylene glycol (PEG), GQDs can provide higher receptor binding affinity and better cellular uptake. These nanomaterials exhibit enhanced drug loading capacity and have been shown to increase the chemotherapy efficacy of anticancer drugs by efficiently accelerating their nuclear accumulation and DNA cleavage activity [19,20]. Their high photothermal conversion efficiency under near-infrared (NIR) light irradiation allows the development of phototheranostic nanoparticles for image-guided photothermal-chemothermal therapy [21–23]. Structural modification of GQDs obtained by top-down or bottom-up approaches has been shown to enable tuning of their physical, chemical, and biological properties [24,25].

2.1 Methods for the synthesis of GQDs

The different synthetic strategies used for the synthesis of GQDs, can be classified into two different routes: top-down and bottom-up approaches (Fig.2) [26].

The first methodologies are based on cutting and exfoliation of graphene-based bulk materials such as graphite, graphene and GO, CNTs, as well as charcoal and natural biomass, under drastic reaction conditions [27–31]. Bottom-up methodologies start from aromatic compounds or other natural or synthetic carbon sources, using different methodologies; the chosen route depends on the application for which the nanomaterial is synthesized. Physicochemical approaches generally allow obtaining GQDs that possess many oxygen-containing functional groups that favor their solubility in water and thus their use in the biological field. However, these

methodologies are generally not suitable for large-scale synthesis due to the already discussed lack of morphological control. Bottom-up procedures can provide more accurate control over the morphology, size, and shape of synthesized GQDs, but such synthetic procedure, in contrast, requires expensive precursors and complex stepwise synthetic routes. However, GQDs synthesized by these methods generally possess superior optical properties and have been developed for *in vitro* and *in vivo* imaging and biosensing applications [32]. The various top-down methodologies for the synthesis of GQDs are generally described as "defect-mediated fragmentation processes" because the oxygen-containing functional groups created during the oxidation processes generate defects on the surface of the material that, in turn, act as reactive sites, allowing the formation of smaller graphene fragments, and the amount of oxygen-containing functionalities strongly depends on the choice of carbon precursor and the chosen cutting methodology [33]. In a very recent work, Hoang *et al.* reported the synthesis of GQDs from GO via a one-step microwave-assisted hydrothermal method, resulting in graphene fragments with strong blue emission. Although the use of graphene-based materials as a carbon source has been shown to afford hydrophilic GQDs of small size and excellent PL performance, the use of environmentally harmful organic solvents and oxidants and the expensive precursors used as a carbon source has driven the search for new alternative processes and green precursors [29]. Chen *et al.* reported a green and efficient one-pot hydrothermal method for the synthesis of GQDs using only water and starch as precursor [31]. The authors obtained GQDs, with very small size (2.25-3.50 nm) endowed with high PL emission, good water solubility

and low cytotoxicity. Recently, Chen *et al.* reported a facile and environmentally friendly hydrothermal process for the synthesis of GQDs, starting from cellulose in the absence of strong oxidants or organic solvents [34]. The synthesized GQDs exhibited nearly uniformly small size, good hydrophilicity, and low cytotoxicity. Among the various top-down methods for the production of GQDs, acid oxidation of graphene-based materials has been shown to be a very simple method that can yield nanomaterials with a high degree of oxygen-containing groups. Zhang *et al.* treated the nanomaterials with a mixture of sulfuric and nitric acid to obtain GQDs with uniform size distribution as fluorescent detection probes for imaging [35]. Zhao *et al.* reported a three-step hydrothermal etching method to prepare GQDs using GO as the precursor and nitric acid as the oxidizer, at different concentrations [36]. The authors obtained GQDs of very small size (in the range of 2.38-3.38 nm) that showed green and yellow luminescence; the different optical properties are due to nitrogen doping and differences in the degree of oxidation. Multi-walled carbon nanotubes (MWCNTs) have also been used as a carbon source to synthesize GQDs with many oxygen-containing functional groups, small particle size, and improved water solubility [37,38]. A technique for complete conversion of MWCNTs into water-dispersible GQDs using sodium bismuth as an oxidizing agent was reported by Biswas *et al.* [43] The synthesized nanoparticles showed high toxicity to bacterial cells and low toxicity to mammalian cells [37]. As for GQDs with controllable morphology and well-distributed size, they can be synthesized by advanced bottom-up approaches from small aromatic precursors or other carbon sources [32,39–44].

Fan *et al.* reported a bottom-up method for the synthesis of highly fluorescent and water-soluble GQDs based on molecular fusion in the aqueous phase, using pyrene and polyethyleneimine as precursors [41]. Microwave irradiation has also been explored for the bottom-up synthesis of GQDs. Recently, Fresco-Cala *et al.* reported a microwave-assisted one-pot reaction for the formation of fluorescent GQDs starting from organic precursors, urea and glucose, and their spontaneous self-assembly forming porous architectures [43]. The authors suggested that the presence of H_3PO_4 enabled the dehydration process of the precursors, promoting the formation of GQDs. To develop an efficient and environmentally friendly bottom-up approach to synthesize GQDs, Zhu *et al.* reported the free-radical polymerization reaction of oxygen-containing aromatic compounds under ultraviolet irradiation [44]. In this work, the authors obtained fluorescent GQDs in high yields, producing only water and CO_2 as byproducts. Naik *et al.* reported a one-step synthesis of GQDs by pyrolysis of citric acid. In this study, the effect of pH on the size and fluorescence intensity of the synthesized nanomaterials was investigated to optimize the reaction conditions [32].

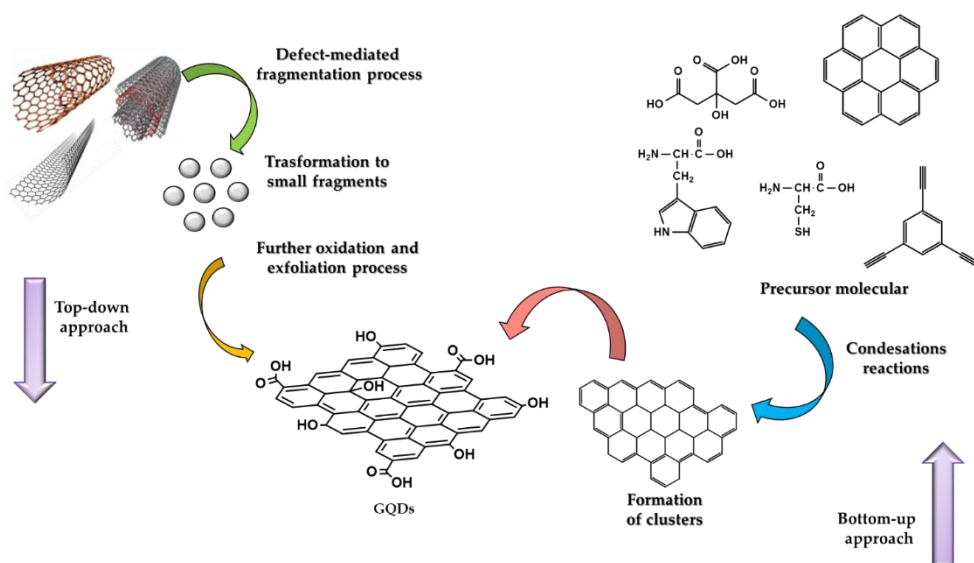


Figure 2. Top-down and bottom-up approaches for the synthesis of GQD

2.2 Application of GQD in drug delivery

To date, many articles treat GQDs as effective carriers for anticancer drugs [45–49]. In addition to their exceptional physical and chemical properties and easy surface functionalization, scientific interest in these nanomaterials is also motivated by their ability to increase the chemotherapeutic efficacy of anticancer drugs that are optimal due to drug resistance (Fig. 3) [47,48]. Zhou *et al.* investigated the influence of the size of graphene nanosheets on the interaction with DNA molecules, showing that GQDs with small lateral sizes show good intercalation ability toward DNA molecules [33]. Recent studies have also shown that GQDs can effectively accelerate the nuclear accumulation of DNA intercalating drugs and decisively improve the DNA cleavage activity and cytotoxicity of these drugs [50,51]. Thus, because of these outstanding biological properties that highlight the superiority of GQDs over modified graphene or GO and many other nanoparticle-based delivery systems, several GQD-based drug delivery systems have been

reported for the treatment of cancer diseases. Sui *et al.* studied the combination of cisplatin with GQDs resulted in increased cytotoxicity of the drug in several cancer cell lines, whereas this effect was not observed in the normal cells tested [51]. The improved cellular uptake and increased toxicity was explained by the small size of GQDs, which allows them to enter the cell nucleus more easily, and the high affinity of GQDs for DNA molecules, leading to increased drug interaction with DNA. The authors reported that the ability of GQDs to enhance the antitumor activity of cisplatin, a chemotherapeutic drug well known both for its efficacy in the treatment of several human cancers including bladder, head, lung, and ovarian cancer, and for its numerous undesirable side effects such as severe renal problems, gastrointestinal disorders, decreased immunity to infections, and development of drug resistance [52]. In another work, Wang *et al.* used GQDs as a nanocarrier to improve the anticancer activity of doxorubicin (DOX) an anticancer agent widely used for the treatment of many common human cancers, including breast cancer and Hodgkin's lymphoma [53]. This drug causes severe side effects leading to major organ toxicity and especially highly dangerous cardiotoxicity, which forces the treatment to become dose limiting. To date, several approaches have been developed to reduce toxicity and improve the therapeutic effect of this agent [54]. The authors, using the DOX/GQD conjugate system, demonstrated efficient delivery of the drug to the nucleus. The results of this study indicate the potential of GQDs to increase the efficacy of chemotherapy, reduce side effects, and improve the therapeutic response of anticancer drugs that exhibit drug resistance [55].

Among different biological ligands, vitamins, polysaccharides, peptides, and proteins have shown specific recognition ability and ease of conjugation with the surface of carboxyl-functionalized graphene-based materials [56]. Recently, the use of B vitamins such as riboflavin (RF, vitamin B2), biotin (vitamin B8), and folate (vitamin B9) has been reported in the literature and for active tumor targeting in GQDs-based drug delivery system (DDS). Recently, Li *et al.* developed a smart DDS for the delivery of mitoxantrone (MTN), an antineoplastic used for solid tumors, by exploiting folic acid (FA) as a targeting ligand [57]. The vitamin was conjugated to carboxylated GQDs by means of a bidentate PEG linker and MTN was adsorbed onto the graphene surface by π - π stacking and hydrogen bonds. The results of in vitro studies, performed in human cervical cancer cells, showed large amounts of MTN released into the cytoplasm after internalization of DDS by the macropinocytosis pathway. Other targeting strategies using, instead, polysaccharides have been shown to provide beneficial properties in DDSs engineered for anticancer therapy, enhancing not only the targeting ability but also the bio adhesiveness, biostability, water dispersibility and biocompatibility of the DDS [58,59]. Thus, several applications of polysaccharides as GQDs-based targeting ligands have been recently described for the targeted delivery of cytotoxic anticancer drugs such as DOX and 5-fluorouracil (5-Fu) [60,61]. Among the different polysaccharides, hyaluronic acid, an acidic mucopolysaccharide composed of alternating *N*-acetyl-d-glucosamine and D-glucuronic acid residues, has proven to be of particular interest in cancer therapy as it exhibits a recognition ability towards specific receptors overexpressed on the surface of cancer cells such

as the integral membrane glycoprotein CD-44, which is highly expressed in many cancers and can regulate metastasis [62]. Ko *et al.* designed a nanocarrier based on GQDs labeled with Herceptin (HER) for the treatment of HER2-overexpressed breast cancer. In this study, photoluminescent GQDs synthesized by pyrolysis of l-glutamic acid were conjugated with a β -cyclodextrin that provided a site for hydrophobic DOX. Subsequent conjugation with HER allowed selective targeting of HER2-overexpressing tumor cells, thus limiting the exposure of DDS toward healthy cells. The final DDS showed the ability to release DOX to human breast cancer in a pH- and temperature-controlled manner [46].

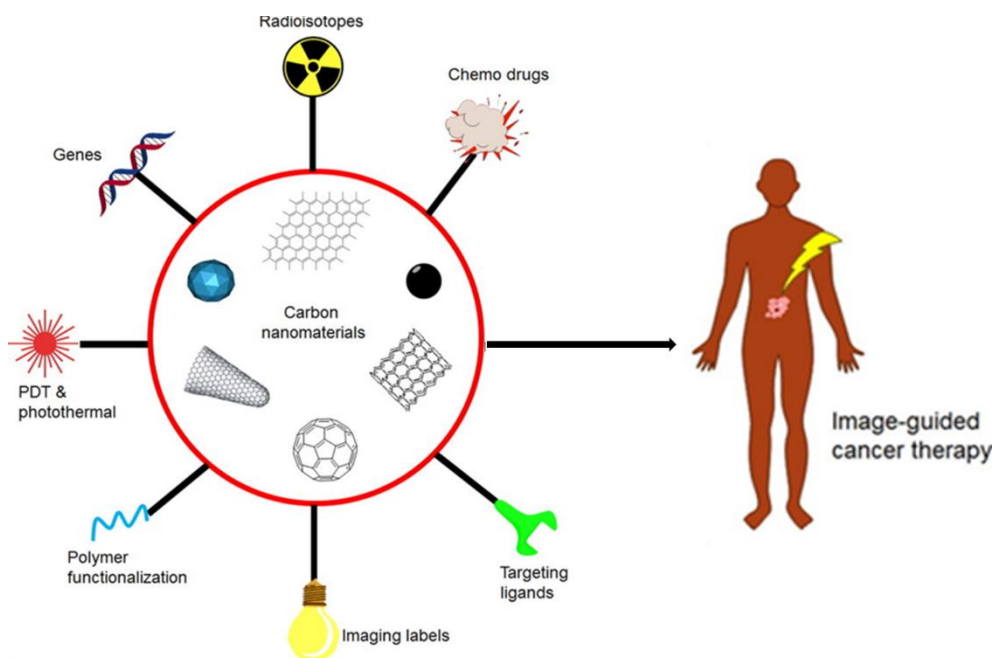


Figure 3. Schematic presentation for the applications of Carbon-based nanomaterials

REFERENCES

1. Leszczynski, J.; Dinadayalane, T.C. *Fundamental Structural, Electronic, and Chemical Properties of Carbon Nanostructures: Graphene, Fullerenes, Carbon Nanotubes, and Their Derivatives*; 2017; ISBN 9783319272825.
2. Geim, A.K. Graphene : Status and Prospects. **2009**, 324, 1530–1535.
3. Iijima, S. (1991). Helical microtubules of graphitic carbon. *Nature*, 354(6348), 56–58. doi:10.1038/354056a0 ©19 9 1 Nature Publishing Group
그라첼꺼. *Nature***1991**, 354, 737–740.
4. Iijima, S.; Ichihashi, T. Single-shell carbon nanotubes of 1-nm diameter. *Nature***1993**, 363, 603–605, doi:10.1038/363603a0.
5. Geim, A.K.; Novoselov, K.S. The rise of graphene. *Nanosci. Technol. A Collect. Rev. from Nat. Journals***2009**, 11–19, doi:10.1142/9789814287005_0002.
6. Zhang, H.; Fan, T.; Chen, W.; Li, Y.; Wang, B. Recent advances of two-dimensional materials in smart drug delivery nano-systems. *Bioact. Mater.***2020**, 5, 1071–1086, doi:10.1016/j.bioactmat.2020.06.012.
7. Patra, J.K.; Das, G.; Fraceto, L.F.; Campos, E.V.R.; Rodriguez-Torres, M.D.P.; Acosta-Torres, L.S.; Diaz-Torres, L.A.; Grillo, R.; Swamy, M.K.; Sharma, S.; et al. Nano based drug delivery systems: Recent developments and future prospects 10 Technology 1007 Nanotechnology 03 Chemical Sciences0306 Physical Chemistry (incl. Structural)03 Chemical Sciences0303 Macromolecular and Materials Chemistry 11 Medical and He. *J. Nanobiotechnology***2018**, 16, 1–33, doi:10.1186/s12951-018-0392-8.
8. Rudramurthy, G.R.; Swamy, M.K.; Sinniah, U.R.; Ghasemzadeh, A. Nanoparticles: Alternatives against drug-resistant pathogenic microbes. *Molecules***2016**, 21, 1–30, doi:10.3390/molecules21070836.

9. Jahangirian, H.; Lemraski, E.G.; Webster, T.J.; Rafiee-Moghaddam, R.; Abdollahi, Y. A review of drug delivery systems based on nanotechnology and green chemistry: Green nanomedicine. *Int. J. Nanomedicine* **2017**, *12*, 2957–2978, doi:10.2147/IJN.S127683.
10. Maiti, D.; Tong, X.; Mou, X.; Yang, K. Carbon-Based Nanomaterials for Biomedical Applications: A Recent Study. *Front. Pharmacol.* **2019**, *9*, 1–16, doi:10.3389/fphar.2018.01401.
11. Lam, P.L.; Wong, W.Y.; Bian, Z.; Chui, C.H.; Gambari, R. Recent advances in green nanoparticulate systems for drug delivery: Efficient delivery and safety concern. *Nanomedicine* **2017**, *12*, 357–385, doi:10.2217/nnm-2016-0305.
12. Wang, J.; Qiu, J. A review of carbon dots in biological applications. *J. Mater. Sci.* **2016**, *51*, 4728–4738, doi:10.1007/s10853-016-9797-7.
13. Chen, X.; Wong, S.T.C. Cancer Theranostics: An Introduction. *Cancer Theranostics* **2014**, 3–8, doi:10.1016/B978-0-12-407722-5.00001-3.
14. Zhou, Q.; Zhang, L.; Wu, H. Nanomaterials for cancer therapies. *Nanotechnol. Rev.* **2017**, *6*, 473–496, doi:10.1515/ntrev-2016-0102.
15. Jain, V.P.; Chaudhary, S.; Sharma, D.; Dabas, N.; Lalji, R.S.K.; Singh, B.K.; Jaiswar, G. Advanced functionalized nanographene oxide as a biomedical agent for drug delivery and anti-cancerous therapy: A review. *Eur. Polym. J.* **2021**, *142*, 110124, doi:10.1016/j.eurpolymj.2020.110124.
16. Kortel, M.; Mansuriya, B.D.; Santana, N.V.; Altintas, Z. Graphene quantum dots as flourishing nanomaterials for bio-imaging, therapy development, and micro-supercapacitors. *Micromachines* **2020**, *11*, doi:10.3390/MI11090866.

REFERENCES

17. Pham, S.H.; Choi, Y.; Choi, J. Stimuli-responsive nanomaterials for application in antitumor therapy and drug delivery. *Pharmaceutics***2020**, *12*, 1–19, doi:10.3390/pharmaceutics12070630.
18. Barman, Monoj Kumar and Jana, Bikash and Bhattacharyya, Santanu and Patra, A. Photophysical Properties of Doped Carbon Dots (N , P and B) and Their Influence on Electron / Hole Transfer in Carbon Dots- Nickel. *J. Phys. Chem. C***2014**, *118*, 20034–20041.
19. Liyanage, P.Y.; Hettiarachchi, S.D.; Zhou, Y.; Ouhtit, A.; Seven, E.S.; Oztan, C.Y.; Celik, E.; Leblanc, R.M. Nanoparticle-mediated targeted drug delivery for breast cancer treatment. *Biochim. Biophys. Acta - Rev. Cancer***2019**, *1871*, 419–433, doi:10.1016/j.bbcan.2019.04.006.
20. Bae, K.H.; Chung, H.J.; Park, T.G. Nanomaterials for cancer therapy and imaging. *Mol. Cells***2011**, *31*, 295–302, doi:10.1007/s10059-011-0051-5.
21. Fang, J.; Liu, Y.; Chen, Y.; Ouyang, D.; Yang, G.; Yu, T. Graphene quantum dots-gated hollow mesoporous carbon nanoplatform for targeting drug delivery and synergistic chemo-photothermal therapy. *Int. J. Nanomedicine***2018**, *13*, 5991–6007, doi:10.2147/IJN.S175934.
22. Guo, X.; Cao, B.; Wang, C.; Lu, S.; Hu, X. In vivo photothermal inhibition of methicillin-resistant *Staphylococcus aureus* infection by in situ templated formulation of pathogen-targeting phototheranostics. *Nanoscale***2020**, *12*, 7651–7659, doi:10.1039/d0nr00181c.
23. Yang, J.; Zhai, S.; Qin, H.; Yan, H.; Xing, D.; Hu, X. NIR-controlled morphology transformation and pulsatile drug delivery based on multifunctional phototheranostic nanoparticles for photoacoustic imaging-guided photothermal-chemotherapy. *Biomaterials***2018**, *176*, 1–12,

doi:10.1016/j.biomaterials.2018.05.033.

24. Facure, M.H.M.; Schneider, R.; Mercante, L.A.; Correa, D.S. A review on graphene quantum dots and their nanocomposites: From laboratory synthesis towards agricultural and environmental applications. *Environ. Sci. Nano***2020**, *7*, 3710–3734, doi:10.1039/d0en00787k.
25. Chen, W.; Lv, G.; Hu, W.; Li, D.; Chen, S.; Dai, Z. Synthesis and applications of graphene quantum dots: A review. *Nanotechnol. Rev.***2018**, *7*, 157–185, doi:10.1515/ntrev-2017-0199.
26. Kundu, S.; Pillai, V.K. Synthesis and characterization of graphene quantum dots. *Phys. Sci. Rev.***2020**, *5*, 1–35, doi:10.1515/psr-2019-0013.
27. Baragau, I.A.; Power, N.P.; Morgan, D.J.; Heil, T.; Lobo, R.A.; Roberts, C.S.; Titirici, M.M.; Dunn, S.; Kellici, S. Continuous hydrothermal flow synthesis of blue-luminescent, excitation-independent nitrogen-doped carbon quantum dots as nanosensors. *J. Mater. Chem. A***2020**, *8*, 3270–3279, doi:10.1039/c9ta11781d.
28. Luo, Z.; Qi, G.; Chen, K.; Zou, M.; Yuwen, L.; Zhang, X.; Huang, W.; Wang, L. Microwave-Assisted Preparation of White Fluorescent Graphene Quantum Dots as a Novel Phosphor for Enhanced White-Light-Emitting Diodes. *Adv. Funct. Mater.***2016**, *26*, 2739–2744, doi:10.1002/adfm.201505044.
29. Hoang, T.T.; Pham, H.P.; Tran, Q.T. A Facile Microwave-Assisted Hydrothermal Synthesis of Graphene Quantum Dots for Organic Solar Cell Efficiency Improvement. *J. Nanomater.***2020**, *2020*, 15–17, doi:10.1155/2020/3207909.
30. Teymourinia, H.; Salavati-Niasari, M.; Amiri, O.; Farangi, M. Facile synthesis of graphene quantum dots from corn powder and their application

REFERENCES

as down conversion effect in quantum dot-dye-sensitized solar cell. *J. Mol. Liq.* **2018**, *251*, 267–272, doi:10.1016/j.molliq.2017.12.059.

31. Chen, W.; Li, D.; Tian, L.; Xiang, W.; Wang, T.; Hu, W.; Hu, Y.; Chen, S.; Chen, J.; Dai, Z. Synthesis of graphene quantum dots from natural polymer starch for cell imaging. *Green Chem.* **2018**, *20*, 4438–4442, doi:10.1039/c8gc02106f.

32. Naik, J.P.; Sutradhar, P.; Saha, M. Molecular scale rapid synthesis of graphene quantum dots (GQDs). *J. Nanostructure Chem.* **2017**, *7*, 85–89, doi:10.1007/s40097-017-0222-9.

33. Zhou, X.; Zhang, Y.; Wang, C.; Wu, X.; Yang, Y.; Zheng, B.; Wu, H.; Guo, S.; Zhang, J. Photo-Fenton reaction of graphene oxide: A new strategy to prepare graphene quantum dots for DNA cleavage. *ACS Nano* **2012**, *6*, 6592–6599, doi:10.1021/nn301629v.

34. Chen, W.; Shen, J.; Lv, G.; Li, D.; Hu, Y.; Zhou, C.; Liu, X.; Dai, Z. Green Synthesis of Graphene Quantum Dots from Cotton Cellulose. *ChemistrySelect* **2019**, *4*, 2898–2902, doi:10.1002/slct.201803512.

35. Zhang, C.; Li, J.; Zeng, X.; Yuan, Z.; Zhao, N. Graphene quantum dots derived from hollow carbon nano-onions. *Nano Res.* **2018**, *11*, 174–184, doi:10.1007/s12274-017-1617-0.

36. Zhao, M. Direct synthesis of graphene quantum dots with different fluorescence properties by oxidation of graphene oxide using nitric acid. *Appl. Sci.* **2018**, *8*, doi:10.3390/app8081303.

37. Biswas, A.; Khandelwal, P.; Das, R.; Salunke, G.; Alam, A.; Ghorai, S.; Chattopadhyay, S.; Poddar, P. Oxidant mediated one-step complete conversion of multi-walled carbon nanotubes to graphene quantum dots and their bioactivity

against mammalian and bacterial cells; 2017; Vol. 5; ISBN 9120259026.

38. Iannazzo, D.; Pistone, A.; Ferro, S.; De Luca, L.; Monforte, A.M.; Romeo, R.; Buemi, M.R.; Pannecouque, C. Graphene Quantum Dots Based Systems As HIV Inhibitors. *Bioconj. Chem.***2018**, *29*, 3084–3093, doi:10.1021/acs.bioconjchem.8b00448.
39. Yin, L.; Zhou, J.; Li, W.; Zhang, J.; Wang, L. Yellow fluorescent graphene quantum dots as a phosphor for white tunable light-emitting diodes. *RSC Adv.***2019**, *9*, 9301–9307, doi:10.1039/c8ra10353d.
40. Wang, Z.; Yu, J.; Zhang, X.; Li, N.; Liu, B.; Li, Y.; Wang, Y.; Wang, W.; Li, Y.; Zhang, L.; et al. Large-Scale and Controllable Synthesis of Graphene Quantum Dots from Rice Husk Biomass: A Comprehensive Utilization Strategy. *ACS Appl. Mater. Interfaces***2016**, *8*, 1434–1439, doi:10.1021/acsami.5b10660.
41. Liu, P.; Wei, Z.; Cheng, K.; Liao, X.; Qin, X.; Feng, Y.; Rao, J.; Chen, J.; Wang, T.; Liu, L.; et al. Self-healable flexible luminescent films based on silk fibroin and graphene quantum dots. *OSA Contin.***2020**, *3*, 1021, doi:10.1364/osac.383872.
42. Kumawat, M.K.; Thakur, M.; Gurung, R.B.; Srivastava, R. Graphene Quantum Dots for Cell Proliferation, Nucleus Imaging, and Photoluminescent Sensing Applications. *Sci. Rep.***2017**, *7*, 1–16, doi:10.1038/s41598-017-16025-w.
43. Fresco-Cala, B.; Soriano, M.L.; Sciortino, A.; Cannas, M.; Messina, F.; Cardenas, S. One-pot synthesis of graphene quantum dots and simultaneous nanostructured self-assembly: Via a novel microwave-assisted method: Impact on triazine removal and efficiency monitoring. *RSC Adv.***2018**, *8*,

29939–29946, doi:10.1039/c8ra04286a.

44. Zhu, J.; Tang, Y.; Wang, G.; Mao, J.; Liu, Z.; Sun, T.; Wang, M.; Chen, D.; Yang, Y.; Li, J.; et al. Green, Rapid, and Universal Preparation Approach of Graphene Quantum Dots under Ultraviolet Irradiation. *ACS Appl. Mater. Interfaces***2017**, *9*, 14470–14477, doi:10.1021/acsami.6b11525.

45. Jing, Y.; Zhu, Y.; Yang, X.; Shen, J.; Li, C. Ultrasound-triggered smart drug release from multifunctional core-shell capsules one-step fabricated by coaxial electrospray method. *Langmuir***2011**, *27*, 1175–1180, doi:10.1021/la1042734.

46. Ko, N.R.; Nafiujjaman, M.; Lee, J.S.; Lim, H.N.; Lee, Y.K.; Kwon, I.K. Graphene quantum dot-based theranostic agents for active targeting of breast cancer. *RSC Adv.***2017**, *7*, 11420–11427, doi:10.1039/c6ra25949a.

47. Wang, X.; Sun, X.; Lao, J.; He, H.; Cheng, T.; Wang, M.; Wang, S.; Huang, F. Multifunctional graphene quantum dots for simultaneous targeted cellular imaging and drug delivery. *Colloids Surfaces B Biointerfaces***2014**, *122*, 638–644, doi:10.1016/j.colsurfb.2014.07.043.

48. Liu, X.; Liu, H.J.; Cheng, F.; Chen, Y. Preparation and characterization of multi stimuli-responsive photoluminescent nanocomposites of graphene quantum dots with hyperbranched polyethylenimine derivatives. *Nanoscale***2014**, *6*, 7453–7460, doi:10.1039/c4nr00739e.

49. Qiu, J.; Zhang, R.; Li, J.; Sang, Y.; Tang, W.; Gil, P.R.; Liu, H. Fluorescent graphene quantum dots as traceable, pH-sensitive drug delivery systems. *Int. J. Nanomedicine***2015**, *10*, 6709–6724, doi:10.2147/IJN.S91864.

50. Frieler, M.; Pho, C.; Lee, B.H.; Dobrovolny, H.; Naumov, A. V.; Akkaraju, G.R. Effects of doxorubicin delivery by nitrogen-doped graphene

quantum dots on cancer cell growth: Experimental study and mathematical modeling. *Nanomaterials***2021**, *11*, 1–15, doi:10.3390/nano11010140.

51. Sui, X.; Luo, C.; Wang, C.; Zhang, F.; Zhang, J.; Guo, S. Graphene quantum dots enhance anticancer activity of cisplatin via increasing its cellular and nuclear uptake. *Nanomedicine Nanotechnology, Biol. Med.***2016**, *12*, 1997–2006, doi:10.1016/j.nano.2016.03.010.

52. Dasari, S.; Bernard Tchounwou, P. Cisplatin in cancer therapy: Molecular mechanisms of action. *Eur. J. Pharmacol.***2014**, *740*, 364–378, doi:10.1016/j.ejphar.2014.07.025.

53. Wang, C.; Wu, C.; Zhou, X.; Han, T.; Xin, X.; Wu, J.; Zhang, J.; Guo, S. Enhancing Cell Nucleus Accumulation and DNA Cleavage Activity of Anti-Cancer Drug via Graphene Quantum Dots. *Sci. Rep.***2013**, *3*, 1–8, doi:10.1038/srep02852.

54. Kim, J.; Hong, J.; Lee, J.; Fakhraei Lahiji, S.; Kim, Y.H. Recent advances in tumor microenvironment-targeted nanomedicine delivery approaches to overcome limitations of immune checkpoint blockade-based immunotherapy. *J. Control. Release***2021**, *332*, 109–126, doi:10.1016/j.jconrel.2021.02.002.

55. Senapati, S.; Mahanta, A.K.; Kumar, S.; Maiti, P. Controlled drug delivery vehicles for cancer treatment and their performance. *Signal Transduct. Target. Ther.***2018**, *3*, 1–19, doi:10.1038/s41392-017-0004-3.

56. Alibakhshi, A.; Abarghooi Kahaki, F.; Ahangarzadeh, S.; Yaghoobi, H.; Yarian, F.; Arezumand, R.; Ranjbari, J.; Mokhtarzadeh, A.; de la Guardia, M. Targeted cancer therapy through antibody fragments-decorated nanomedicines. *J. Control. Release***2017**, *268*, 323–334,

doi:10.1016/j.jconrel.2017.10.036.

57. Jampilek, J.; Kralova, K. Advances in drug delivery nanosystems using graphene-based materials and carbon nanotubes. *Materials (Basel)*.**2021**, *14*, 1–39, doi:10.3390/ma14051059.

58. Aronson, M.R.; Medina, S.H.; Mitchell, M.J. Peptide functionalized liposomes for receptor targeted cancer therapy. *APL Bioeng*.**2021**, *5*, doi:10.1063/5.0029860.

59. Lewis Phillips, G.D.; Li, G.; Dugger, D.L.; Crocker, L.M.; Parsons, K.L.; Mai, E.; Blättler, W.A.; Lambert, J.M.; Chari, R.V.J.; Lutz, R.J.; et al. Targeting HER2-positive breast cancer with trastuzumab-DM1, an antibody-cytotoxic drug conjugate. *Cancer Res*.**2008**, *68*, 9280–9290, doi:10.1158/0008-5472.CAN-08-1776.

60. Gui, W.; Zhang, J.; Chen, X.; Yu, D.; Ma, Q. N-Doped graphene quantum dot @ mesoporous silica nanoparticles modified with hyaluronic acid for fluorescent imaging of tumor cells and drug delivery. **2017**, *2*, 2–9.

61. Nigam Joshi, P.; Agawane, S.; Athalye, M.C.; Jadhav, V.; Sarkar, D.; Prakash, R. Multifunctional inulin tethered silver-graphene quantum dots nanotheranostic module for pancreatic cancer therapy. *Mater. Sci. Eng. C***2017**, *78*, 1203–1211, doi:10.1016/j.msec.2017.03.176.

62. Senbanjo, L.T.; Chellaiah, M.A. CD44: A multifunctional cell surface adhesion receptor is a regulator of progression and metastasis of cancer cells. *Front. Cell Dev. Biol*.**2017**, *5*, doi:10.3389/fcell.2017.00018.

3. CHITOSAN-BASED HYDROGEL FOR TISSUE ENGINEERING

Polymeric materials, thanks to their suitable intrinsic properties, have found wide use as biomaterials in regenerative medicine (bone and soft tissue scaffolds and elastic supports), as drug delivery systems, and as components for prostheses (in cardiology, orthopedics, ophthalmology).

Among the most important advantages related to the use of polymeric biomaterials there are their great biocompatibility, physical-mechanical properties and surface characteristics, low coefficients of friction, easy processing and workability even in complex geometries, and also the ability to incorporate different biomolecules or active compounds. (Fig. 1)

Biomaterials are able to form direct interactions and biochemical bonds with a living tissue, which can freely cover the entire surface.

Especially in recent decades, biodegradable polymers have received increasing interest in the field of tissue engineering [1,2]. Compared to other traditional implantation materials, such as metals and non-degradable polymers, biodegradable polymers, once implanted *in vivo*, degrade over time through enzymatic, microbial, or chemical processes, yielding non-toxic by products that are then excreted and metabolized in that form [3–9]. Among the different 3D scaffold based on biopolymers, polysaccharide-based hydrogels composed of chitosan, alginate, dextran, or hyaluronic acid have been extensively studied for bone and soft tissue engineering applications due to their high biocompatibility and biodegradability, low cost, ease of handling, viscoelastic properties comparable to soft tissues, ability to gel *in situ*, and ability to provide an ideal hydrated environment for cell or tissue growth [10]. In addition, based on their chemistry, they can be

cross-linked, allowing the incorporation of cells, growth factors, and the controlled release of bioactive molecules [11]. Among the different natural polysaccharides, chitosan (CS), a D-glucosamine polymer of natural origin, biodegradable, biocompatible and most importantly, osteoinductive, obtained by deacetylation of chitin has been widely studied for the development of scaffolds used to repair or regenerate organs or tissues, due to the biological properties derived from its chemical composition [12].

In addition, chitosan, such as often biopolymer hybrid composites, containing inorganic materials with intrinsic bioactive properties and cytocompatibility have demonstrated the ability to promote repair and regeneration of damaged tissues through intrinsic osteoinductive properties and/or by triggering stimulatory effects on bone cells and tissues, such as pH, ionic strength, temperature, light, and magnetic yields [13].

However, in addition to its exceptional chemical, physical, and biological characteristics, applications of scaffolds based on natural chitosan exhibit limitations mainly related to its low mechanical strength, rapid hydrolysis, and sudden drug release that limit its use, as a single component, in bone tissue engineering formulations [14,15]. In order to improve the mechanical behavior and biological stability of chitosan-based scaffolds, 3D hydrogels can be reinforced with materials such as silica, titanium dioxide, zirconium oxide nanoparticles and hydroxyapatite (HA) [16,17].

In fact, chitosan is often formed into a composite structure with calcium phosphate (CaP) to produce a useful adjuvant material (bone cement) with better mechanical properties than chitosan hydrogel alone [18]. However, hydroxyapatite, which is the major inorganic component of bone, has shown

to have superior osteoconductive properties than CaP, with a slower dissolution rate that encourages prolonged ossification [19–21]. When HA is incorporated in chitosan matrices, it has shown to overcome some limitations of commonly used bone cements that are inherently brittle and difficult to fabricate into specific forms [22,23]. Among different inorganic composites, silica nanoparticles have been shown to improve mechanical properties of polymers by providing an improvement in their structure and increasing the bioactivity of related composites. Polyhedral oligomeric silsesquioxanes (POSS) are silicon/oxygen cage structures with $\text{RSiO}_{3/2}$ repeat units and 1-3 nm dimensions. These compounds are characterized by a hybrid chemical composition, intermediate between that of inorganic materials (SiO_2) and organic silicon polymers (R_2SiO) [24]. This structural peculiarity gives to POSS, "hybrid" properties and thus the ability to be inert and thermally stable due to the presence of the inorganic Si-O-Si fragment and also the reactivity and ability to be easily modified due to the presence of the R-Si fragment. In addition, it has been shown that these nanostructured materials can improve the mechanical and rheological properties of biopolymers, and stimulate important biological responses at specific size dimensions, such as cell adhesion and apatite formation [25,26].

In addition to the possibility to reinforce this biopolymer with inorganic structures, it is possible to exploit the chemical functionalization of chitosan with biocompatible polymeric structures, such as the graft copolymerization or coupling with biodegradable dendrimers and cyclodextrins, which has shown to improve the characteristics relevant to its use in hydrogel formulations [27]. Dendrimers, highly branched globular macromolecular

structures with nanoscale dimensions, possess a typical tree-like architecture that can influence the chemical and physical properties of these hybrid compounds, especially at high molecular weights, thus offering several possibilities in biomedical applications [28–30]. Among the different types of synthetic dendrimers, poly(amidoamine) (PAMAM) dendrimers, (Fig. 1) which consist of alkyl-diamine cores, represent the most common class of biodegradable dendrimers and have been studied for the targeted drug and gene delivery as well as for the development of co-delivery systems.[31]

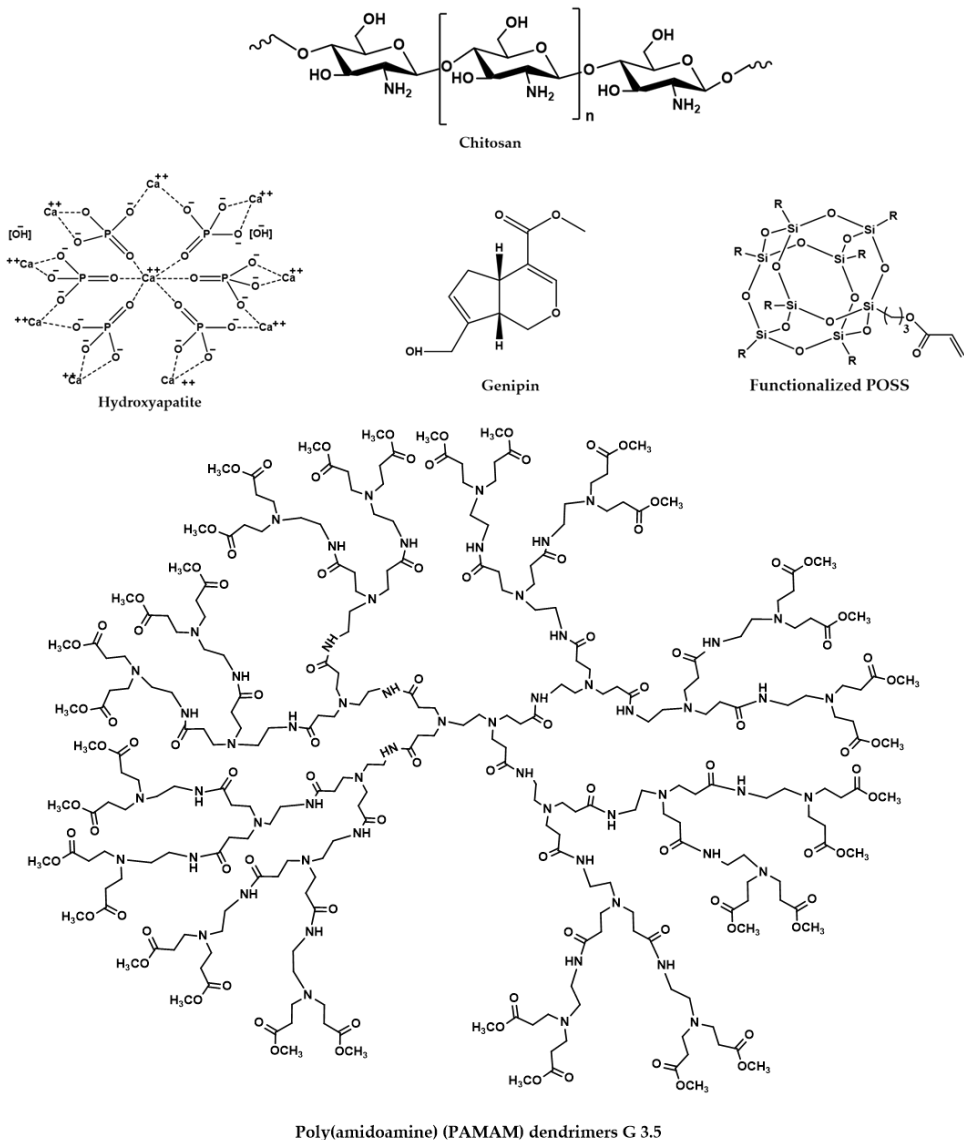


Figure 1. Biomaterials for tissue engineering

3.1 Characteristics of an ideal scaffold

The development of 3D scaffolds, support structures or matrices that induce cells to form functional tissues, is a major goal of tissue engineering. Specifically, using scaffolds, transplanted cells can be delivered to a specific location in a tissue, driving cell growth at the desired anatomical site.

The characteristics required for an ideal scaffold are:

- Porosity
- Mechanical strength
- Biocompatibility

The scaffold architecture should have a highly interconnected pore structure and high porosity to ensure cellular penetration and diffusion of nutrients to cells within the scaffold. The porous nature also aids in the diffusion of waste products and degradation products from the scaffold to leave the body without interfering with surrounding tissues or organs [32]. Porosity can be intentionally created by the manufacturing process or can also occur as an artifact of manufacturing. Porous scaffolds are mainly used for artificial skin, blood vessels, drug delivery, bone and cartilage reconstruction, periodontal repair, etc., each after the fulfillment of some specific requirements.

Mechanical strength is a key factor to consider when designing or determining the suitability of a scaffold in tissue engineering. The mechanical properties of the biomaterial used to make the scaffold should match those of the host tissue [33]. For the scaffold creation, especially in the construction of load-bearing hard tissues such as bone and cartilage that maintains its structure even after implantation, mechanical strength represents a very essential factor. The mechanical properties of the biomaterial must be tailored to the proposed function to avoid failure. For example, for fixation of a bone fracture, it is necessary to have a required strength to avoid fracture. The intrinsic properties required for a material from a mechanical standpoint are modulus of elasticity, yield strength, and ultimate load. These three properties determine the stiffness, deformability

and strength of a material. Another property is fatigue, which is a process by which structures fail as a result of a cyclic stress that is less than the ultimate load. Cyclic stresses are very common in the human body in places such as heart pumping, limb connections, etc. After the preparation of the required tissue-engineered construct, it should be successfully integrated into the living system and only after addressing the issues in technologies for integration into the living system, the success in tissue engineering can be achieved. This involves the issues of biocompatibility and immune acceptance [34].

Biocompatibility is the property of a material that, when introduced into a living body to perform a specific function, does not interfere with or enhance the function of an organ and does not exert local or general toxicological actions in the body. After performing the functions it should be biodegraded and the products of biodegradation should be completely eliminated and natural tissues should regenerate in place of the implant [35]. In simple terms, biocompatibility can be defined as the ability of a medical device or a material to perform within an appropriate host response and in a specific situation. The magnitude and duration of any adverse alteration in the homeostatic mechanisms that determine the host response can be measured and is referred to as a biocompatibility assessment [36]. Potential biological hazards can include short-term effects, specific toxic effects, and long-term effects. Several *in vivo* tests to determine biocompatibility include sensitization, intracutaneous irritation and reactivity, acute and subacute toxicity (systemic and subchronic toxicity), genotoxicity, chronic toxicity, human and environmental toxicity, compatibility, carcinogenicity,

reproductive and developmental toxicity, biodegradation, and immune responses.

3.2 Applications in tissue engineering

The chemical structure of chitosan and its mechanical properties have shown to be stable in physiological environments (Fig. 2) [37]. Moreover, the degradation products of chitosan are often the substances involved in cartilage synthesis [38]. Cui *et al.* investigated how these intrinsic characteristics of chitosan create broad applications in bone and cartilage tissue engineering [39]. The authors used a chitosan coating in PCL scaffolds, and this layer resulted in improved cell attachment and infiltration. On the other hand, to improve the biological, osteoconductive, and mechanical properties of chitosan, it was suggested to functionalize it with other materials such as bioglass [39], collagen, etc. [40]. Ang *et al.* developed a novel robotic rapid prototyping delivery system to fabricate a chitosan/hydroxyapatite scaffold. They added a chitosan scaffold the hydroxyapatite (HA) to improve the osteoconductivity and mechanical strength of the scaffolds. They dispersed the chitosan-HA in acetic acid to prepare the final hydrogels, and finally performed an extrusion in a mixture of sodium hydroxide and ethanol to create a gel-like precipitation.[41]

It was reported that higher amounts of NaOH resulted in rapid precipitation and low mobility of the chitosan molecules, and thus little or no attachment of the layers was obtained. Conversely, a very low concentration of NaOH lowered the precipitation rate and provided low shape retention. Chavanne *et al.* evaluated different binders for 3D printing chitosan and obtained near optimal results for lactic acid [42]. They performed new studies on printing

a similar composition (chitosan/HA) while lactic acid, citric acid, and acetic acid were used as binders. They found that lactic acid at 40 wt % provided a suitable structure compared to the other binders due to its medium viscosity, high wettability, and short solidification time. There was an improvement in the material stability using a composite ratio of 20 wt % chitosan and 40 wt% lactic acid as binder, and post-treatment with 40% lactic acid.

The resulting moulded specimens showed 16.32 MPa compressive strength, 4.4 G Pa elastic modulus, and 37.1% porosity. The low porosity value was the result of open pore collapse as a result of high lactic acid concentration. Their results showed that the chitosan/HA moulded scaffold is a promising alternative for bone regeneration. In a recent study, Morris *et al.* evaluated the mechanical properties and cytocompatibility of a hybrid composition comprising chitosan and a synthetic polymer (polyethylene glycol diacrylate (PEGDA) [43]. The ratio of PEGDA to chitosan was set to 1:5 and 1:10 considered as the optimal range. Low molecular weight chitosan (LMWC) needs higher concentration of sodium acetate to neutralize its protonated amine groups due to its higher de-acetylation degree. They used stereolithography (SLA) for scaffold fabrication while the ratio of 1:7.5 indicated better printability. SLA showed adequate potential to control scaffold compositions and porous structure according to patients' anatomical requirements. They constructed ear-shaped scaffolds using a 405 nm laser beam. The presence of higher concentrations of chitosan in the resin formulation improved the swelling ratio. Adequate mechanical properties and great potential to support cell adhesion and proliferation led to a

promising construct for the cartilage tissue engineering with complex geometries.

In another recent study, Reed *et al.* investigated an acellular chitosan-alginate scaffold for cartilage tissue engineering [44].

Chitosan-alginate was chosen as a desirable combination because of its similarity to natural articular cartilage glycosaminoglycans (GAGs) such as keratin sulphate, hyaluronic acid, and chondroitin sulphate. This composition is capable of conferring desirable properties such as compressive strength and swelling potential. In addition, pH-neutral scaffold preparation provides a safe environment that protects the combined growth factor or drugs from denaturation. In the used method, macro-channels were created from 3D printed positive and negative molds and directional freezing of the solution created micro-channels. These scaffolds made cartilage imitation more natural by facilitating the regeneration process. Madihally *et al.* functionalized chitosan with gelatin without the need for post-processing [45]. The mixture of chitosan and gelatin was prepared in deionized water acidulated with hydrochloric acid, and finally affixing the cells to the solution. The results of this study showed that solid contaminants, aggregation and gelling can lead to needle clogging in the 3D bioprinting process. Cooling of the prepared solution, centrifugation, and vacuum degassing inhibited these challenges during printing. The authors showed that as the concentration of chitosan increased, also, the viscosity increased, and, consequently, accelerated gelation time decreased the fiber size. It was demonstrated that the novel bioprinter was capable of providing an easy and inexpensive method for bioprinting a chitosan/gelatin substrate

while maintaining high cell viability. Demirtas *et al.* revealed that bioprinting chitosan prepared in acidic solution can be detrimental to cell viability and pH-sensitive molecules [46]. Therefore, they introduced new chitosan hydrogels for more effective bioprinting. For this purpose, they dissolved chitosan in an acetic acid solution, to which they then added sodium phosphate salt of glycerol and raised the pH to about 6.95-7.00 by adding sodium hydroxide, which is more suitable for cell viability. The limiting factor was a faster gelation time-when larger amounts of NaOH were used, and on the other hand, the composite was not printable. Therefore, it should be added to adjust the pH to 7.00. For this composition, the gelation starts at about 32 °C, and completely turns into a gel at about 37 °C. The authors also added hydroxyapatite to the solution to improve osteoconductivity, osteoinductivity, and mechanical strength. Biological assays showed that cells printed in chitosan/hydroxyapatite hydrogels afforded more cell viability and osteogenic markers than those made of alginate, which is known as the most usable material for cell encapsulation of bioprinting materials. Huang *et al.* introduced a novel gelatin hydrogel composition loaded with bone marrow stem cells/sodium alginate/carboxymethyl chitosan for 3D bioprinting [47]. The objective in using chitosan is to improve cell adhesion, proliferation, and mechanical strength due to ionic bonding between the amine group of chitosan and the carboxyl group of alginate. To improve the aqueous solubility, chitosan was modified to carboxymethyl chitosan. For solution preparation, gelatin was dissolved in water, then alginate and carboxymethyl chitosan were added to the solution, and it was cross-linked ionically by 2% CaCl₂. Bone marrow stem cells were loaded onto

the hydrogels, and biological 3D printing was performed. The authors showed that the degradation ratio of hydrogels with carboxymethyl chitosan decreased compared to hydrogels without chitosan, which means that carboxymethyl chitosan improved the stability of the hydrogel. In addition, antibacterial activity was improved by using carboxymethyl chitosan compared to hydrogel without chitosan. Muller *et al.* modified chitosan into *N, O*-carboxyethyl chitosan to react with polyphosphate in order to improve the biological and bioactivity properties of the hydrogel [48]. The authors dissolved the *N, O*-carboxyethyl chitosan in a saline solution and added the polyphosphate to the solution, which, subsequently, was centrifuged. Finally, the solution was treated with an aqueous alginate solution and was bioprinted by a 3D bioprinter. Then CaCl_2 was added for crosslinking and curing of the bioprinted structures. The suggested composition induced SaOS-2 bone-like cells to bio-mineralize. Such scaffolds were assayed *in vivo*, revealing strong regeneration inducing activity in rat calvarial defects. This composition appears to be a very effective material for custom design of bone scaffolds.

Based on *in vitro* cell culture, the application of hydrogels containing polyhedral oligomeric silsesquioxanes (POSS) for tissue engineering were further studied *in vivo*, due to the ability of POSS to initiate the cellular response to form apatite, the main inorganic component of bone, thus favouring the bone repair [26]. Li *et al.* constructed hydrogels from octa-vinyl POSS (OVPOSS) and PEG-dithiol via click reaction with easily customizable mechanical behaviour and interfacial nature by varying the length of PEG [49]. The bioactivity and biocompatibility of the materials were confirmed by

a series of *in vitro* and *in vivo* tests, and then the adipose-derived stem cell-encapsulated hydrogels were implanted into a critically sized site of the femoral condyle to evaluate the capacity for osteogenesis *in vivo*. Mineralization at the site, after six weeks, was characterized using microcomputed tomography (micro-CT), and new bone formation was observed at the empty defect sites with bone mineral density comparable to that of normal bone. However, complete bone repair was prevented throughout because of the non-degradability of the hydrogels and the lack of new bone formation space, so further refinement of the structure was needed. Fan *et al.* developed hydrogels from methacrylate gelatin and octa-methacrylate POSS (OMAPOSS) by photo crosslinking [50]. Gelatin hydrogels were superior because of their good biocompatibility, biodegradability, and cell adhesion, but they were limited by poor mechanical properties and a too fast degradation rate for long-term tissue repair [51]. The introduction of POSS well ameliorated the problems by maintaining or even extending the original advantages to meet tissue growth needs. When assayed, POSS-containing hydrogels showed clearly improved osseointegration and osteoinduction effects, compared to hydrogel groups without gels or without POSS.

A type of IPN (interpenetrating polymer network) hydrogels was also investigated through a photo-crosslinking process, where the first network consisted of OMAPOSS and methacrylate chitosan and the second network was prepared from methacrylate gelatin [52]. IPN hydrogels showed much better performance in bone regeneration. Multilayer hydrogels are considered as a feasible solution since stem cell differentiation has been

reported to be influenced by the elasticity of the materials providing spatially distinct cellular phenotypes and stimulating regeneration of complex tissues [53]. As part of this strategy, Yuan *et al.* developed a three-layer hydrogel based on gelatin, chitosan, and poly(ethylene glycol) dimethacrylate (PEGDMA) via photo-crosslinking [54]. The gelatin and chitosan were pre-treated with different amounts of glycidyl methacrylate leading to increasing crosslinking density from top to bottom. Together with the addition of OVPOSS in the deep layer, the hydrogels exhibited graded morphology, swelling ratio, and mechanical properties with good interconnectivity. The potential of the hydrogels for repairing osteochondral defects were evaluated on a rabbit model, and after implantation for two months, the cartilage and subchondral bone regenerated and integrated well with the adjacent native tissue. Even better results were presented when the hydrogels were loaded with transforming growth factor- β 1, while defects in the untreated blank group still existed.

Wu *et al.* reported the properties of carboxyl-terminated poly(amidoamine) (PAMAM-COOH)-alendronate (ALN) conjugated (ALN-PAMAM-COOH) on hydroxyapatite remineralization on acid-etched enamel, both *in vitro* and *in vivo* [55]. In addition, Wang *et al.* also reported the remineralization properties of PAMAM-G3 for the treatment of dentinal tubule occlusions, affording optimal results [56]. In addition, Gao *et al.* investigated the biomineralization effects of PAMAM-G4 [57]. For comparison, sodium fluoride (NaF), being a desensitizing agent, was used as a positive control. Dentin permeability, morphology, and surface deposits were measured, and both samples were subjected to brushing and an acid challenge. The results

showed that both PAMAM and NaF reduced dentin permeabilization to significant levels, at 25.1% and 20.7%, respectively. PAMAM also showed excellent results with the creation of precipitates on dentin; it was initially slower than NaF, but then led to similar results after 28 days. In addition, PAMAM induced biomineralization, not only at the surface level on dentin surfaces, but also at a deeper level, reaching the dentinal tubules. PAMAM still showed stronger resistance to acid challenge, to a greater extent than NaF, and proved to be a more reliable and stable dentinal tubule occlusion agent. Liang *et al.* also conducted similar studies, using a composite with nanoparticles of amorphous calcium phosphate (NACP) and PAMAM, which provided positive results [58].

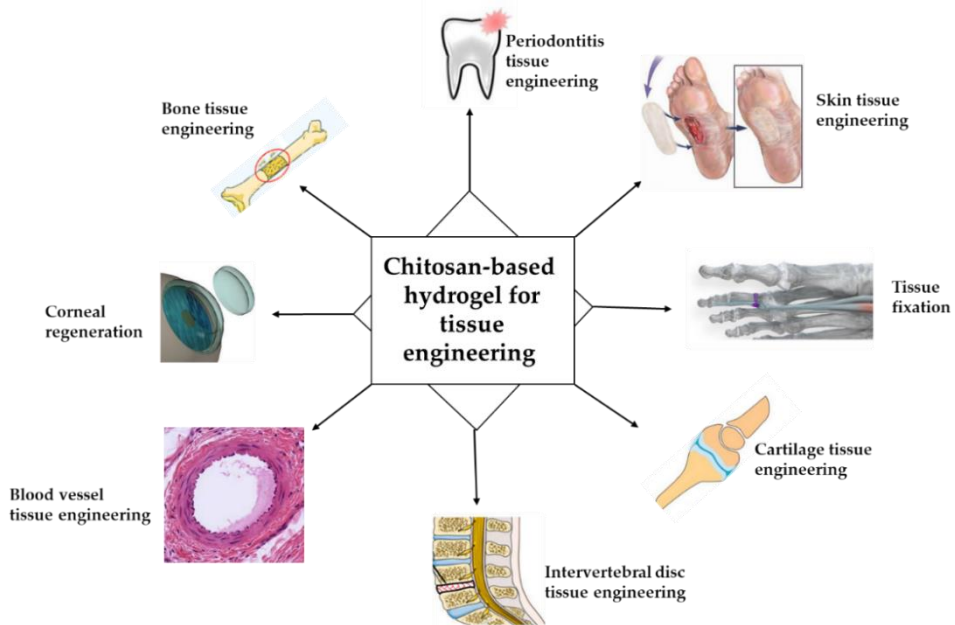


Figure 2. Schematic representation of applications of chitosan-based bioactive materials.

REFERENCES

1. Albertsson, A.C. Degradable aliphatic polyesters: Preface. *Adv. Polym. Sci.***2002**, *157*, 42249.
2. Visco, A.; Scolaro, C.; Giamporcaro, A.; De Caro, S.; Tranquillo, E.; Catauro, M. Threads made with blended biopolymers: Mechanical, physical and biological features. *Polymers (Basel)***2019**, *11*, doi:10.3390/polym11050901.
3. Sultankulov, B.; Berillo, D.; Sultankulova, K.; Tokay, T.; Saparov, A. Progress in the development of chitosan-based biomaterials for tissue engineering and regenerative medicine. *Biomolecules***2019**, *9*, doi:10.3390/biom9090470.
4. Williams, D.F. On the nature of biomaterials. *Biomaterials***2009**, *30*, 5897–5909, doi:10.1016/j.biomaterials.2009.07.027.
5. Ulery, B.D.; Nair, L.S.; Laurencin, C.T. Biomedical applications of biodegradable polymers. *J. Polym. Sci. Part B Polym. Phys.***2011**, *49*, 832–864, doi:10.1002/polb.22259.
6. Li, J.; Cai, C.; Li, J.; Li, J.; Li, J.; Sun, T.; Wang, L.; Wu, H.; Yu, G. Chitosan-based nanomaterials for drug delivery. *Molecules***2018**, *23*, 1–26, doi:10.3390/molecules23102661.
7. Muzzarelli, R.A.A.; El Mehtedi, M.; Bottegoni, C.; Aquili, A.; Gigante, A. Genipin-crosslinked chitosan gels and scaffolds for tissue engineering and regeneration of cartilage and bone. *Mar. Drugs***2015**, *13*, 7314–7338, doi:10.3390/md13127068.
8. Song, R.; Murphy, M.; Li, C.; Ting, K.; Soo, C.; Zheng, Z. Current development of biodegradable polymeric materials for biomedical

- applications. *Drug Des. Devel. Ther.***2018**, *12*, 3117–3145, doi:10.2147/DDDT.S165440.
9. Piskin, E. *Journal of Biomaterials Science, Biodegradable polymers as biomaterials.* **1994**, 37–41.
10. Tiwari, S.; Patil, R.; Bahadur, P. Polysaccharide based scaffolds for soft tissue engineering applications. *Polymers (Basel).***2018**, *11*, doi:10.3390/polym11010001.
11. Galler, K.M.; D'Souza, R.N.; Hartgerink, J.D. Biomaterials and their potential applications for dental tissue engineering. *J. Mater. Chem.***2010**, *20*, 8730–8746, doi:10.1039/c0jm01207f.
12. Rodríguez-Vázquez, M.; Vega-Ruiz, B.; Ramos-Zúñiga, R.; Saldaña-Koppel, D.A.; Quiñones-Olvera, L.F. Chitosan and Its Potential Use as a Scaffold for Tissue Engineering in Regenerative Medicine. *Biomed Res. Int.***2015**, *2015*, doi:10.1155/2015/821279.
13. Zhang, K.; Wang, S.; Zhou, C.; Cheng, L.; Gao, X.; Xie, X.; Sun, J.; Wang, H.; Weir, M.D.; Reynolds, M.A.; et al. Advanced smart biomaterials and constructs for hard tissue engineering and regeneration. *Bone Res.***2018**, *6*, doi:10.1038/s41413-018-0032-9.
14. Gao, S.; Tang, G.; Hua, D.; Xiong, R.; Han, J.; Jiang, S.; Zhang, Q.; Huang, C. Stimuli-responsive bio-based polymeric systems and their applications. *J. Mater. Chem. B***2019**, *7*, 709–729, doi:10.1039/c8tb02491j.
15. Logithkumar, R.; Keshavnarayan, A.; Dhivya, S.; Chawla, A.; Saravanan, S.; Selvamurugan, N. A review of chitosan and its derivatives in bone tissue engineering. *Carbohydr. Polym.***2016**, *151*, 172–188, doi:10.1016/j.carbpol.2016.05.049.

16. Kumar, S.; Koh, J. Physiochemical and optical properties of chitosan based graphene oxide bionanocomposite. *Int. J. Biol. Macromol.***2014**, *70*, 559–564, doi:10.1016/j.ijbiomac.2014.07.019.
17. Deepthi, S.; Venkatesan, J.; Kim, S.K.; Bumgardner, J.D.; Jayakumar, R. An overview of chitin or chitosan/nano ceramic composite scaffolds for bone tissue engineering. *Int. J. Biol. Macromol.***2016**, *93*, 1338–1353, doi:10.1016/j.ijbiomac.2016.03.041.
18. Xu, H.H.K.; Simon, C.G. Fast setting calcium phosphate-chitosan scaffold: Mechanical properties and biocompatibility. *Biomaterials***2005**, *26*, 1337–1348, doi:10.1016/j.biomaterials.2004.04.043.
19. Eliaz, N.; Metoki, N. Calcium phosphate bioceramics: A review of their history, structure, properties, coating technologies and biomedical applications. *Materials (Basel)***2017**, *10*, doi:10.3390/ma10040334.
20. Nasiri, N.; Ceramidas, A.; Mukherjee, S.; Panneerselvan, A.; Nisbet, D.R.; Tricoli, A. Ultra-Porous Nanoparticle Networks: A Biomimetic Coating Morphology for Enhanced Cellular Response and Infiltration. *Sci. Rep.***2016**, *6*, 1–11, doi:10.1038/srep24305.
21. Pistone, A.; Iannazzo, D.; Espro, C.; Galvagno, S.; Tampieri, A.; Montesi, M.; Panseri, S.; Sandri, M. Tethering of Gly-Arg-Gly-Asp-Ser-Pro-Lys Peptides on Mg-Doped Hydroxyapatite. *Engineering***2017**, *3*, 55–59, doi:10.1016/J.ENG.2017.01.007.
22. Kim, H.L.; Jung, G.Y.; Yoon, J.H.; Han, J.S.; Park, Y.J.; Kim, D.G.; Zhang, M.; Kim, D.J. Preparation and characterization of nano-sized hydroxyapatite/alginate/chitosan composite scaffolds for bone tissue engineering. *Mater. Sci. Eng. C***2015**, *54*, 20–25, doi:10.1016/j.msec.2015.04.033.

-
23. Nazeer, M.A.; Yilgör, E.; Yilgör, I. Intercalated chitosan/hydroxyapatite nanocomposites: Promising materials for bone tissue engineering applications. *Carbohydr. Polym.***2017**, *175*, 38–46, doi:10.1016/j.carbpol.2017.07.054.
24. Cordes, D.B.; Lickiss, P.D.; Rataboul, F. Recent developments in the chemistry of cubic polyhedral oligosilsesquioxanes. *Chem. Rev.***2010**, *110*, 2081–2173, doi:10.1021/cr900201r.
25. Chew, S.L.; Wang, K.; Chai, S.P.; Goh, K.L. Elasticity, thermal stability and bioactivity of polyhedral oligomeric silsesquioxanes reinforced chitosan-based microfibrils. *J. Mater. Sci. Mater. Med.***2011**, *22*, 1365–1374, doi:10.1007/s10856-011-4318-3.
26. Ha, Y.M.; Amna, T.; Kim, M.H.; Kim, H.C.; Hassan, S.S.M.; Khil, M.S. Novel silicified PVAc/POSS composite nanofibrous mat via facile electrospinning technique: Potential scaffold for hard tissue engineering. *Colloids Surfaces B Biointerfaces***2013**, *102*, 795–802, doi:10.1016/j.colsurfb.2012.09.018.
27. Argüelles-Monal, W.M.; Lizardi-Mendoza, J.; Fernández-Quiroz, D.; Recillas-Mota, M.T.; Montiel-Herrera, M. Chitosan derivatives: Introducing new functionalities with a controlled molecular architecture for innovative materials. *Polymers (Basel)***2018**, *10*, doi:10.3390/POLYM10030342.
28. Sashiwa, H.; Yajima, H.; Aiba, S.I. Synthesis of a chitosan-dendrimer hybrid and its biodegradation. *Biomacromolecules***2003**, *4*, 1244–1249, doi:10.1021/bm030021w.
29. Xu, Q.; Wang, C.-H.; Wayne Pack, D. Polymeric Carriers for Gene Delivery: Chitosan and Poly(amidoamine) Dendrimers. *Curr. Pharm.*

*Des.***2010**, *16*, 2350–2368, doi:10.2174/138161210791920469.

30. He, G.; Kong, Y.; Zheng, H.; Ke, W.; Chen, X.; Yin, Y.; Yi, Y. Preparation and Properties of Poly(amidoamine) Dendrimer/Quaternary Ammonium Chitosan Hydrogels. *J. Wuhan Univ. Technol. Mater. Sci. Ed.***2018**, *33*, 736–743, doi:10.1007/s11595-018-1886-9.

31. Abedi-Gaballu, F.; Dehghan, G.; Ghaffari, M.; Yekta, R.; Abbaspour-Ravasjani, S.; Baradaran, B.; Ezzati Nazhad Dolatabadi, J.; Hamblin, M.R. PAMAM dendrimers as efficient drug and gene delivery nanosystems for cancer therapy. *Appl. Mater. Today***2018**, *12*, 177–190, doi:10.1016/j.apmt.2018.05.002.

32. O'Brien, F.J. Biomaterials & scaffolds for tissue engineering. *Mater. Today***2011**, *14*, 88–95, doi:10.1016/S1369-7021(11)70058-X.

33. Chan, B.P.; Leong, K.W. Scaffolding in tissue engineering: General approaches and tissue-specific considerations. *Eur. Spine J.***2008**, *17*, doi:10.1007/s00586-008-0745-3.

34. Murua, A.; Herran, E.; Orive, G.; Igartua, M.; Blanco, F.J.; Pedraz, J.L.; Hernández, R.M. Design of a composite drug delivery system to prolong functionality of cell-based scaffolds. *Int. J. Pharm.***2011**, *407*, 142–150, doi:10.1016/j.ijpharm.2010.11.022.

35. Lipatov, T.E. Biocompatible polymers for medical application. *Basics Appl. Stoch. Process.***2013**, *53*, 1689–1699.

36. Ratner, B.D. The biocompatibility manifesto: Biocompatibility for the twenty-first century. *J. Cardiovasc. Transl. Res.***2011**, *4*, 523–527, doi:10.1007/s12265-011-9287-x.

37. Panwar, A.; Tan, L.P. Current status of bioinks for micro-extrusion-

- based 3D bioprinting. *Molecules***2016**, *21*, doi:10.3390/molecules21060685.
38. Ye, K.; Felimban, R.; Traianedes, K.; Moulton, S.E.; Wallace, G.G.; Chung, J.; Quigley, A.; Choong, P.F.M.; Myers, D.E. Chondrogenesis of infrapatellar fat pad derived adipose stem cells in 3D printed chitosan scaffold. *PLoS One***2014**, *9*, doi:10.1371/journal.pone.0099410.
39. Cui, Z.; Lin, L.; Si, J.; Luo, Y.; Wang, Q.; Lin, Y.; Wang, X.; Chen, W. Fabrication and characterization of chitosan/OGP coated porous poly(ϵ -caprolactone) scaffold for bone tissue engineering. *J. Biomater. Sci. Polym. Ed.***2017**, *28*, 826–845, doi:10.1080/09205063.2017.1303867.
40. Sun, B.; Ma, W.; Su, F.; Wang, Y.; Liu, J.; Wang, D.; Liu, H. The osteogenic differentiation of dog bone marrow mesenchymal stem cells in a thermo-sensitive injectable chitosan/collagen/ β -glycerophosphate hydrogel: in vitro and in vivo. *J. Mater. Sci. Mater. Med.***2011**, *22*, 2111–2118, doi:10.1007/s10856-011-4386-4.
41. Ang, T.H.; Sultana, F.S.A.; Hutmacher, D.W.; Wong, Y.S.; Fuh, J.Y.H.; Mo, X.M.; Loh, H.T.; Burdet, E.; Teoh, S.H. Fabrication of 3D chitosan-hydroxyapatite scaffolds using a robotic dispensing system. *Mater. Sci. Eng. C***2002**, *20*, 35–42, doi:10.1016/S0928-4931(02)00010-3.
42. Chavanne, P.; Stevanovic, S.; Wüthrich, A.; Braissant, O.; Pielas, U.; Gruner, P.; Schumacher, R. 3D printed chitosan / hydroxyapatite scaffolds for potential use in regenerative medicine. *Biomed. Eng. / Biomed. Tech.***2013**, *58*, 9–10, doi:10.1515/bmt-2013-4069.
43. Morris, V.B.; Nimbalkar, S.; Younesi, M.; McClellan, P.; Akkus, O. Mechanical Properties, Cytocompatibility and Manufacturability of Chitosan:PEGDA Hybrid-Gel Scaffolds by Stereolithography. *Ann. Biomed.*

Eng. **2017**, *45*, 286–296, doi:10.1007/s10439-016-1643-1.

44. Reed, S.; Lau, G.; Delattre, B.; Lopez, D.D.; Tomsia, A.P.; Wu, B.M. Macro- and micro-designed chitosan-alginate scaffold architecture by three-dimensional printing and directional freezing. *Biofabrication* **2016**, *8*, 15003, doi:10.1088/1758-5090/8/1/015003.

45. Madihally, S. V.; Roehm, K.D. Bioprinted chitosan-gelatin thermosensitive hydrogels using an inexpensive 3D printer. *Biofabrication* **2017**, *10*, 015002.

46. Ross, D.E. Review of longitudinal studies of MRI brain volumetry in patients with traumatic brain injury. *Brain Inj.* **2011**, *25*, 1271–1278, doi:10.3109/02699052.2011.624568.

47. Huang, J.; Fu, H.; Wang, Z.; Meng, Q.; Liu, S.; Wang, H.; Zheng, X.; Dai, J.; Zhang, Z. BMSCs-laden gelatin/sodium alginate/carboxymethyl chitosan hydrogel for 3D bioprinting. *RSC Adv.* **2016**, *6*, 108423–108430, doi:10.1039/c6ra24231f.

48. Paquin, F.; Rivnay, J.; Salleo, A.; Stingelin, N.; Silva, C. Multi-phase semicrystalline microstructures drive exciton dissociation in neat plastic semiconductors. *J. Mater. Chem. C* **2015**, *3*, 10715–10722, doi:10.1039/b000000x.

49. Lu, N.; Lu, Y.; Liu, S.; Jin, C.; Fang, S.; Zhou, X.; Li, Z. Tailor-Engineered POSS-Based Hybrid Gels for Bone Regeneration. *Biomacromolecules* **2019**, *20*, 3485–3493, doi:10.1021/acs.biomac.9b00771.

50. Chen, M.; Zhang, Y.; Xie, Q.; Zhang, W.; Pan, X.; Gu, P.; Zhou, H.; Gao, Y.; Walther, A.; Fan, X. Long-Term Bone Regeneration Enabled by a Polyhedral Oligomeric Silsesquioxane (POSS)-Enhanced Biodegradable

- Hydrogel. *ACS Biomater. Sci. Eng.* **2019**, *5*, 4612–4623, doi:10.1021/acsbiomaterials.9b00642.
51. Xavier, J.R.; Thakur, T.; Desai, P.; Jaiswal, M.K.; Sears, N.; Cosgriff-Hernandez, E.; Kaunas, R.; Gaharwar, A.K. Bioactive nanoengineered hydrogels for bone tissue engineering: A growth-factor-free approach. *ACS Nano* **2015**, *9*, 3109–3118, doi:10.1021/nm507488s.
52. Zhang, Y.; Chen, M.; Tian, J.; Gu, P.; Cao, H.; Fan, X.; Zhang, W. In situ bone regeneration enabled by a biodegradable hybrid double-network hydrogel. *Biomater. Sci.* **2019**, *7*, 3266–3276, doi:10.1039/c9bm00561g.
53. Nguyen, L.H.; Kudva, A.K.; Saxena, N.S.; Roy, K. Engineering articular cartilage with spatially-varying matrix composition and mechanical properties from a single stem cell population using a multi-layered hydrogel. *Biomaterials* **2011**, *32*, 6946–6952, doi:10.1016/j.biomaterials.2011.06.014.
54. Han, F.; Yang, X.; Zhao, J.; Zhao, Y.; Yuan, X. Photocrosslinked layered gelatin-chitosan hydrogel with graded compositions for osteochondral defect repair. *J. Mater. Sci. Mater. Med.* **2015**, *26*, doi:10.1007/s10856-015-5489-0.
55. Wu, D.; Yang, J.; Li, J.; Chen, L.; Tang, B.; Chen, X.; Wu, W.; Li, J. Hydroxyapatite-anchored dendrimer for in situ remineralization of human tooth enamel. *Biomaterials* **2013**, *34*, 5036–5047, doi:10.1016/j.biomaterials.2013.03.053.
56. Wang, T.; Yang, S.; Wang, L.; Feng, H. Use of poly (amidoamine) dendrimer for dentinal tubule occlusion: A preliminary study. *PLoS One* **2015**, *10*, doi:10.1371/journal.pone.0124735.
57. Gao, Y.; Liang, K.; Li, J.; Yuan, H.; Liu, H.; Duan, X.; Li, J. Effect and

Stability of Poly(Amido Amine)-Induced Biomineralization on Dentinal Tubule Occlusion. *Materials (Basel)*.**2017**, *10*, 1–15, doi:10.3390/ma10040384.

58. Liang, K.; Weir, M.D.; Xie, X.; Wang, L.; Reynolds, M.A.; Li, J.; Xu, H.H.K. Dentin remineralization in acid challenge environment via PAMAM and calcium phosphate composite. *Dent. Mater.***2016**, *32*, 1429–1440, doi:10.1016/j.dental.2016.09.013.

4. COATINGS AGAINST MARINE FOULING

The term biofouling refers to the phenomenon of accumulation and deposition of living organisms, animals and plants, unicellular or multicellular, on natural or artificial submerged surfaces. This event constitutes a problem that must be contrasted and controlled especially when hydrodynamically efficient surfaces (e.g. boat hulls, pipes, hulls of boats, pipes) are needed.

Biofouling can be schematically represented as an ecological succession [1] in which the microfouling (or biofilm), consisting of bacteria, unicellular algae and cyanobacteria, occurs in an ecological succession. In this process cyanobacteria settlement on the surfaces preparing them to the attack of macrofouling, constituted by the settlement of larger marine organisms of both plant origin (macroalgae) and animals (serpulids, barnacles, bivalves, sponges and more).

To counteract the attack of organisms with strong adhesive capacities, antifouling coatings that contain molecules with a biocidal action that are released at different times and at different concentrations depending on the matrices in which they are incorporated, can be used. Some substances with biocidal action and high effectiveness used over the years have shown high levels of toxicity in the various compartments of the marine environment (sediments, water column, organisms). An example is given by organotin compounds (e.g. TBT), whose use as antifoulants has been banned following the indications of the IMO and of the International Convention (AFS) adopted on October 5, 2002 by the Member States of the European Union.

Recently, coatings based on copper compounds, the most widely used to date, have also been banned in Sweden [2].

An alternative to coatings containing biocides could be the use of polymers with a fouling-release action, whose action does not prevent the formation of biofouling but facilitates the detachment of biofouling, due to the weak interactions that are created between the matrix and the organisms. There are more than 4000 species of "foulers" each with its own characteristics. The two broad categories into which the division can be made are:

- **MICROFOULING:** characterized by foulers of very small size (micrometer size), form the famous slime, mainly formed by sea mold, diatoms and unicellular organisms. They can affect the resistance to the motion of the ship up to a maximum of 10 %.
- **MACROFOULING:** characterized by foulers more bulky (they reach thicknesses of several centimeters) than the micro category, include algae of considerable size and animal fouling. They can affect up to 40% the resistance to the motion of the ship. In addition to increasing resistance, they also corrode and damage first the paint and then the hull later.

The phenomenon occurs from the moment the ship plunges into the sea or ocean waters. In the first phase, dissolved organic matter and molecules such as polysaccharides, proteins and protein fragments accumulate on the hull. A few hours later, the second phase begins, giving the basis for the subsequent ones. In fact, in this phase a thin microbiotic film of bacteria and unicellular organisms such as diatoms (slime) forms, followed by a secretion of mucopolysaccharides create a solid base for the settlement of

macrofouling. This slime will greatly affect the performance of the vessel, increasing the resistance to movement between 2% and 10%.

The presence of adhesive substances and the roughness caused by the irregular microbiotic colonies then favors the settlement of many other particles and organisms, thus beginning the third phase in which mainly algal spores, fungi and marine protozoa are established. In addition, this phase will see the transition from the microbiotic film to a much more complex organic coating that is typically characterized by multicellular marine organisms, herbivores and decomposers. Finally, in the fourth and last phase of the fouling process, the biological attachment is strongly intensified and mainly macroalgae grow on the hull, such as green algae (Enteromorpha) and brown algae (Ectocarpus), which have an extraordinary reproductive potential and a strong resistance to widespread environmental fluctuations, especially with regard to salinity and dryness, making the detachment very complicated. Another protagonist of this phase is the animal fouling composed mainly by barnacles, molluscs, bryozoans and tubificids. The "animal" fouling compared to the already mentioned "slime" drastically reduces the efficiency of the ship (40%) and must be eliminated and avoided as much as possible. (Fig. 1)

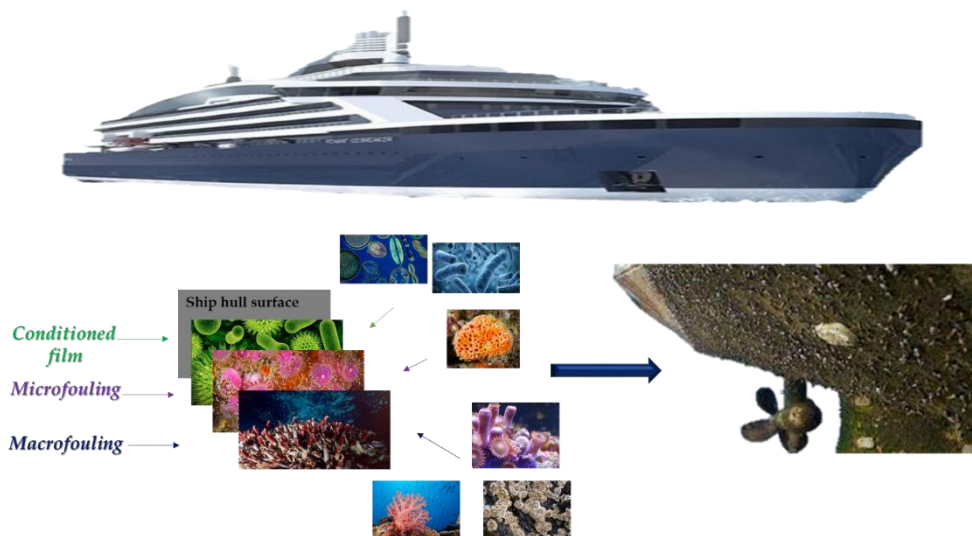


Figure 1. Hull surface fouling process and main fouling organisms.

The development of marine biofouling depends on multiple factors such as water temperature, nutrient level, frequency of currents, salinity and pH of the marine environment and the properties of the hull material. In addition to environmental factors, surface properties such as surface energy, wettability, mechanical strength, and surface topography are also influential. Several studies have shown that a surface with energy values between 20 and 30 mJ/m², known as the “Baier’s minimum”, represents the minimum adhesion condition for microorganisms. (Fig. 2) It also depends on geographical factors such as geographic area and time of year. The most aggressive phase occurs when the ship docks in port especially in the presence of tropical waters. Therefore, antifouling marine coatings must not only be highly effective and guarantee at least 5 years of constant protection between dockings, but they must also have, in most cases, a broad spectrum of action so as to be able to combat the most common types of pollution. Each

ship should have its own anti-fouling paint best suited to its own purposes and needs environmental, speed and cargo needs.

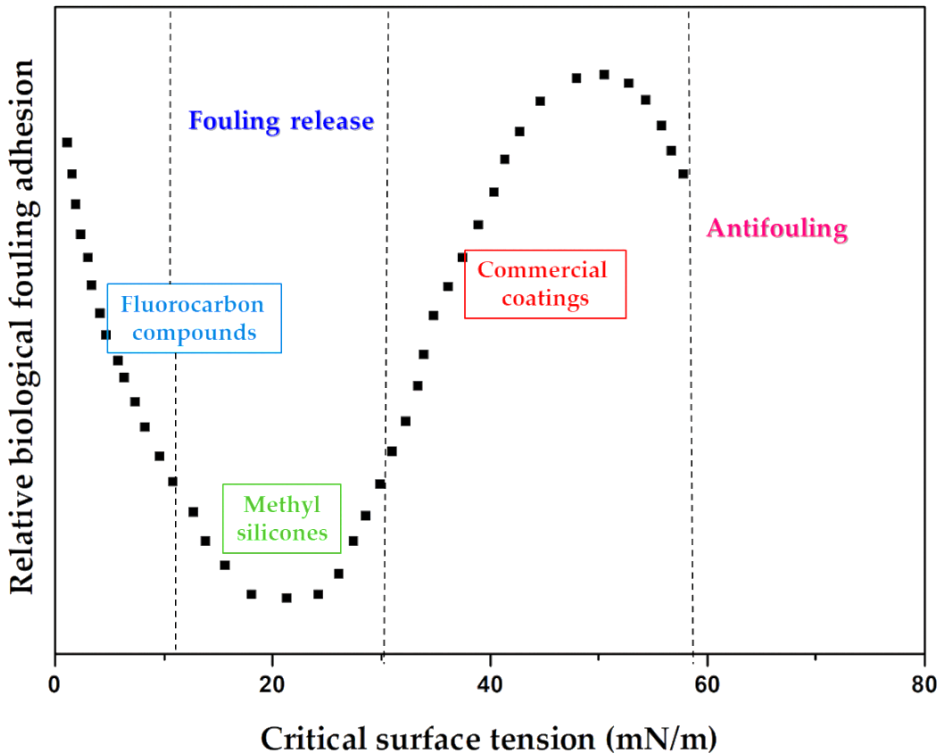


Figure 2. A Baier curve plotting the degree of fouling versus critical surface tension.

Therefore, after the middle of the 19th century, anti-fouling paints took over from all other technologies patented up to that time [3]. The most common type of antifouling paints contain biocides, i.e. poisonous substances applied to the hull with the aim of killing micro or macro organisms causing biofouling and thus preserving the shape and integrity of the hull. One of the most effective paint was patented in 1950 based on tributyltin compounds (called TBT) which guaranteed effectiveness on a wide range of species and a duration of 5 years. This paint, however, was the cause of impotence and sterilized some marine species that could not reproduce and risked

extinction. As a result, this technology (TBT) was banned in November 1999 by the IMO (International Maritime Organization), with a ban on the application of paints with organotin compounds from January 1, 2001 and a total ban from January 1, 2008. When the era of organotin compounds ended, the aim was not only to eliminate fouling that had already settled on the hull, but also to prevent its formation by guaranteeing a certain level of smoothness and thus, to reduce the friction of the ship's motion to a minimum. For a certain period in the years following the IMO ban, new copper-based release (by motion) and ablative (by resting period) technologies were used. However, also in this case, environmental problems have been registered since the metals present in the paints bio accumulate in the environment, creating sediments that can become toxic at high levels and remain hidden for years.

So, over time, attempts were made to increase the number of biocides in order to reduce the amount of copper and metals, even though the organic effects of biocides have not yet been fully discovered and revealed, as well as the consequences that they can generate in the environment. The research in this field led, recently, to the discovery of the coatings of the future known as "foul release" and "biocide free", which offer an excellent compromise between a high level of environmental respect and efficient performance. These coatings are composed of functional polymer chains that are released onto the immersed surface of the ship's hull, thus avoiding the release of possibly toxic biocides. Polymer chains are more likely to inhibit biofouling and bio corrosion due to their incorporation of functional anti-adhesion, anti-microbial and anti-corrosion chains than biocide release. Several functional

polymer-based coatings and paints have been developed in recent years and others are under development. The three most widely investigated types of marine coatings are (Fig. 3):

- **Antifouling coatings:** they prevent the attachment of "foulers" to the surface;
- **Fouling release coatings:** they reduce the adhesion between marine organisms and the materials of which the immersed surfaces are composed;
- **Super hydrophobic coatings:** they can produce a reduction in frictional resistance, thereby increasing fuel efficiency, and can also reduce corrosion and prevent the growth of marine organisms on a ship's hull.

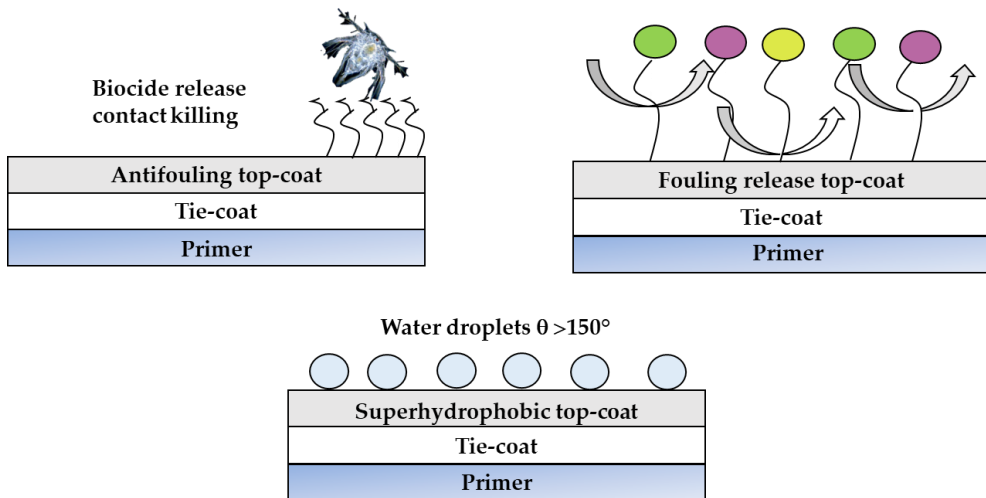


Figure 3. Schematic representation of the three types of coatings.

The main approaches of these three types of coatings involve the use of homogeneous surfaces such as hydrophobic, hydrophilic or amphiphilic surfaces, and heterogeneous surfaces such as patterned or mixed surfaces [4]. The polymers most commonly used for coatings development are shown in Figure 4, and will be discussed in the following sections.

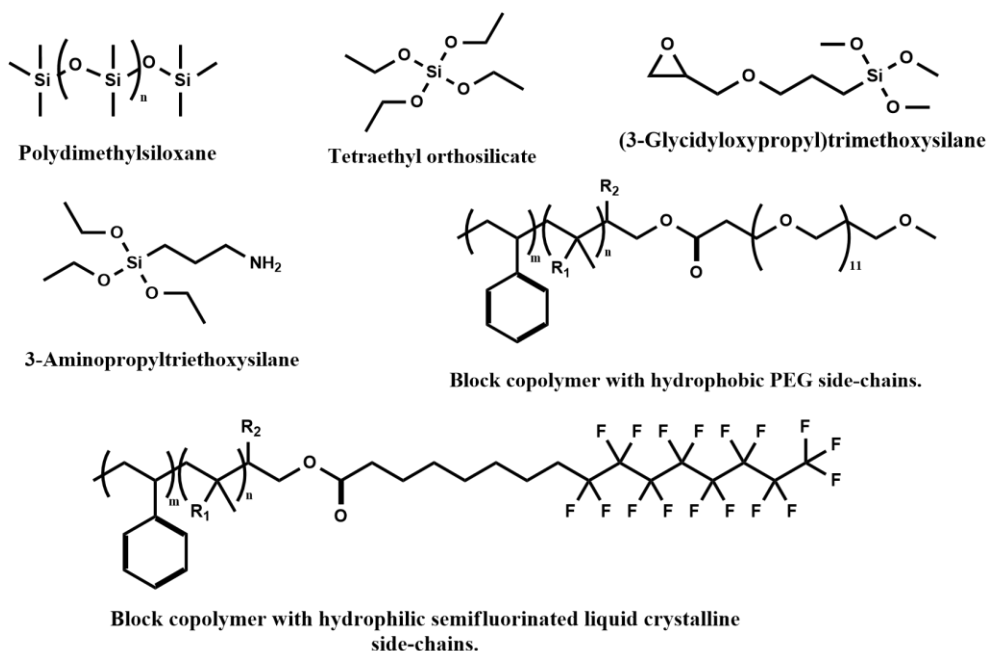


Figure 4. Polymers most commonly used for the preparation of coatings against biofouling.

4.1 Homogenous surfaces

Homogeneous surfaces include hydrophobic, hydrophilic or amphiphilic, surfaces with both hydrophobic and hydrophilic functionalities. Hydrophobic surfaces that are efficient for fouling release include coatings of fluorinated polymers and poly(dimethyl siloxane) polymers; whereas coatings using poly(ethylene glycol) polymers are hydrophilic and have antifouling properties. Thus, amphiphilic surfaces can be designed to have both foulant release and antifouling properties, as in the case of polymers with both fluorinated and poly(ethylene glycol) areas in their chain.

Callow *et al.* studied self-assembled monolayers (SAMs) of ω -substituted alkanethiolates on gold with different wettabilities to determine the adhesion strength of marine species [5–8]. The authors used methyl groups (CH₃), hydroxyl groups (OH), and a mixture or template of CH₃ and OH groups as chain endings for the alkanethiolates to create surfaces with

contact angles ranging from 20° (hydrophilic surface) to 110° (hydrophobic surface) [5]. The antifouling properties of these surfaces were tested against zoospores of the seaweed *Ulva linza*, observing that the rate of zoospore attachment was lowest on hydrophilic SAMs with terminal OH groups and highest on hydrophobic SAMs containing terminal CH_3 groups. In the case of surfaces with mixed terminal groups and patterned surfaces, the same trend was observed. As the surface became more hydrophilic, the number of deposited zoospores decreased. It has been reported in literature that the displacement of water molecules is facilitated by hydrophobic interactions [9]. Thus, such interactions strengthen surface-adhesive bonds. Callow *et al.* showed that zoospores that tried to settle on hydrophilic surfaces could not form such a strong adhesive bond and were easily displaced [5]. SAMs of alkane-thiols with short-chain oligo(ethylene glycol) (OEG) and $\text{SO}_3^-/\text{N}^+(\text{CH}_3)_3$ (SA/TMA) and terminal CH_3 were compared with long-chain poly(sulfobetaine methacrylate) (pSBMA) and poly(oligo((ethylene glycol) methyl ether methacrylate) (pOEGMA) zwitterionic groups by Cheng *et al.* [10]. The biological assays were performed on two bacterial species, *Staphylococcus epidermidis* and the Gram-negative *Pseudomonas aeruginosa*. The pSBMA zwitterionic surfaces showed the greatest reduction in bacterial adhesion and accumulation, due to the presence of strong hydration caused by electrostatic interactions, long chains and high densities. In addition, these surfaces exhibit high resistance to nonspecific protein adsorption, making them promising materials as antifoulants [11,12].

A hydrophobic surface with low surface energy, on the other hand, can be achieved using fluorinated polymers due to their apolar character [13].

Krishnan *et al.* investigated a block copolymer with semi-fluorinated liquid crystalline side chains whose contact angle with water is 120° . This copolymer was found to be effective in preventing the settlement and release of *Ulva alga* spores.[14] Fouling release was comparable to that of the most commonly used coating, polydimethylsiloxane (PDMS). In addition, the low surface energy may be responsible for the weak adhesion. However, the copolymer was not effective in the release of *Navicula* diatom cells. Another type of polymer with high surface energy and hydrophilic characteristics is poly(ethylene glycol) (PEG) [15]. PEG polymers are resistant to protein and cell adhesion due to steric repulsion of adhesion molecules, large exclusion volume, and high mobility [16,17]. Krishnan *et al.* also studied a block copolymer with PEGylated side chains and a water contact angle of 78° . The copolymer was more effective in releasing *Navicula* diatom cells than the PDMS surface, but also in preventing *Ulva alga* settlement. The hydrophilic surface allowed the adhesive to spread over a larger area and to produce a lower contact angle between the adhesive and the surface, which led to a stronger attachment to the surface [8,18]. Dalsin *et al.* conjugated a methoxy-terminated PEG polymer (mPEG) with the amino acid L-3,4-dihydroxyphenylalanine (DOPA), in order to increase the adhesive properties of the polymer to the substrates. DOPA is present in large amounts in the adhesive proteins of mussels [19,20]. Titanium substrates were modified with the mPEG-DOPA polymer affording highly hydrophilic surfaces with a water contact angle of 33° . This polymer was more effective than PDMS in preventing settlement and in allowing the release of the diatom *Navicula perminuta* and the *alga Ulva* zoospores (Fig. 5) [19].

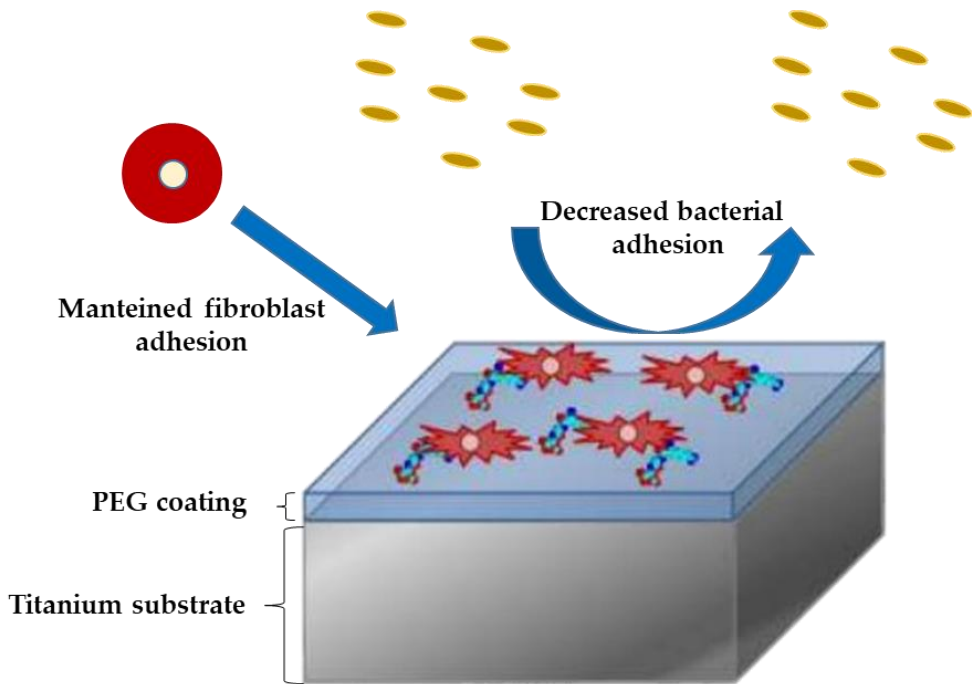


Figure 5. Mechanism of PEG-functionalized PDMS-based coatings.

Poly(dimethyl siloxane) (PDMS) has been widely used in the area of antifouling coatings and other fields due to its unique combination of properties including low elastic modulus and low glass transition temperature. The disadvantage of PDMS in some applications is its hydrophobic surface, which results in non-specific protein adsorption and wettability issues [21]. Poly(ethylene glycol)-based block copolymers and surfactants have been added to PDMS coatings and films to impart biofouling resistance and hydrophilicity to the surface with successful results. Camós Noguier *et al.* synthesized a novel fluorescent PEG-*b*-PDMS-*b*-PEG "triblock" copolymer and added it to a PDMS coating. The surface activity and fouling resistance of the synthesized copolymer were confirmed by water contact angle measurements and seawater immersion experiments [22].

Advances in nanomaterial science are associated with developments in fabrication methods in terms of energy conservation, environmental compatibility, and low cost. Selim *et al.* have successfully developed a series of self-cleaning technologies using siloxane polymers functionalized with magnetite nanoparticles. Such nanocomposite systems are dynamic non-stick surfaces and discourage any fouling attack through physical anti-adhesion. A series of superhydrophobic nanocomposites were synthesized via solution casting using different filler concentrations of nano-magnetite. PDMS/magnetite nanomodels possess numerous advantages, such as simplicity, non-toxicity, environmental sustainability, commercial viability, low fuel consumption, and desirable self-cleaning surfaces with durability characteristics [23].

Guo *et al.* developed a novel amphiphilic coating incorporating poly (N-vinylpyrrolidone) (PVP), a highly hydrophilic polymer with strong chemical-physical stability, polydimethylsiloxane (PDMS) matrix. PVP was first functionalized with triethoxysilane and then directly cross-linked with PDMS to form an amphiphilic network coating at room temperature. The results suggested that the hydrophilicity of the PDMS matrix was significantly improved after the change. In addition, the PDMS-PVP coatings could effectively prevent the adhesion of *Navicula* bacteria and diatoms (99% reduction), as well as resist the attack of *Cyrripedes mimeticus* (82% reduction). Wettability tests performed on these samples show that PDMS has a contact angle $\sim 108^\circ$, thus indicating its high hydrophobicity; in contrast, the hydrophilicity of PDMS-PVP coatings could be significantly improved and was directly proportional to the PVP-IPTS content (contact angle decreased

from 99° to 84° with 5% to 15% PVP-IPTS), while when the PVP-IPTS content is 20%, the mechanical strength of amphiphilic coatings decreases. The anti-biofouling performance of PDMS-PVP coatings was also investigated. The samples, immersed in seawater for 4 months, showed that a large number of marine organisms were observable on the surfaces of the PVC control panel and PDMS panel. On the other hand, the PDMS-PVP coated panels showed a significant improvement in anti-fouling performance. In particular, the PDMS-PVP-15 sample showed almost no obvious fouling binding for long-term evaluation, indicating that this coating was highly stable and promising to be applied in the field of marine antifouling [24].

Patterson *et al.* studied poly-(dimethyl-siloxane) (PDMS)- and poly(ethylene oxide) (PEO) block copolymer coatings functionalized with amphiphilic side chains, surfactants, and sequence-controlled oligomers to directly compare the effects of hydrophilicity, hydrogen bonding, and monomer sequence on antifouling performance. Amphiphilic character was imparted with oligopeptide and oligopeptoid chains made from oligo-PEOs and surface-segregating fluoroalkyl units. Biofouling tests with *Ulva linza* showed that the presence of peptoid side chains facilitated the removal of spores from the PDMS-based copolymer, with removal corresponding to that of a standard PDMS elastomer. The lack of a hydrogen bond donor in the peptoid backbone likely contributed to the lower adhesion strength of these surfaces. Both the initial attachment and adhesion strength of the uncertain *Navicula* diatom were lower on PEO-based coatings than on PDMS-based coatings. For the PEO coating that carried the blocking peptoid sequence, the initial

attachment of *Navicula incerta* showed no measurable cell density (Fig. 6) [25].

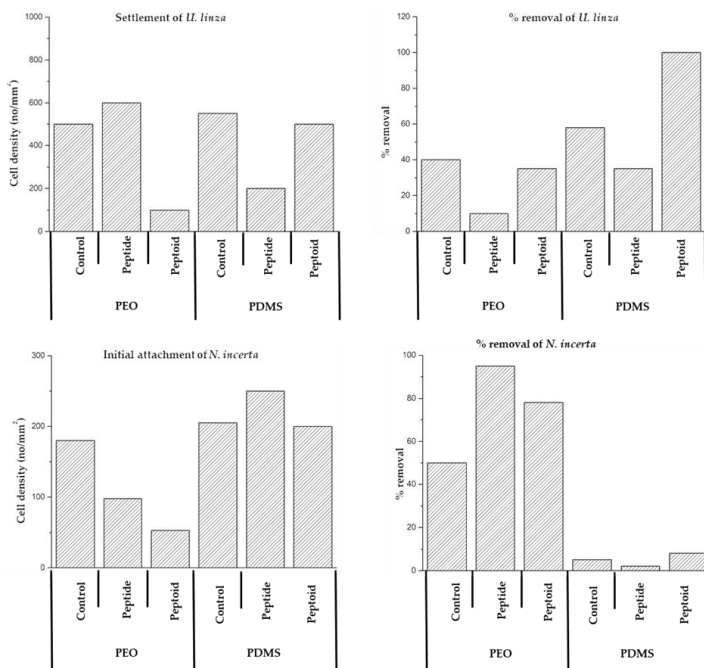


Figure 6. Results of coatings synthesized by Patterson et al. [25] on *U. linza* spores and *N. incerta* cells.

4.2 Heterogeneous surfaces

Another important approach in designing surfaces to inhibit biofouling focuses on heterogeneous surfaces, which include patterned surfaces or surfaces with a mixed character. These surfaces are usually designed to have both hydrophobic and hydrophilic areas. An example of a mixed surface is the phase-separated hydrophobic and hydrophilic PDMS domains groups of quaternary ammonium salts, while a patterned surface can have alternating strips of hydrophobic and hydrophilic polymers. The complexity of these surfaces with different chemistry and domain sizes can further enhance the deterrence of the marine biofouling properties.

Qin *et al.* developed a series of PDMS-b-QPDMAEMA block copolymers with different contents of quaternary ammonium salt groups by RAFT polymerization and quaternization. These well-defined copolymers generate a special composition and morphology on the film surfaces, which allows a greater understanding of the structure-activity antimicrobial relationship. The antimicrobial activity was found to be highly dependent on surfaces with heterogeneous morphology and higher N⁺ content, and PDMS-b-QPDMAEMA100 showed superior and broad-spectrum antimicrobial activity [26]. Liu *et al.* incorporated quaternary ammonium salts (QAS)-based biocides *in situ* to PDMS for fouling release and antifouling coatings. Two different PDMS systems, one bound with QAS and one incorporated with quaternary ammonium-functionalized polyhedral oligomeric silsesquioxanes (Q-POSS) were studied in air, water, and artificial seawater. Interestingly, in the QAS-bound PDMS system, polymers prepared from octadecyldimethyl(3-triethoxysilylpropyl) ammonium chloride (TES-QAS) resulted in better antifouling coatings. The results showed that the different reaction dynamics of methoxysilane and ethoxysilane can lead to different surface structures, resulting in different antifouling activities. In particular, it was shown that a lower degree of quaternization provides more freedom for the alkyl groups to extend and penetrate microbial membranes, thus neutralizing microorganisms on contact. In summary, the degree of extension of alkyl chains in QAS plays an important role in preventing bacterial biofilm growth [27]. Thermosetting siloxane-urethane coatings have been studied using high-throughput combinatorial methods by Bodkhe *et al.* [28]. These methods allow for rapid synthetic testing as well as screening

of a large number of coatings [29,30]. The siloxane-urethane polymer mixed with a cross-linker self-assembles into microstructured domains. The characteristics of the domains depend on the mixing time after addition of the cross-linker [31,32]. The water contact angles were similar for all coatings and closer to the values of PDMS than urethane, about 103°. PDMS has a lower surface energy and predominates at the surface. Biological assays showed that micro separated surfaces had the lowest release force. The design of cross-linked systems based on urethane and epoxy groups with a self-stratifying capability is one of the most promising approaches to develop antifouling coatings with improved mechanical and adhesion properties. Cross-linked poly(siloxane)-poly(urethane) (PU) self-stratified coatings have also been extensively studied by Webster *et al.* [29,30,33,34]. The first systems reported by Majundar and Webster consisted of cross-linked PDMS-PU coatings that exhibited microtopographic surface domains of PDMS on a PU matrix background, formed spontaneously by phase separation during film formation [31]. These coatings showed a significant decrease in the adhesive strength of *Amphibalanus Amphitrite* barnacles and prompted further studies of a variety of PDMS-PU systems. This could be due to the formation of the domains with uniform size, which were evenly distributed across the surface [32]. Imbesi *et al.* developed a two-dimensional matrix of hyperbranched fluoropolymer (HBFP) networks cross-linked with poly(ethylene glycol) by method of co-deposition and polymerization of HBFP with varying ratios of PEG, towards optimization for applications as marine anti-biofouling coatings. Blending the incompatible polymers resulted in coatings with different physical, mechanical, and anti-biofouling properties that depended

on the polymer composition and the amount of cross linker used. Unique surface effects occurred with water swelling, resulting in increased hydrophobicity and increased surface roughness. Overall, the tests provided information on how polymer composition and the amount of cross linker affect the thermal, surface, mechanical, and anti-biofouling properties [35].

(Fig. 7)

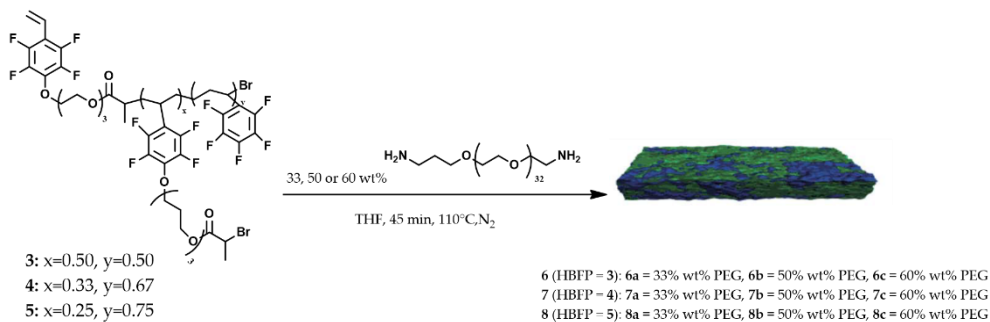


Figure 7. Crosslinking strategy for the preparation of HBFP–PEG coatings at varying HBFP compositions and PEG concentrations. [35]

Pollack *et al.* synthesized a series of ternary amphiphilic coatings using HBFP, PEG, and PDMS [36]. It has been shown that heterocomplexity and surface energy are explicitly functions of chemical composition and that these systems are promising for use as antibiofouling coatings. By differing from previous fluoropolymer-PEG systems through the incorporation of PDMS, this system also provided an entirely new mode of dynamic surface reorganization, as demonstrated by the preferential emergence of the PDMS character on the surface after water immersion, and which differs from the predominant fluoropolymer expression observed in previous HBFP-PEG formulations. By varying the composition ratios of the three constituents, a wide range of topographical, morphological, and compositional variations

were visualized. All these features provide a new type of amphiphilic surface promising antibiofouling material. In the area of fluorinated polymers, perfluoropolyether (PFPE) graft terpolymers have high chemical resistance and low surface energy, but at the same time are very flexible [37]. Coatings were made by Yarbrough *et al.* using a random terpolymer and three different classes of monomers [38]. One of the classes of monomers contains butyl acrylate (BA) or methyl methacrylate (MMA). These polymers showed water contact angles of 117°. Another class was based on glycidyl methacrylate (GMA), a cross-linkable functional group. Crosslinking was used to prevent surface reorganization in an aqueous environment by limiting chain mobility. These polymers were characterized by water contact angles of about 120°. The MMA-GMA-based polymers showed a lower settlement density of *Ulva* zoospores than glass, 10% lower, and PDMS elastomer, 25% lower. Another widely investigated class of polymers, is that of hybrid xerogels incorporating organic groups are more flexible and less prone to breakage. Tang *et al.* fabricated hybrid xerogels from alkoxysilane with n-propyl, 3,3,3-trifluoropropyl, n-octyl, and ethylene diamine groups [39]. The ethylene diamine groups are hydrophilic, while the other three groups are hydrophobic. Alkylsilyl and amino-containing silyl residues are found on the surface of xerogel films. This gives the different hydrophobicity and surface tension properties to the films. The authors showed that the settlement of zoospores and spores of *Ulva* and *Balanus Amphitrite* cyprids was lower for xerogels than for standard glass. The n-octyl xerogels had the highest removal of spores and juvenile barnacles. More recently McMaster *et al.* developed hybrid coatings active xerogels with covalently sequestered

catalysts [40]. The xerogel composition was 50 mol% aminopropyltriethoxysilane (APTES)/50 mol% tetraethoxysilane (TEOS) or 10 mol% APTES/90 mol% TEOS doped with 0.015 M 4-(hydroxymethyl)phenyl benzyl selenoxide (Sel) or 0.015 M 3-(n-hexyltelluro)-1-propanol (Tel). The APTES/TEOS-based xerogels showed a water contact angle of 34°, while the 10/90 APTES/TEOS xerogels had a contact angle of 54°. All coatings showed lower settlement of *Ulva* zoospores than standard glass. The lowest settlement observed was on the 10/90 APTES/TEOS surfaces. The surfaces were also tested using cypris larvae of *Balanus Amphitrite* and larvae of the tapeworm *Hydroides elegans*, and the lowest settlement was observed on the xerogel containing the catalysts. Saravanan *et al.* have more recently developed silane-treated nanoparticles reinforced with diglycidyl epoxy resin to fabricate surface functionalized nanohybrid epoxy coatings. The effect of the inorganic nanoparticles on corrosion and fouling resistance properties was investigated at various filler loading concentrations (1, 3, 5, and 7 wt %). Diglycidyl epoxy resin (DGEBA) was commonly used for coating. 3-Aminopropyltriethoxysilane (APTES) was used as a coupling agent to surface treat TiO₂ nanoparticles. The nanohybrid coating (3 wt% APTES and TiO₂) showed corrosion resistance up to 108 Ucm² after 30 days of immersion in a 3.5% NaCl solution, indicating excellent corrosion resistance [41].

REFERENCES

1. Candries, M.; Atlar, M.; Mesbahi, E.; Pazouki, K. The measurement of the drag characteristics of tin-free self-polishing co-polymers and fouling release coatings using a rotor apparatus. *Biofouling* **2003**, *19*, 27–36, doi:10.1080/0892701021000026138.
2. Price, R.G.A.; Readman, W.J. Late Lesson II Chapter 12 - Booster biocide antifoulants: is history repeating itself? *Late lessons from early Warn. Sci. precaution, Innov.* **2013**, 265–278.
3. NRL The History of the Prevention of Fouling. *Mar. Fouling Its Prev.* **1952**, 211–222.
4. Grozea, C.M.; Walker, G.C. Approaches in designing non-toxic polymer surfaces to deter marine biofouling. *Soft Matter* **2009**, *5*, 4088–4100, doi:10.1039/b910899h.
5. Callow, M.E.; Callow, J.A.; Ista, L.K.; Coleman, S.E.; Nolasco, A.C.; Lopez, G.P. Use of self-assembled monolayers of different wettabilities to study surface selection and primary adhesion processes of green algal (Enteromorpha) zoospores. *Appl. Environ. Microbiol.* **2000**, *66*, 3249–3254, doi:10.1128/AEM.66.8.3249-3254.2000.
6. Finlay, J.A.; Callow, M.E.; Ista, L.K.; Lopez, G.P.; Callow, J.A. The influence of surface wettability on the adhesion strength of settled spores of the green alga Enteromorpha and the diatom Amphora. *Integr. Comp. Biol.* **2002**, *42*, 1116–1122, doi:10.1093/icb/42.6.1116.
7. Ista, L.K.; Callow, M.E.; Finlay, J.A.; Coleman, S.E.; Nolasco, A.C.; Simons, R.H.; Callow, J.A.; Lopez, G.P. Effect of substratum surface chemistry and surface energy on attachment of marine bacteria and algal

- spores. *Appl. Environ. Microbiol.* **2004**, *70*, 4151–4157, doi:10.1128/AEM.70.7.4151-4157.2004.
8. Callow, J.A.; Callow, M.E.; Ista, L.K.; Lopez, G.; Chaudhury, M.K. The influence of surface energy on the wetting behaviour of the spore adhesive of the marine alga *Ulva linza* (synonym *Enteromorpha linza*). *J. R. Soc. Interface* **2005**, *2*, 319–325, doi:10.1098/rsif.2005.0041.
9. Fletcher, M. *Bacterial Adhesion: Molecular and Ecological Diversity*, ed. M.Fletcher, Wiley-Liss, New York, NY, 1996, pp.1–24. **1997**, *3*, 4–5.
10. Cheng, G.; Zhang, Z.; Chen, S.; Bryers, J.D.; Jiang, S. Inhibition of bacterial adhesion and biofilm formation on zwitterionic surfaces. *Biomaterials* **2007**, *28*, 4192–4199, doi:10.1016/j.biomaterials.2007.05.041.
11. Chang, Y.; Chen, S.; Zhang, Z.; Jiang, S. Highly protein-resistant coatings from well-defined diblock copolymers containing sulfobetaines. *Langmuir* **2006**, *22*, 2222–2226, doi:10.1021/la052962v.
12. Zhang, Z.; Chen, S.; Chang, Y.; Jiang, S. Surface grafted sulfobetaine polymers via atom transfer radical polymerization as superlow fouling coatings. *J. Phys. Chem. B* **2006**, *110*, 10799–10804, doi:10.1021/jp057266i.
13. Krishnan, S.; Kwark, Y.J.; Ober, C.K. Fluorinated polymers: Liquid crystalline properties and applications in lithography. *Chem. Rec.* **2004**, *4*, 315–330, doi:10.1002/tcr.20022.
14. Krishnan, S.; Wang, N.; Ober, C.K.; Finlay, J.A.; Callow, M.E.; Callow, J.A.; Hexemer, A.; Sohn, K.E.; Kramer, E.J.; Fischer, D.A. Comparison of the fouling release properties of hydrophobic fluorinated and hydrophilic PEGylated block copolymer surfaces: Attachment strength of the diatom *Navicula* and the green alga *Ulva*. *Biomacromolecules* **2006**, *7*, 1449–1462,

doi:10.1021/bm0509826.

15. Long, H.P.; Lai, C.C.; Chung, C.K. Polyethylene glycol coating for hydrophilicity enhancement of polydimethylsiloxane self-driven microfluidic chip. *Surf. Coatings Technol.* **2017**, *320*, 315–319, doi:10.1016/j.surfcoat.2016.12.059.

16. Zhi, Z.; Su, Y.; Xi, Y.; Tian, L.; Xu, M.; Wang, Q.; Padidan, S.; Li, P.; Huang, W. Dual-Functional Polyethylene Glycol-b-polyhexanide Surface Coating with in Vitro and in Vivo Antimicrobial and Antifouling Activities. *ACS Appl. Mater. Interfaces* **2017**, *9*, 10383–10397, doi:10.1021/acsami.6b12979.

17. Buxadera-Palomero, J.; Calvo, C.; Torrent-Camarero, S.; Gil, F.J.; Mas-Moruno, C.; Canal, C.; Rodríguez, D. Biofunctional polyethylene glycol coatings on titanium: An in vitro-based comparison of functionalization methods. *Colloids Surfaces B Biointerfaces* **2017**, *152*, 367–375, doi:10.1016/j.colsurfb.2017.01.042.

18. Cao, S.; Wang, J.; Zhang, Y.; Chen, D. The effectiveness of an antifouling compound coating based on a silicone elastomer and colored phosphor powder against *Navicula* species diatom. *J. Coatings Technol. Res.* **2013**, *10*, 397–406, doi:10.1007/s11998-012-9457-z.

19. Dalsin, J.L.; Hu, B.H.; Lee, B.P.; Messersmith, P.B. Mussel adhesive protein mimetic polymers for the preparation of nonfouling surfaces. *J. Am. Chem. Soc.* **2003**, *125*, 4253–4258, doi:10.1021/ja0284963.

20. Manolakis, I.; Azhar, U. Recent advances in mussel-inspired synthetic polymers as marine antifouling coatings. *Coatings* **2020**, *10*, doi:10.3390/coatings10070653.

21. Eduok, U.; Faye, O.; Szpunar, J. Recent developments and

- applications of protective silicone coatings: A review of PDMS functional materials. *Prog. Org. Coatings* **2017**, *111*, 124–163, doi:10.1016/j.porgcoat.2017.05.012.
22. Camós Noguer, A.; Latipov, R.; Madsen, F.B.; Daugaard, A.E.; Hvilsted, S.; Olsen, S.M.; Kiil, S. Visualization of the distribution of surface-active block copolymers in PDMS-based coatings. *Prog. Org. Coatings* **2018**, *120*, 179–189, doi:10.1016/j.porgcoat.2018.03.011.
23. Selim, M.S.; Elmarakbi, A.; Azzam, A.M.; Shenashen, M.A.; EL-Saeed, A.M.; El-Safty, S.A. Eco-friendly design of superhydrophobic nano-magnetite/silicone composites for marine foul-release paints. *Prog. Org. Coatings* **2018**, *116*, 21–34, doi:10.1016/j.porgcoat.2017.12.008.
24. Guo, H.; Yang, J.; Zhao, W.; Xu, T.; Lin, C.; Zhang, J.; Zhang, L. Direct formation of amphiphilic crosslinked networks based on PVP as a marine anti-biofouling coating. *Chem. Eng. J.* **2019**, *374*, 1353–1363, doi:10.1016/j.cej.2019.06.025.
25. Patterson, A.L.; Wenning, B.; Rizis, G.; Calabrese, D.R.; Finlay, J.A.; Franco, S.C.; Zuckermann, R.N.; Clare, A.S.; Kramer, E.J.; Ober, C.K.; et al. Role of Backbone Chemistry and Monomer Sequence in Amphiphilic Oligopeptide- and Oligopeptoid-Functionalized PDMS- and PEO-Based Block Copolymers for Marine Antifouling and Fouling Release Coatings. *Macromolecules* **2017**, *50*, 2656–2667, doi:10.1021/acs.macromol.6b02505.
26. Qin, X.; Li, Y.; Zhou, F.; Ren, L.; Zhao, Y.; Yuan, X. Polydimethylsiloxane-polymethacrylate block copolymers tethering quaternary ammonium salt groups for antimicrobial coating. *Appl. Surf. Sci.* **2015**, *328*, 183–192, doi:10.1016/j.apsusc.2014.12.019.

27. Liu, Y.; Leng, C.; Chisholm, B.; Stafslie, S.; Majumdar, P.; Chen, Z. Surface structures of PDMS incorporated with quaternary ammonium salts designed for antibiofouling and fouling release applications. *Langmuir* **2013**, *29*, 2897–2905, doi:10.1021/la304571u.
28. Bodkhe, R.B.; Thompson, S.E.M.; Yehle, C.; Cilz, N.; Daniels, J.; Stafslie, S.J.; Callow, M.E.; Callow, J.A.; Webster, D.C. The effect of formulation variables on fouling-release performance of stratified siloxane-polyurethane coatings. *J. Coatings Technol. Res.* **2012**, *9*, 235–249, doi:10.1007/s11998-011-9362-x.
29. Webster, D.C.; Chisholm, B.J.; Stafslie, S.J. Mini-review: Combinatorial approaches for the design of novel coating systems. *Biofouling* **2007**, *23*, 179–192, doi:10.1080/08927010701250948.
30. Ekin, A.; Webster, D.C.; Daniels, J.W.; Stafslie, S.J.; Cassé, F.; Callow, J.A.; Callow, M.E. Synthesis, formulation, and characterization of siloxane-polyurethane coatings for underwater marine applications using combinatorial high-throughput experimentation. *J. Coatings Technol. Res.* **2007**, *4*, 435–451, doi:10.1007/s11998-007-9039-7.
31. Majumdar, P.; Webster, D.C. Preparation of siloxane-urethane coatings having spontaneously formed stable biphasic microtopographical surfaces. *Macromolecules* **2005**, *38*, 5857–5859, doi:10.1021/ma050967t.
32. Majumdar, P.; Stafslie, S.; Daniels, J.; Webster, D.C. High throughput combinatorial characterization of thermosetting siloxane-urethane coatings having spontaneously formed microtopographical surfaces. *J. Coatings Technol. Res.* **2007**, *4*, 131–138, doi:10.1007/s11998-007-9015-2.
33. Pieper, R.J.; Ekin, A.; Webster, D.C.; Cassé, F.; Callow, J.A.; Callow,

- M.E. Combinatorial approach to study the effect of acrylic polyol composition on the properties of crosslinked siloxane-polyurethane fouling-release coatings. *J. Coatings Technol. Res.* **2007**, *4*, 453–461, doi:10.1007/s11998-007-9032-1.
34. Chisholm, B.J.; Staflien, S.J.; Christianson, D.A.; Gallagher-Lein, C.; Daniels, J.W.; Rafferty, C.; Wal, L. Vander; Webster, D.C. Combinatorial materials research applied to the development of new surface coatings. VIII: Overview of the high-throughput measurement systems developed for a marine coating workflow. *Appl. Surf. Sci.* **2007**, *254*, 692–698, doi:10.1016/j.apsusc.2007.05.090.
35. Imbesi, P.M.; Finlay, J.A.; Aldred, N.; Eller, M.J.; Felder, S.E.; Pollack, K.A.; Lonneck, A.T.; Raymond, J.E.; MacKay, M.E.; Schweikert, E.A.; et al. Targeted surface nanocomplexity: Two-dimensional control over the composition, physical properties and anti-biofouling performance of hyperbranched fluoropolymer-poly(ethylene glycol) amphiphilic crosslinked networks. *Polym. Chem.* **2012**, *3*, 3121–3131, doi:10.1039/c2py20317k.
36. Pollack, K.A.; Imbesi, P.M.; Raymond, J.E.; Wooley, K.L. Hyperbranched fluoropolymer-polydimethylsiloxane-poly(ethylene glycol) cross-linked terpolymer networks designed for marine and biomedical applications: Heterogeneous nontoxic antibiofouling surfaces. *ACS Appl. Mater. Interfaces* **2014**, *6*, 19265–19274, doi:10.1021/am505296n.
37. Hu, Z.; Finlay, J.A.; Chen, L.; Betts, D.E.; Hillmyer, M.A.; Callow, M.E.; Callow, J.A.; Desimone, J.M. Photochemically cross-linked perfluoropolyether-based elastomers: Synthesis, physical characterization,

and biofouling evaluation. *Macromolecules* **2009**, *42*, 6999–7007, doi:10.1021/ma901227k.

38. Yarbrough, J.C.; Rolland, J.P.; DeSimone, J.M.; Callow, M.E.; Finlay, J.A.; Callow, J.A. Contact angle analysis, surface dynamics, and biofouling characteristics of cross-linkable, random perfluoropolyether-based graft terpolymers. *Macromolecules* **2006**, *39*, 2521–2528, doi:10.1021/ma0524777.

39. Tang, Y.; Finlay, J.A.; Kowalke, G.L.; Meyer, A.E.; Bright, F. V.; Callow, M.E.; Callow, J.A.; Wendt, D.E.; Detty, M.R. Hybrid xerogel films as novel coatings for antifouling and fouling release. *Biofouling* **2005**, *21*, 59–71, doi:10.1080/08927010500070935.

40. McMaster, D.M.; Bennett, S.M.; Tang, Y.; Finlay, J.A.; Kowalke, G.L.; Nedved, B.; Bright, F. V.; Callow, M.E.; Callow, J.A.; Wendt, D.E.; et al. Antifouling character of “active” hybrid xerogel coatings with sequestered catalysts for the activation of hydrogen peroxide. *Biofouling* **2009**, *25*, 21–33, doi:10.1080/08927010802431298.

41. Saravanan, P.; Jayamoorthy, K.; Ananda Kumar, S. Design and characterization of non-toxic nano-hybrid coatings for corrosion and fouling resistance. *J. Sci. Adv. Mater. Devices* **2016**, *1*, 367–378, doi:10.1016/j.jsamd.2016.07.001.

5. RESULTS AND DISCUSSION

In this chapter, I will discuss the main results obtained during my PhD course.

The results of these studies that will be discussed in the next paragraphs, led to the following publications on international journals

- ❖ Iannazzo, D.; Pistone, A.; Celesti, C.; Triolo, C.; Patané, S.; Giofré, S.V.; Romeo, R.; Ziccarelli, I.; Mancuso, R.; Gabriele, B.; Visalli, G.; Facciola, A.; Di Pietro, A. A Smart Nanovector for Cancer Targeted Drug Delivery Based on Graphene Quantum Dots. *Nanomaterials* **2019**, *9*, 282. <https://doi.org/10.3390/nano9020282>
- ❖ Pistone, A.; Iannazzo, D.; Celesti, C.; Piperopoulos, E.; Ashok, D.; Cembran, A.; Tricoli, A.; Nisbet, D. Engineering of Chitosan-Hydroxyapatite-Magnetite Hierarchical Scaffolds for Guided Bone Growth. *Materials* **2019**, *12*, 2321. <https://doi.org/10.3390/ma12142321>
- ❖ Legnani, L., Iannazzo, D., Pistone, A., Celesti, C., Giofrè, S., Romeo, R., Di Pietro, A., Visalli, G., Fresta, M., Bottino, P., Blanco, I., Chiacchio, M. A. Functionalized polyhedral oligosilsesquioxane (POSS) based composites for bone tissue engineering: synthesis, computational and biological studies. *RSC Advances* **2020**, *10*(19), 11325–11334. [doi:10.1039/d0ra01636e](https://doi.org/10.1039/d0ra01636e)
- ❖ Pistone, A.; Iannazzo, D.; Celesti, C.; Scolaro, C.; Giofré, S.V.; Romeo, R.; Visco, A. Chitosan/PAMAM/Hydroxyapatite Engineered Drug Release Hydrogels with Tunable Rheological Properties. *Polymers* **2020**, *12*, 754. <https://doi.org/10.3390/polym12040754>

- ❖ Giofrè, S.V.; Tiecco, M.; **Celesti, C.**; Patanè, S.; Triolo, C.; Gulino, A.; Spitaleri, L.; Scalese, S.; Scuderi, M.; Iannazzo, D. Eco-Friendly 1,3-Dipolar Cycloaddition Reactions on Graphene Quantum Dots in Natural Deep Eutectic Solvent. *Nanomaterials* **2020**, *10*, 2549. <https://doi.org/10.3390/nano10122549>

The chapter will be divided according to the three previously reported research topics. Specifically, it will concern: 1) the synthesis and characterization of GQDs as smart nanocarriers for drug delivery, 2) chitosan functionalized with different compounds for tissue engineering, and 3) 3-aminopropyltriethoxysilane (APTES) used for the design of potential protective coatings against biofouling.

5.1 Synthesis and characterization of an smart nanovector for cancer-targeted drug delivery based on Graphene Quantum Dots

GQDs are nanomaterials that have shown promising applications in biomedical field and in particular in anticancer therapy. The aim of this study was to develop a traceable and biocompatible drug delivery system (DDS) based on GQDs, and bearing an anticancer agent with benzofuran structure and the targeting ligand riboflavin (vitamin B2) (Figure 1). The GQDs used in this study were produced by acidic exfoliation of multi-walled carbon nanotubes (MWCNTs), where the presence of multiple defects in the graphene layers allows the production of graphene fragments containing many oxygen reactive functional groups and endowed with water dispersibility. The anticancer drug chosen for this study, the methyl 3,3-dimethyl-2-(3-methyl-2,3-dihydrobenzofuran-2-yl)butanoate (BFG), belongs to a series of benzofuran-2-acetic ester derivatives. BFG is able to inhibit cell growth and to induce apoptosis in breast cancer cells by increasing the expression of p21^{Cip/WAF1} gene independently of p53. The drug was covalently conjugated to the surface of GQD through a cleavable PEG linker that can be activated inside cells. Modification with PEG is generally considered the favoured method for improving biocompatibility and for masking nanoparticles from immune recognition. The targeting ligand chosen in this study, riboflavin (RF), is an important coenzyme in energy metabolism. The presence of RF receptors over-expressed in human prostate and breast cancer cells have shown to enhance tumor cell uptake of RF and RF conjugates via receptor-mediated endocytosis. In this work, RF was conjugated to the surface of GQDs by exploiting the stable π - π interaction of this nanomaterial

with pyrene derivatives. In addition to its targeting ability, this vitamin is of particular interest for the design of an ideal DDS due to its water solubility, biocompatibility, and intrinsic fluorescence that allows its *in vitro* traceability. The results of *in vitro* biological assays performed on GQDs-based systems, demonstrated the high biocompatibility of the synthesized nanocarrier and the good ability of the developed DDS to increase drug-cell interactions, causing cytotoxicity in all the investigated cell lines (Details are included in the experimental section E.S.1).

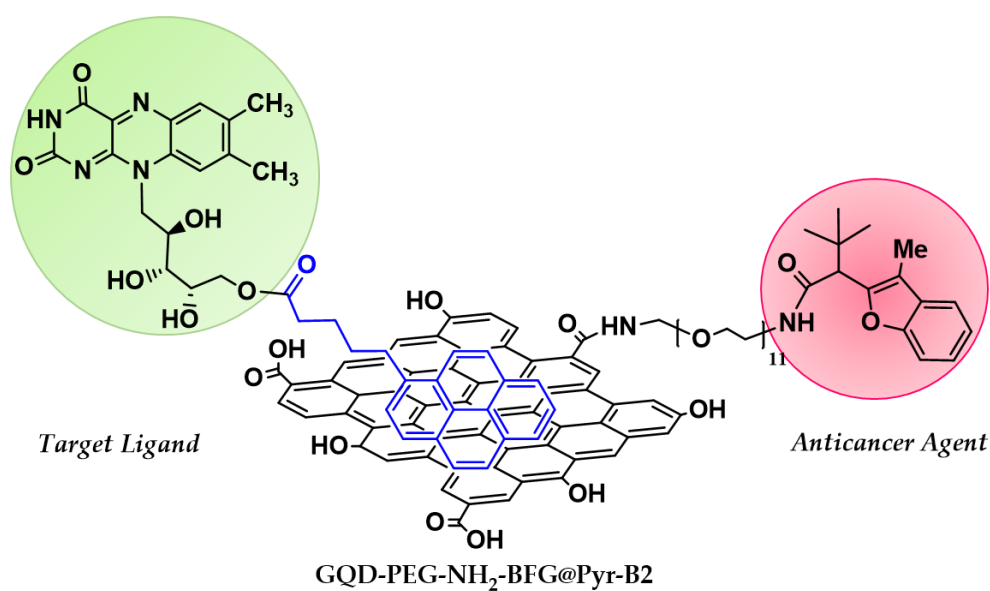


Figure 1. Cancer targeted drug delivery system (DDS) based on graphene quantum dots (GQD).

5.1.1 Characterizations

The synthesized GQD were investigated by XRD, DLS, UV, PL, Raman, and HRTEM analyses. (Fig. 2)

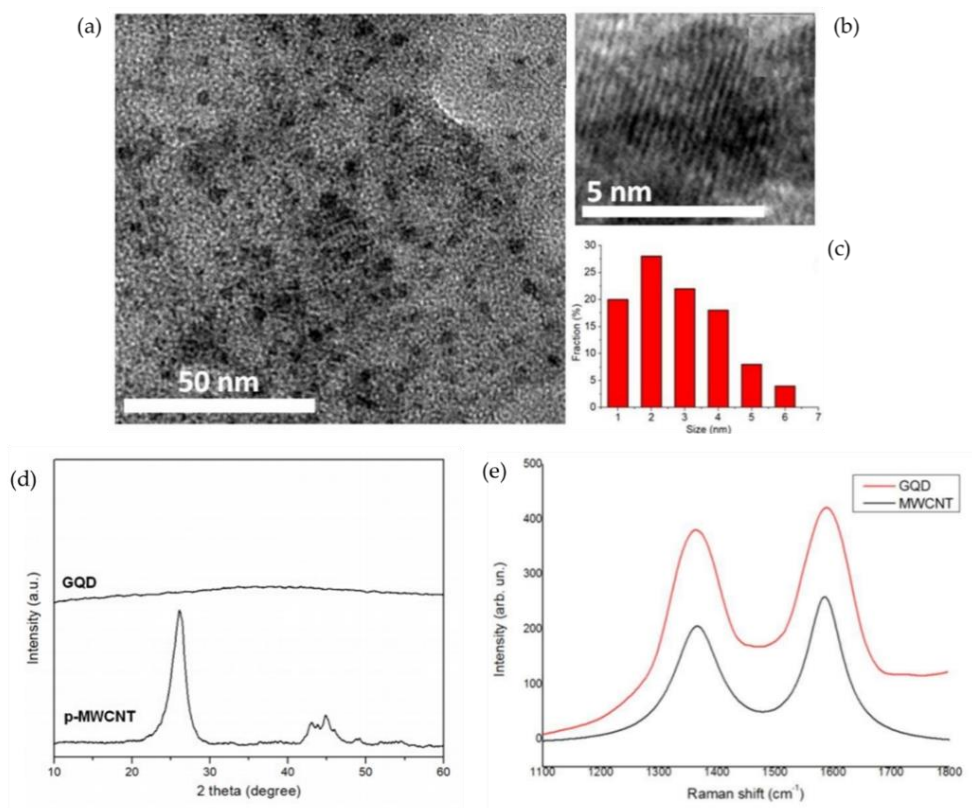


Figure 2. (a) Representative TEM image of the as-prepared GQDs; (b) high-resolution TEM image showing the crystal structure of an individual GQDs; (c) size distribution of GQDs derived from TEM images; (d) XRD spectra of GQDs and of pristine MWCNTs (p-MWCNTs); (e) Raman spectra of GQDs and MWCNTs.

Representative TEM images of the synthesized GQDs show monodisperse particles with a size distribution between 1 and 6 nm (Figure 2a) and a weighted size distribution centered at 2.78 nm, as assessed using statistical calculations performed on more than 200 points (Figure 2c). The HRTEM image shows the graphene crystal structure of single GQDs (Figure 2b). The presence of this structure, which opens up the possibility of modifying the

organic surface with biologically active agents, along with their uniformly small size, make these nanomaterials ideal nanoplatforms for drug delivery applications. The XRD spectrum of the GQDs sample, compared with that of the MWCNTs precursor, shows no diffraction signal throughout the 2-theta range, while MWCNTs shows the presence of the (002) peak. This peak, which is generally considered a measure of the interplanar spacing for two neighboring graphene layers, is totally absent in the GQDs sample and suggests a single-layer structure after acid exfoliation (Figure 2d). In Figure 2e, the Raman spectra of GQDs and MWCNTs are shown. Both spectra show the D band (approximately 1360 cm^{-1}) and the G band (approximately 1590 cm^{-1}), which represent the Raman fingerprint of the carbon nanostructures. The D band is attributed to disorder in sp^2 hybridized carbon, the G band is associated with first-order scattering of the E_{2g} stretching vibration mode observed for sp^2 carbon. The relative intensity ratio of the D and G bands (ID/IG ratio) showed a value of 1.033 for the pristine MWCNT and a value of 1.145 for the GQDs sample, thus further demonstrating the loss of long-range order after acid treatment.

The success of the reaction between GQDs and PEG linker and the subsequent drug loading on the surface of GQDs was investigated by TGA and by FTIR spectroscopy.

The FTIR spectrum of GQDs (Figure 3a) shows two peaks at 1620 cm^{-1} and 3450 cm^{-1} that are related to the vibrations of C=O and O-H bonds, respectively. The additional peak at 1072 cm^{-1} is attributable to the C-O alkoxy group. These data further confirm the presence of many oxygen-containing groups on the GQDs surface. The FTIR spectrum of the PEG-

functionalized sample (GQD-PEG) shows the additional representative peak at 1640 cm^{-1} . The peaks at 1650 and 2870 cm^{-1} that are present in the FTIR spectrum of the PEG-NH₂ sample are considerably weaker in the GQD-PEG conjugated sample, thus demonstrating the amide bond formation between the free amine group of PEG-NH₂ and the carboxyl groups of GQDs. The FTIR spectrum of the drug-conjugated sample (GQD-PEG-BFG) shows the presence of an additional peak at 1680 cm^{-1} , which can be ascribed to the C=O stretching of the amide bond formed after conjugation of BFG to the PEG-functionalized GQD. The FTIR spectrum of the anticancer agent BFG shows the presence of a peak at 2920 cm^{-1} attributable to the stretching of the C-H bond of the aliphatic chain of BFG and a peak at 1750 cm^{-1} due to the stretching of the C=O bond of the ester functionality. The disappearance of the latter peak demonstrates the effectiveness of the conjugation reaction between the drug and the free amine groups present in the nanosystem.

The TGA curves of the functionalized GQDs and pristine GQDs, performed in an inert atmosphere, show weight losses (calculated at $600\text{ }^{\circ}\text{C}$) for both functionalized samples equal to 23.6% for the GQD-PEG and to 29.5% for the GQD-PEG-BFG sample versus 5.6% for the pristine GQD, and are related to the higher amount of organic fraction present on the surface of the GQDs (Figure 3b). The different profiles of the TGA curves of the conjugated compounds further confirm the profound chemical changes that occurred on the nanostructures after the functionalization processes.

The drug loading on the surface of GQDs was measured as the difference between the amount of BFG added in the coupling reaction mixture and the

amount of drug recovered in the solutions filtered from the dialysis bag and was found to be 21.6% by weight.

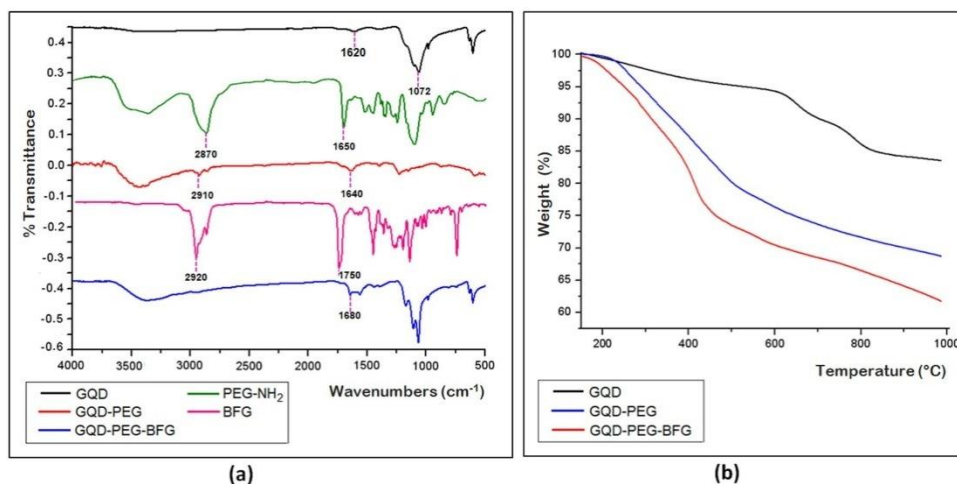


Figure 3. (a) FTIR spectra of GQD, GQD-PEG, GQD-PEG-BFG, PEG-NH₂, and BFG; (b) TGA analysis for GQD, GQD-PEG, and GQD-PEG-BFG conducted in an argon atmosphere.

The presence of a stable interaction between the Pyr-RF targeting module and the GQDs surface was also demonstrated by evaluating the fluorescence properties of GQD@Pyr-RF and GQD-PEG-BFG@Pyr-RF and comparing their PL spectra with those of GQDs and the unbound Pyr-RF samples at an excitation wavelength of 360 nm (Figure 4). The PL spectra of the Pyr-RF-conjugated GQD samples reveal a decrease in fluorescence intensity along with a shift toward red from 566 (in the GQD sample) to 551 and 553 nm in the GQD@Pyr-RF and GQD-PEG-BF@Pyr-RF, respectively, which are indicative of the stable chemical interaction between the targeting module (Pyr-RF) and the surface of GQDs.

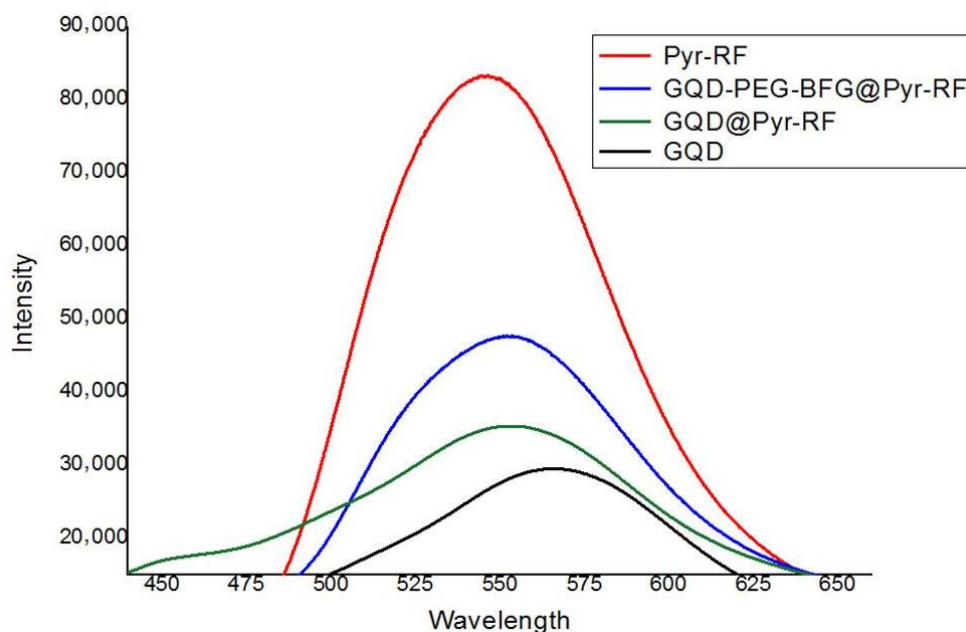


Figure 4. PL spectra of GQD (black line), GQD @ Pyr-RF (green line), GQD-PEG-BFG@ Pyr-RF (blue line) and Pyr-RF (red line) in water, at excitation wavelength of 360 nm. Samples were tested at a concentration of 100 ng/mL

It was also investigated, the effect of the surface functionalization on the size and water dispersibility of GQD-PEG-BFG and GQD-PEG-BFG @ Pyr-RF drug conjugated samples, which may profoundly affect their interaction with cells. The DLS results of the size distribution, for both samples, show two populations smaller than 100 nm (Figures 5 a, c). The GQD-PEG-BFG sample shows two populations centered at 12.6 nm (51%) and 38.5 nm (49%) while for GQD-PEG-BFG@Pyr-RF, two populations centered at 14.9 (52%) and 73.1 nm (52%). Water dispersibility was assessed by calculating electrophoretic mobility in PBS at physiological pH of 7.4. DLS analyses of the GQD-PEG-BFG and GQD-PEG-BFG@Pyr-RF samples show zeta potential values of -32.89 and -31.27 mV, respectively (Figure 6 b,d). The

obtained values, always lower than -30, further confirm the high stability in aqueous solution of the drug-conjugated systems.

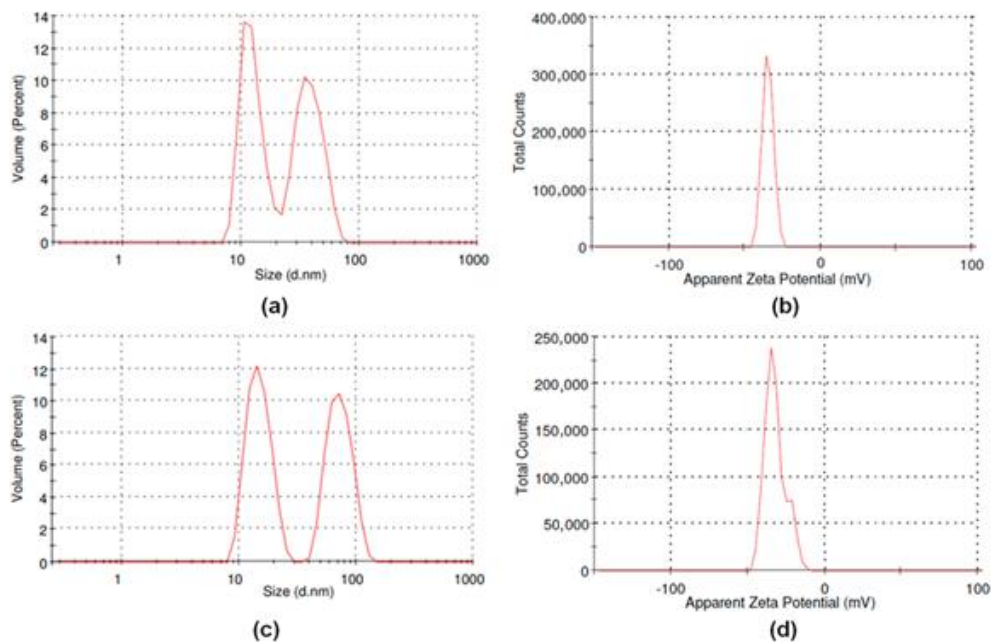


Figure 5. (a) Volume-based size distribution of GQD-PEG-BFG sample; (b) zeta potential measurement of GQD-PEG-BFG sample; (c) volume-weighted size distribution of GQD-PEG-BFG sample @ Pyr-RF; (d) zeta potential measurement of GQD-PEG-BFG sample @ Pyr-RF. All experiments were performed in PBS solutions at pH 7.4.

The cytotoxic effect of synthesized GQD-based nanosystems was tested on three different cancer cell lines: the laryngeal cancer cell line (HEp-2), the human lung epithelial cancer cell line (A549), and the human colorectal adenocarcinoma cell line (HT-29). (Fig. 6) The cytotoxicity of the drug delivery system coupled with the RF targeting molecule and conjugated with the anticancer agent BFG, was compared with that exerted by the same system lacking of the RF ligand (GQD-PEG-BFG) or without the anticancer drug (GQD@Pyr-RF) and with the reference compounds GQD, GQD-PEG, and BFG. Cells, maintained in the same biological medium and incubated

with PBS or BFG solutions, were used as negative and positive controls, respectively. In order to compare the drug of the same concentrations for all tested samples, the BFG solutions used for the biological tests were prepared at the same concentration of the drug present in the GQDs-based samples, as assessed by TGA analysis (range 2.1-42 mg/mL). The results of the biological assays emphasize the low cytotoxicity of the GQD sample as the percentage of dead cells compared to untreated control cells at the highest dosages tested was 29% for HEp-2, 11% for A549, and 17% for HT-29. In all cell lines tested, the IC₅₀ of the nanosystems lacking the anticancer drug, of the GQD-PEG and GQD@Pyr-RF samples, was approximately halved compared with GQD. Most likely, these higher cytotoxicities ($P < 0.01$) were due to the better interactions between the cell membranes and the chemical counterparts present in the PEG and RF moieties, thus emphasizing the more pronounced bioavailability of the tested nanosystems. The drug delivery system, GQD-PEG-BFG@Pyr-RF, exhibited cytotoxic activity against the three cancer cell lines studied, with significantly higher potency in alveolar cancer cells than BFG alone (IC₅₀ = 114.5 vs 153.7; $P < 0.05$). Cytotoxicity assays showed that despite the low water solubility of BFG alone, the drug-conjugated nanosystem exhibited greater dispersibility in water and better cell-drug interactions, thus opening up new possibilities in the use of this or other poorly water-soluble anticancer drugs endowed with critical cytotoxicity and side effects.

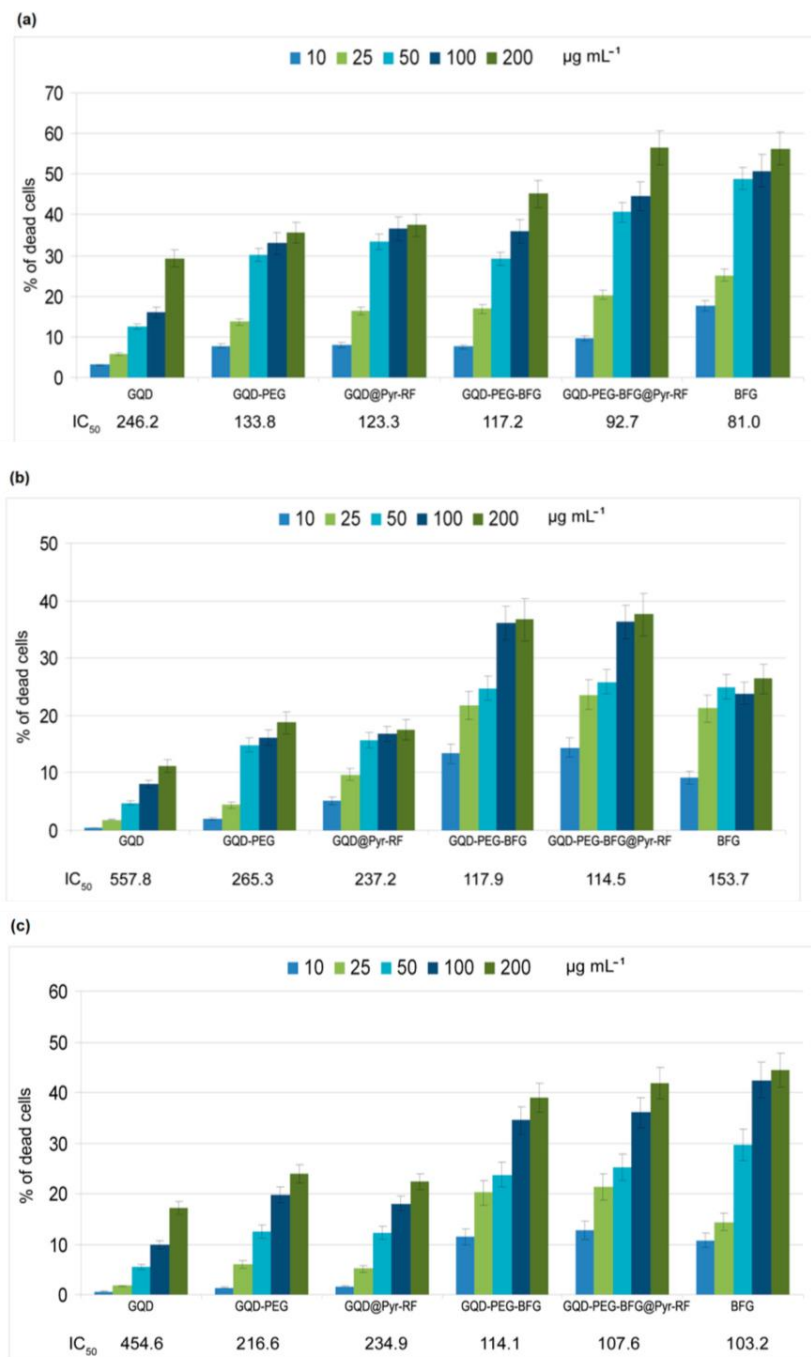


Figure 6. Cytotoxic effect of the synthesized drug delivery nanosystems in (a) laryngeal cancer cells HEp-2, (b) human lung epithelial cancer cell line A549, and (c) the human colorectal adenocarcinoma cell line HT-29.

5.2 Synthesis and characterization of Eco-Friendly 1,3-Dipolar Cycloaddition Reactions on Graphene Quantum Dots in Natural Deep Eutectic Solvent

The possibility offered by the organic multi-functionalization of graphene-structured nanomaterials was exploited to perform the microwave-assisted 1,3 dipolar cycloaddition (1,3-DCA) reaction of two nitrons: the newly synthesized C-ethoxycarbonyl, N-methyl nitrone 1a and C-diethoxyphosphorylpropylidene, N-benzyl nitrone 1b, with the graphene surface of GQDs, leading to the formation of the *isox*-GQD 2a and 2b (Fig. 7). The cycloaddition reactions were carried out using a natural deep eutectic solvent (NADES) consisting of the zwitterionic trimethylglycine (TMG) as the hydrogen bond donor (HBD) and glycolic acid (GA) of the hydrogen bond acceptor (HBA). This NADES, with both components derived from sugar beet, contains no chloride or metal ions in its composition, is economical, and exhibits advantageous physical properties, such as low viscosity and low melting point. (Details are included in the experimental section E.S.1)

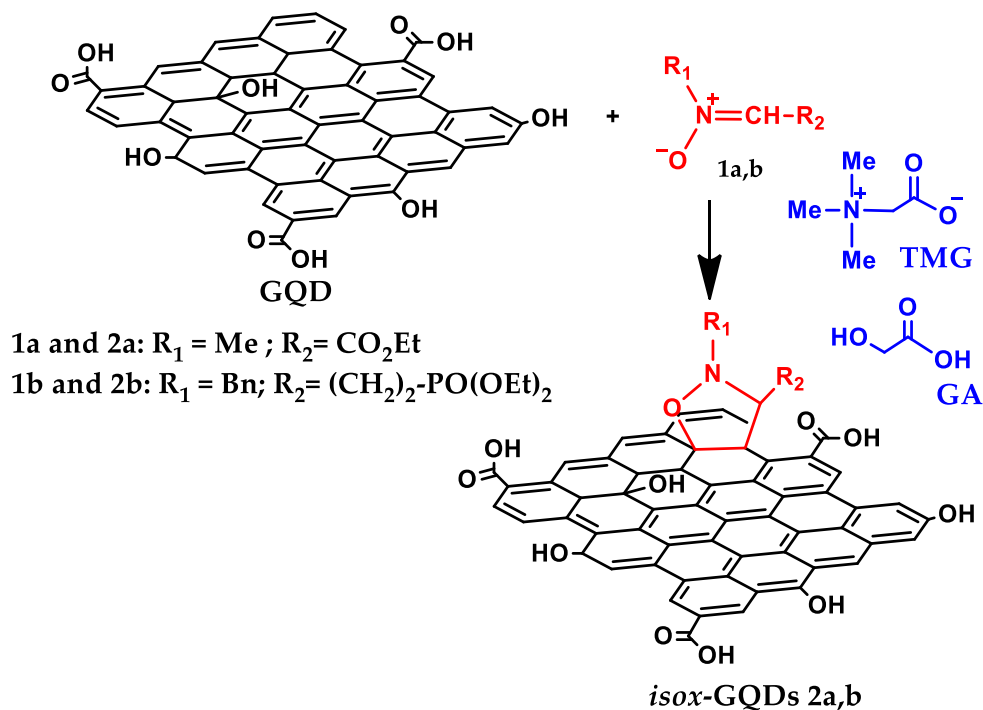


Figure 7. Synthesis of isox-GQDs 2a, b reactions of 1,3-DCA with nitrons 1a,b in NADES medium.

5.2.1 Characterizations

The GQDs used for this study were synthesized using a top-down procedure previously reported in Section 5.1, starting from multi-walled carbon nanotubes (MWCNTs) in order to obtain nanodots with many oxygen-containing functional groups and were characterized by Raman, high-resolution transmission electron microscopy (HRTEM), dynamic light scattering (DLS), UV-VIS, and photoluminescence (PL) analysis. The Raman spectra (Fig. 8a) show the D-band (ca. 1320 cm^{-1}) and G-band (ca. 1590 cm^{-1}), which are usually present in carbon nanostructures. Their relative intensity ratio (ID/IG ratio) showed values of 1.03 for the starting MWCNTs and 1.68 for the GQDs, thus demonstrating the loss of long-range order after the top-

down procedure. Representative TEM imaging of GQDs shows monodisperse nanoparticles with a weighted size distribution centered at 4.8 nm; furthermore, the HRTEM image reported in the inset, further confirms the lattice fringes (~ 0.21 nm) of GQDs (Figure 8b). DLS measurements showed a maximum of the volume weighted percent at 5.85 nm, further demonstrating the small size of the synthesized nanomaterials (Figure 8c). Figure 8d shows the UV-vis absorption and photoluminescence excitation of the synthesized nanomaterials. The UV spectrum shows the typical π - π transition absorption peak at about 250 nm, due to the π - π^* transition of the sp^2 aromatic domains, while the PL measurements confirm the emission properties of GQDs since at the excitation wavelength of 360 nm, the nanomaterial water dispersion showed a strong peak at 560 nm.

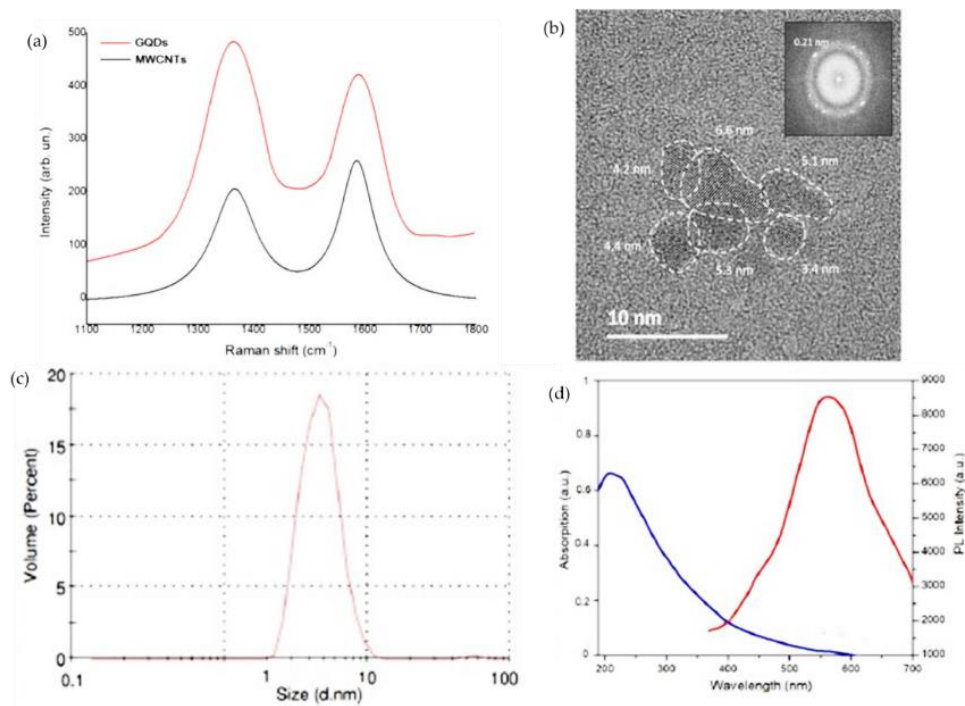


Figure 8. (a) Raman spectra ($\lambda_{exc} = 532$ nm) of pristine MWCNTs and of the synthesized GQDs; (b) Representative HRTEM image of a GQDs cluster with mean particle size of 4.8 nm and the corresponding fast Fourier transform (FTT) on the inset showing planes at 0.21 nm; (c) DLS measurement of GQDs dispersion in deionized water; (d) optical properties of GQDs dispersions in deionized water: UV–vis absorption spectrum of GQDs (blue line) and photoluminescence (PL) spectrum of GQDs at the excitation wavelengths of 360 nm (red line).

The formation of the cycloadducts *isox*-GQDs 2a and *isox*-GQDs 2b was investigated by Fourier transform infrared spectroscopy (FTIR) and by thermogravimetric analysis (TGA), while the chemical and physical properties of the synthesized nanomaterials were evaluated by Raman spectroscopy, DLS and PL analysis. The TGA curves of the GQDs and the corresponding cycloadducts, performed in an inert atmosphere, show, for both cycloadducts, an increase in weight losses, whose amounts, calculated at 500 °C, were found to be 8.4 and 4.9 wt% for *isox*-GQDs 2a and *isox*-GQDs 2b, respectively (Figure 9a). Furthermore, the different TGA curve profiles of the cyclic products confirm that profound chemical changes occurred on the nanomaterials after the chemical functionalization. The degree of functionalization was also confirmed calculating the difference between the initial amount of nitrene used to functionalize the GQDs and the amount of unbound dipole present in the wash water solutions after dialysis. The calculated percentages of 8.3 and 5.0 wt % for *isox*-GQDs 2a and *isox*-GQDs 2b, respectively, are in agreement with the results obtained from TGA analysis. The FTIR spectrum of the GQDs shows the presence of a large band around 3450 cm⁻¹, related to the stretching of the O–H bonds, the stretching of the C=O group at 1610 cm⁻¹, and the stretching of the O–H group at 1420 cm⁻¹. These peaks indicate the presence of many oxygen-containing groups on the surface of the GQDs. The FTIR spectra of the cyclic products show additional representative peaks at 850 cm⁻¹ related to the stretching of the newly formed N-O bond. In addition, the spectrum of *isox*-GQDs 2a shows the presence of a peak at 1727 cm⁻¹, related to the newly introduced ester functionality, while for the phosphonate adduct *isox*-GQDs 2b, the additional

peak is observed at 958 cm^{-1} , attributable to the vibration of the P-O group (Figure 9b). The surface modification of GQDs was also investigated by comparing the PL properties of the starting nanomaterials with those of the corresponding cycloproducts in deionized water at the excitation wavelength of 360 nm (Figure 9c). The PL λ_{max} of GQDs, *isox*-GQDs 2a, and *isox*-GQDs 2b were approximately 560, 545, and 550 nm, respectively. These blue-shifted emissions may demonstrate that the organics are covalently bound with GQDs, as also reported for similar systems.

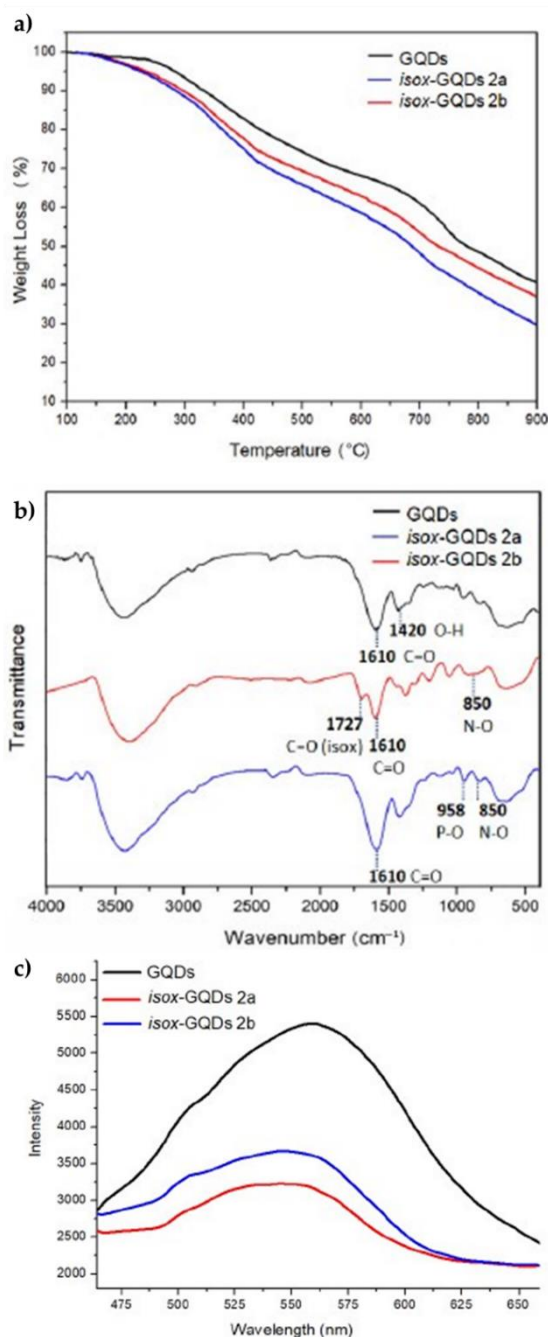


Figure 9. (a) TGA curves of GQDs, isox-GQDs 2a and isox-GQDs 2b, performed in Ar atmosphere; (b) FTIR spectra of GQDs, isox-GQDs 2a and isox-GQDs 2b; (c) PL spectra of GQDs, isox-GQDs 2a and isox-GQDs 2b, at the λ_{exc} of 360 nm. All samples were tested at a concentration of 100 ng/mL.

The effect of surface modification on the size and water dispersibility of the cycloproducts was also investigated, since these properties deeply affect the interaction of the nanomaterials with the biological system (Figure 10). Both *isox*-GQDs 2a and *isox*-GQDs 2b samples show single size populations centered at 6.61 and 4.95 nm, respectively. Dispersibility in water, assessed by measuring their electrophoretic mobility in deionized water, showed zeta potential values below -30 mV (-30.7 mV and -31.2 mV for *isox*-GQDs 2a and *isox*-GQDs 2b, respectively) further confirming their high stability in water.

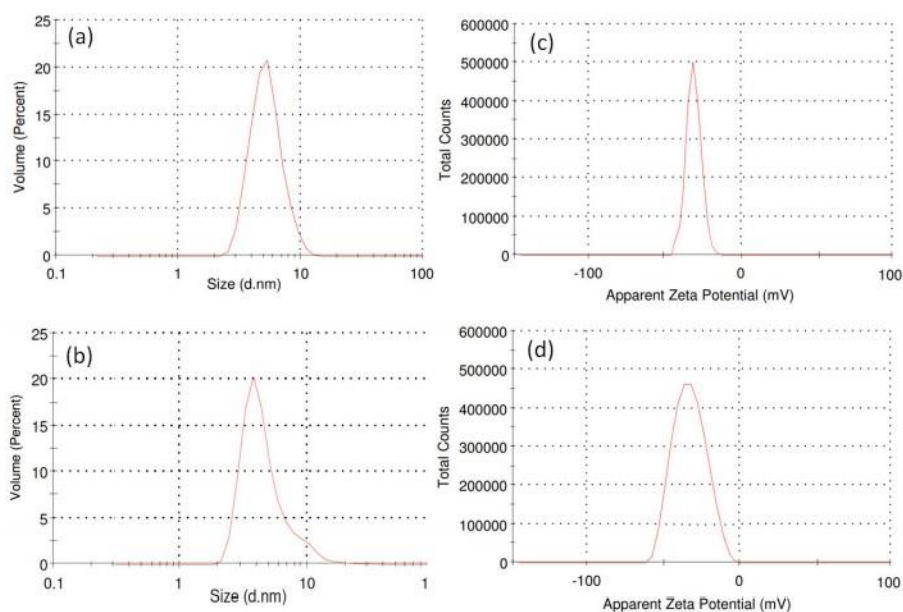


Figure 10. Volume-weighted size distribution of (a) *isox*-GQDs 2a and (c) *isox*-GQDs 2b; zeta potential measurement of (b) *isox*-GQDs 2a and (d) *isox*-GQDs 2b. All the experiments were performed deionized water.

5.3 Synthesis and characterization of Chitosan-Hydroxyapatite-Magnetite Hierarchical Scaffolds

As discussed previously, bioabsorbable polymers have received increasing attention as novel systems for the development of osteoconductive biomaterials for bone tissue engineering. During my PhD studies, chitosan-based composites were synthesized by adding hydroxyapatite into a chitosan matrix using the *in situ* precipitation technique. The effectiveness of the scaffold was further enhanced by the inclusion of crystalline magnetite nanoparticles. These nanoparticles were incorporated to enhance the performance of the scaffolds due to the super magnetic and ferromagnetic properties of iron oxide used in biomedical applications such as MRI, hyperthermia and as drug delivery systems. On this basis, the ability of chitosan/hydroxyapatite/magnetite (CS/HA/MGN) composites cross-linked with genipin as potential biomaterials able to induce osteoinduction and osseointegration has been investigated. These materials were found to be biocompatible with primary osteoblastic cells. In particular, the inclusion of magnetite significantly increases the number of osteoblastic cells infiltrating the scaffold and, more importantly for implant therapy; it increases the number of viable osteoblastic cells at the scaffold interface. (Details are included in the experimental section E.S.2)

5.3.1 Characterizations

The synthesized composites were characterized by optical and electron microscopy and by TGA and XRD analyses. As mentioned above, *in situ* precipitation was shown to ensure a superior homogeneous dispersion of hydroxyapatite within the chitosan matrix compared to what was observed from hydroxyapatite powder, as evidenced in Figure 11 where large clusters of HA, as indicated by the arrows, were observed (Fig.11a), A homogeneous distribution of HA was instead observed in the sample prepared using the *in situ* precipitation method (Fig.11b).

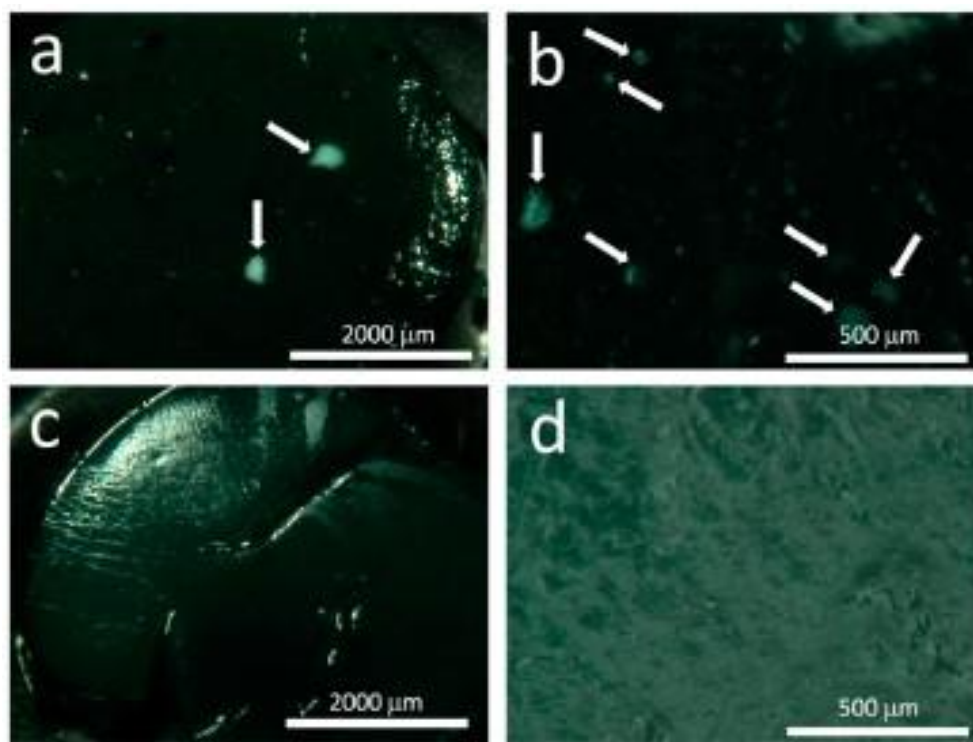


Figure 11. Optical images of chitosan/hydroxyapatite (CS/HA) composites prepared with HA powder (a, lower magnification, and b, higher magnification) and HA obtained by *in situ* precipitation (c, lower magnification, and d, higher magnification) (Images collected with Hirox digital microscope mod. KH8700 with a MX(G)-5040Z lens).

X-ray diffractometry (XRD) analyses, used to determine the crystalline phases contained in the minerals, confirmed the distribution of crystalline hydroxyapatite and magnetite in the biopolymer matrix obtained by precipitation (Fig. 12a); moreover, hydroxyapatite showed low or average values of crystallinity and/or nanosized crystals (20 nm), thus guaranteeing a high metabolic activity. In order to obtain information on the degree of crystallinity within the samples prepared by in situ precipitation, the average crystallite size of hydroxyapatite was calculated from Scherrer's equation using the reflection peak (002) at 2θ 26° , which shows no interference.

$$L = (0.9 \cdot \lambda) / \beta_{002} \cdot \cos \theta \quad (1)$$

where the L value represents the average crystallite size of the hydroxyapatite, β_{002} is the peak width at the peak half maximum (002) expressed in radians, λ is the wavelength of X-ray radiation (Cu K α radiation, $\lambda = 0.15418$ nm), and θ (radians) is the angular position of the peak (002). Conversion of the β_{002} value from degrees to radians is obtained using equation (2):

$$\beta_{002} \text{ (rad)} = \beta_{002} \text{ (2 theta degree)} \cdot \pi / 180 \quad (2)$$

The crystallinity, denoted X_c , which corresponds to the fraction of the crystalline phase of the hydroxyapatite in the powdered sample, was calculated using an empirical relationship between X_c and β_{002} , according to equation (3):

$$X_c = (K / \beta_{002})^3 \quad (3)$$

where X_c is the degree of crystallinity, β_{002} is the full width of the peak at half reflection intensity (002) in degree 2θ , and K is a constant set at 0.24. The data in Table 1 show that chitosan-based systems trapped hydroxyapatite with low to medium values of crystallinity and/or nanometer

crystallites, providing high metabolic activity. This is important, since the bioactivity of hydroxyapatite, in terms of bioabsorption by chemical binding to surrounding hard tissues, is highly dependent on its crystallinity and particle size distribution.

Table 1. Average crystallite size and crystallinity degree of hydroxyapatite in the chitosan-based systems

Sample Code	Full-Width at Half Maximum of (002)Peak (FWHM)	Crystallinity	Average Crystallite Size (L)
	(2θ)	(X_c)	(nm)
CS/HA	0.32	0.421875	25.26
CS/HA/MGN	0.44	0.162284	18.46

On the other hand, thermogravimetric analyses were performed to measure the thermal degradation of the composites; they were performed on the CS, CS/HA, and CS/HA/MGN systems. All samples were pre-treated at 100°C until they reached a constant weight, before being subsequently treated up to 700°C at a rate of 20°C/min under air flow. The hydroxyapatite-containing systems showed improved thermal stability of the chitosan matrix with a residual weight at temperature above 600°C of 33-34 wt % relative to the hydroxyapatite or hydroxyapatite/iron oxide loading in the CS/HA and CS/HA/MGN composites. Furthermore, in the CS/HA/MGN samples, the presence of iron oxides catalyzes the combustion of the chitosan matrix at higher temperatures than in the CS/HA system. Importantly, the TGA results confirmed that the overall chitosan structure was preserved during *in situ* precipitation of hydroxyapatite or hydroxyapatite/iron oxides, as observed

by the similar weight loss profiles of the composites compared to pure chitosan. (Fig. 12b)

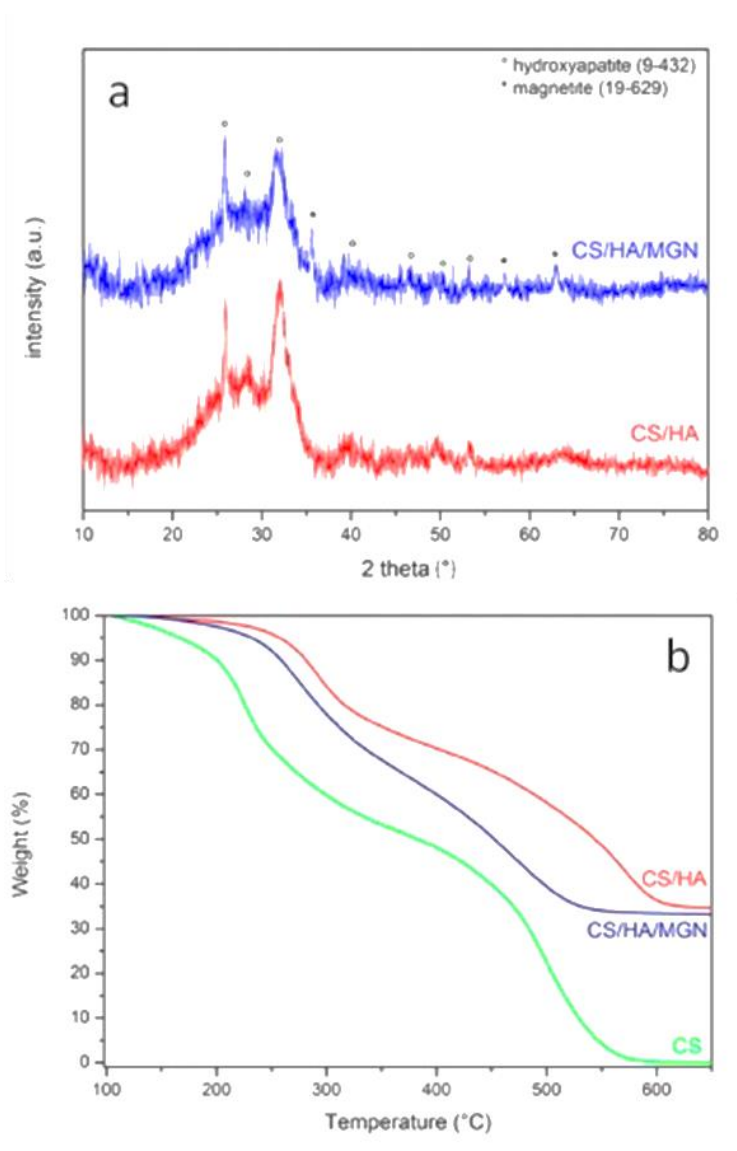


Figure 12. (a) X-ray diffraction (XRD) spectra of CS/HA and CS/HA/MGN (chitosan/hydroxyapatite/magnetite) composites; (b) thermogravimetric analyses (TGA) curves for CS, CS/HA and CS/HA/MGN samples. All experiments were performed under an air atmosphere.

Subsequently, the surface morphology and structure homogeneity of the synthesized composites were studied by field emission scanning electron

microscopy (FEG-SEM). Prior to SEM analysis, the samples were coated with a chromium layer. SEM revealed that the cross-linked chitosan had a smooth surface with a layered structure (Figure 13). The addition of hydroxyapatite and/or hydroxyapatite/iron oxide in the formulation, resulted in the appearance of agglomerates on the surface of the chitosan without any change on the overall, layered structure of the polymer. EDX analysis, shown in Figure 12, confirmed the presence of hydroxyapatite or iron oxides in the composites. In addition, the mapping analysis performed on the CS/HA/MGN composites showed that iron ions (yellow spots) were homogeneously distributed in the composites with an Fe/Ca atomic ratio close to 0.19 (Figure 14). This value, combined with the TGA result showing a residual inorganic mass in the CS/HA/MGN sample of 33% by weight, allows us to determine the composition of CS/HA/MGN as shown in Table 2, since in the punctual EDX elemental analysis on the products each peak corresponds to a unique chemical element with its atomic and weight concentration.

Table 2. Composition of chitosan-based samples as calculated by thermogravimetric analyses (TGA) and Energy Dispersive X-ray (EDX) analyses.

Sample Code	Composition (wt %)		
	Chitosan	Hydroxyapatite	Magnetite
CS	100	//	//
CS/HA	66	34	//
CS/HA/MGN	67	28.8	4.2

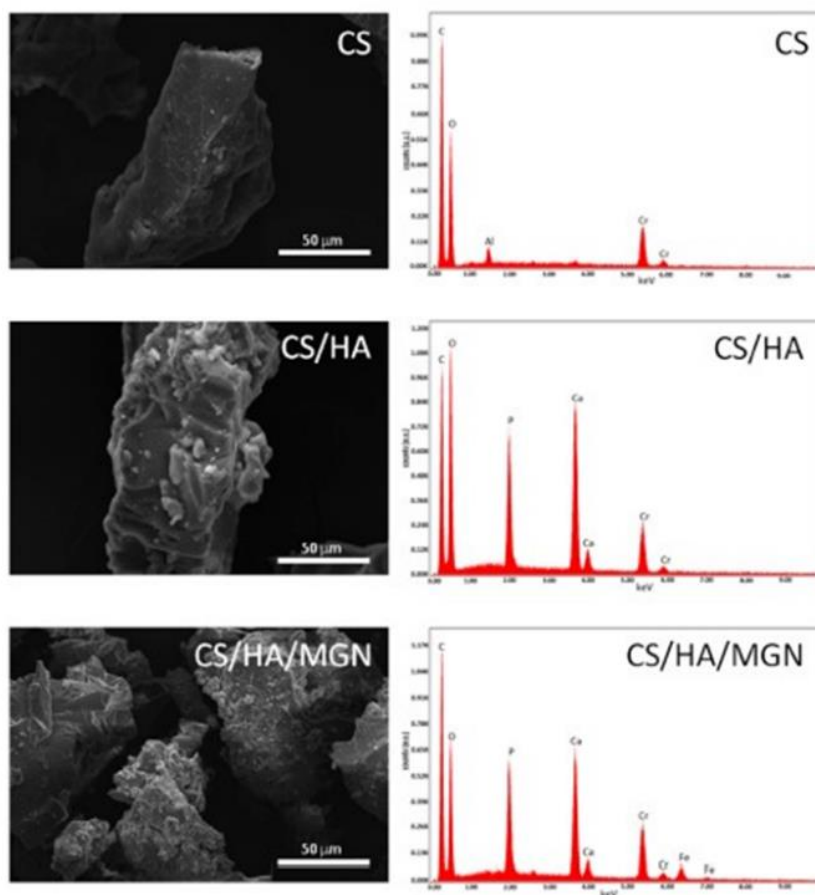


Figure 13. Representative Scanning Electron Microscopy/ Energy Dispersive X-ray (SEM/EDX) analysis of CS, CS/HA, and CS/HA/MGN composites.

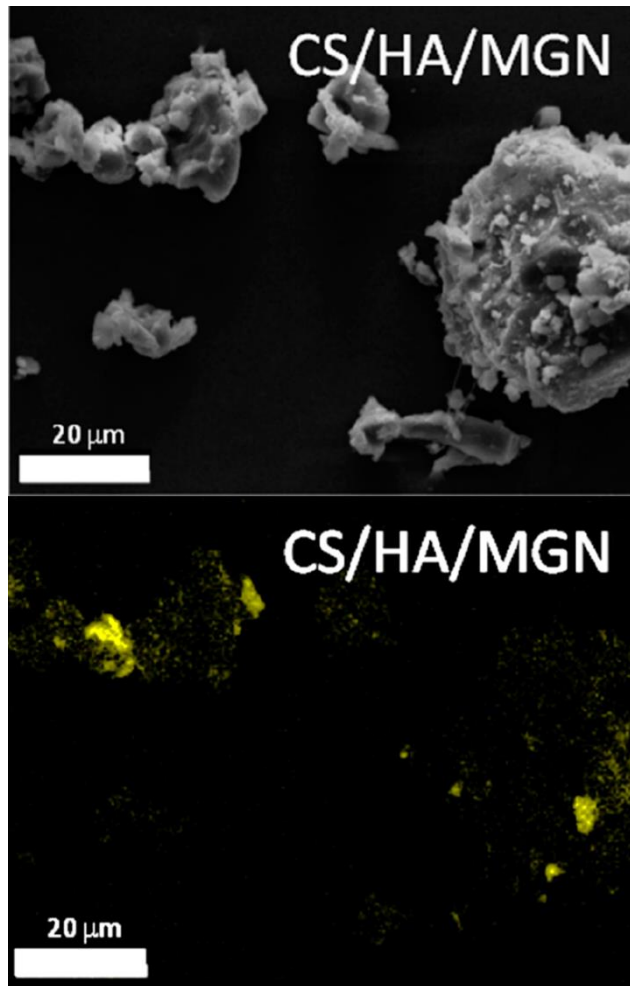


Figure 14. Mapping analysis performed on CS/HA/MGN composite.

The biocompatibility of cells in the immediate microenvironment of scaffolds was assessed to conclude how osteoblasts interact with the tissue-implant interface. Cytotoxicity analysis confirmed the non-toxic nature of the scaffolds over time, with the CS/HA/MGN sample having the highest number of cells due to new magnetite inclusions and the positive influence of its super magnetic and ferromagnetic properties on osteoblast maintenance and differentiation. (Fig. 15) Importantly, the bioactivity of the CS/HA/MGN scaffold has been shown to be higher than that of the CS or

CS/HA scaffolds opening further enhancement of cell proliferation with the application of the external magnetic field.

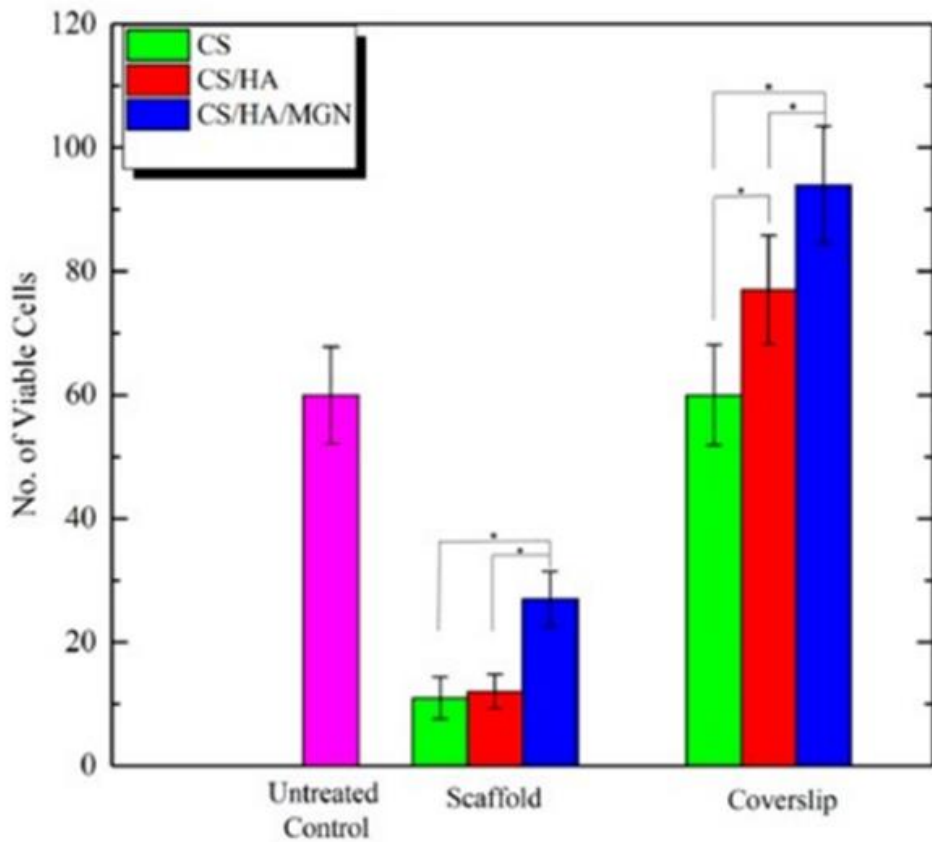


Figure 15. Live cells quantification. Plot showing the average quantified cells on the different scaffolds and test samples.

5.4 Synthesis and characterization of Chitosan/PAMAM/Hydroxyapatite

Subsequently, a novel biodegradable and bioresorbable chitosan-based hydrogel formulation was investigated for controlled drug delivery.

Chitosan was covalently bound with a hyperbranched PAMAM dendrimer followed by *in situ* hydroxyapatite precipitation and gelation. (Fig. 16)

Polyamidoamine dendrimers (PAMAM) represent novel blockers of the pore-mediated translocation of the components of two medically relevant binary bacterial toxins: anthrax toxin from *Bacillus anthracis* and C2 toxin from *Clostridium botulinum* both *in vitro* and *in vivo*. The ability of cationic dendrimers, which carry multiple functional groups, to effectively inhibit the intracellular transport of enzymatic components essential for the aforementioned toxins highlights the value of multivalent interaction in drug development by protecting against intoxication.

Hydrogels were also doped with an anti-inflammatory drug (ketoprofen) to study their drug release properties. Chemical and physicochemical characterizations confirmed the successful covalent functionalization of chitosan with PAMAM and the synthesis of nanostructured hydroxyapatite. The developed hydrogels allowed obtaining innovative systems with rheological properties and drug release properties compared to the well-known formulations containing chitosan and hydroxyapatite powder. The developed chitosan-dendrimer-hydroxyapatite hydrogels can couple the well-known osteoconductive properties of hydroxyapatite with the drug release behavior and good processability of chitosan-dendrimer hydrogels, opening new approaches in the field of tissue engineering based on biopolymer scaffolds. (Details are included in the experimental section ES.2)

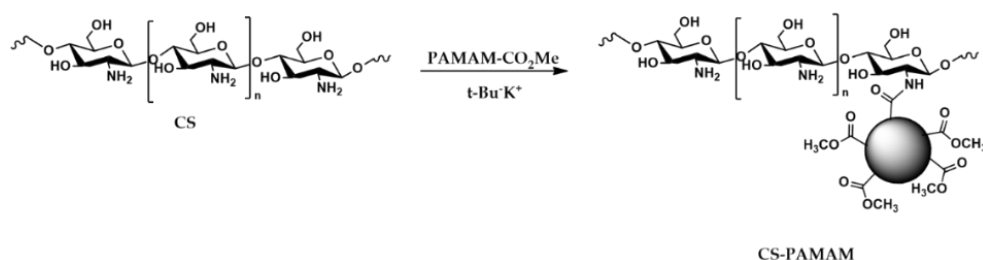
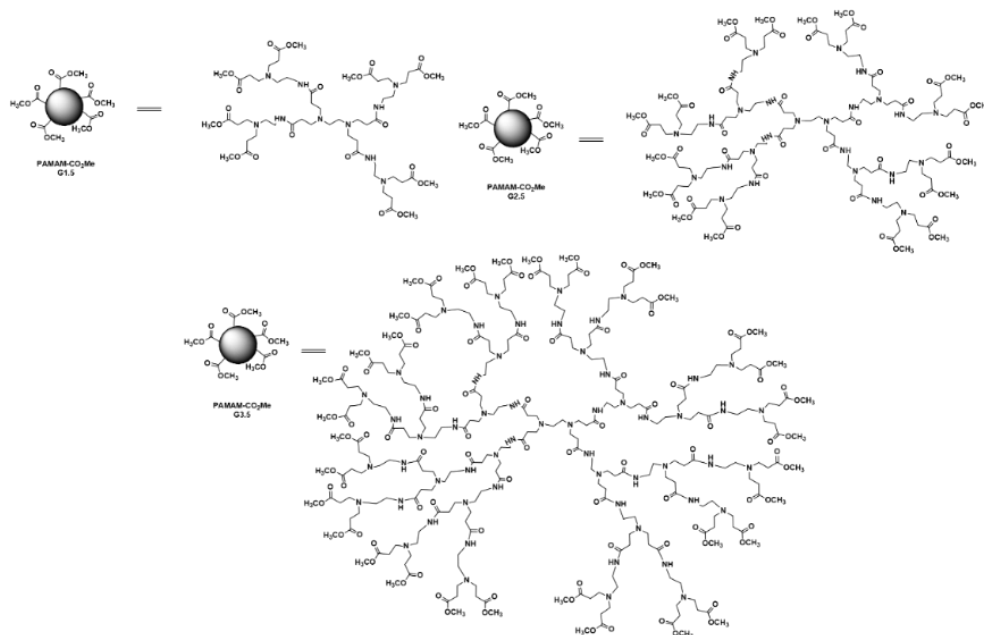


Figure 16. Synthesis of CS-PAMAM chains.

5.4.1 Characterizations

The first step required for the final development of the chitosan-PAMAM-based hydrogels involved the synthesis of the chitosan-PAMAM chains. Generation 1.5, 2.5, and 3.5 PAMAM dendrimers, containing methyl ester moieties on the outer surface, were synthesized according to a procedure consisting of two consecutive steps: (a) Michael's addition of a primary amine group to methyl acrylate (MA) and (b) amidation reaction of the ester moieties to ethylenediamine (EDA). The tetraester obtained in the first process is called the 0.5 generation dendrimer (G0.5). Repetition of these two processes on PAMAM G0.5 resulted in the PAMAM G1.5 dendrimer and, subsequently, the desired dendrimers PAM-CO₂Me G2.5 and PAM-CO₂Me G3.5, whose structure was confirmed by ¹H NMR spectroscopy. NMR analysis of PAM-CO₂Me shows diagnostic signals of the methyl ester societies at 3.66 ppm, and three sets of multiples centered at 3.25, 2.75, and 2.45 ppm, attributable to methylenes protons near the amide groups, methylenes protons from the amine groups, and methylenes groups in position at the ester societies, respectively. The ester group portions present on the outer surface of the PAMAM-CO₂Me dendrimer were used for the *tert*-butoxide-assisted amidation reaction with the free nucleophilic amine

groups of chitosan (Scheme 1). The PAMAM-CO₂Me sample was purified using a dialysis bag capable of retaining compounds with MW of 12,000 or higher, and then amide bond formation between PAMAM dendrimers and chitosan was studied by ¹H NMR and FTIR spectroscopy.



Scheme 1. Chemical structure of PAMAM dendrimers.

The FTIR spectroscopy analyses further confirmed the presence of a covalent bond between chitosan and the PAMAM dendrimers (Fig. 17). The FTIR spectrum of chitosan shows a band at 1580 cm⁻¹ ascribable to N–H bending and a peak at 1029 cm⁻¹ corresponding to C–O stretching; moreover, the presence of residual *N*-acetyl groups on the chitosan structure is confirmed by the presence of a peak at 1650 cm⁻¹ corresponding to the C=O stretching of the primary amide. The PAMAM-CO₂Me sample shows peaks at 1735 cm⁻¹ and 1648 cm⁻¹ corresponding to the C=O stretching of the ester group and to the N–H bending of primary amide, respectively. The conjugated sample PAMAM-CS sample shows the expected presence of to the C=O stretching

of the ester group at 1735 cm^{-1} and the additional peak at 1660 cm^{-1} due to the C=O stretching of the new amide bond, thus confirming the success of the amidation reaction between the chitosan and the dendrimer.

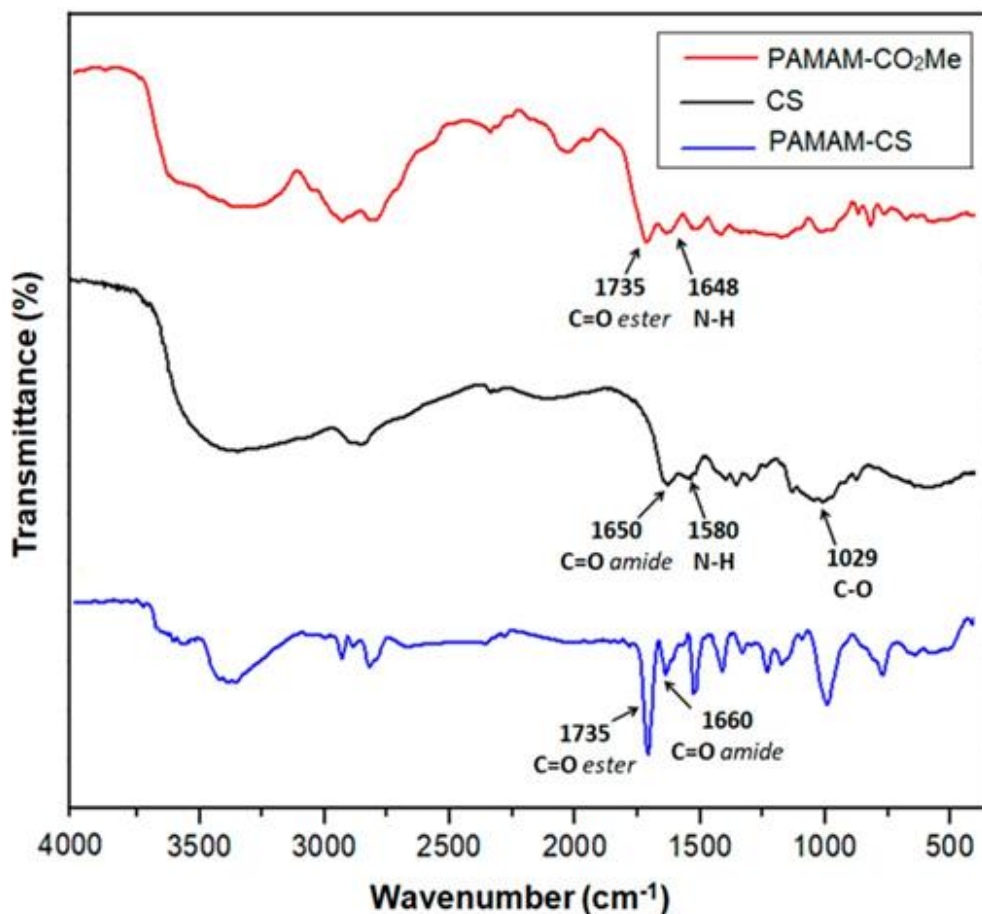


Figure 17. FTIR spectra of CS, CS-PAMAM and PAMAM- CO_2Me samples.

Functionalization of chitosan chains with portions of dendrimers results in an increase in the surface roughness of the corresponding hydrogels compared to the parent obtained with unmodified chitosan (Figure 18).

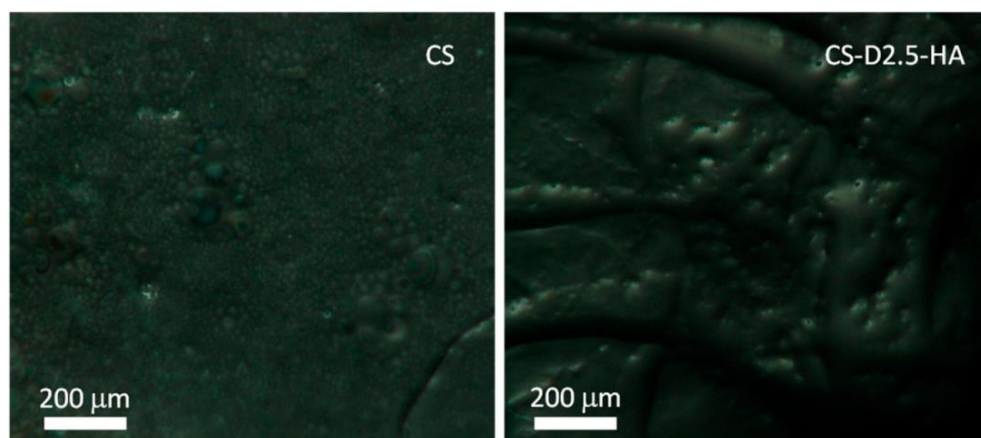


Figure 18. Optical images of CS and CS-D2.5-HA hydrogels

XRD analyses (Figure 19a) confirmed the formation of crystalline hydroxyapatite by obtaining a good overlap between the synthesized material and the hydroxyapatite characteristic line ($\text{Ca}_{10}(\text{PO}_4)_6(\text{OH})_2$, JCPDS 9-432), showing that *in situ* precipitation allows the synthesis of hydroxyapatite with nanometric crystals in the order of 30 nm, thus providing a high bioactivity behavior due to the faster bioabsorption of hydroxyapatite crystals with the surrounding hard tissues. The degree of crystallinity was calculated using Scherrer's equation (Equation 1) using the reflection peak (002) at 2θ 26° , as discussed in Section 5.3.1.

TGA analyses were performed on the CS-D-HA hydrogels and the thermal behaviors were compared with the CS and CS-HA systems; thermal decomposition of chitosan occurs in several steps that include dehydration, changes in the conformation of the molecules, defragmentation and thermo-oxidation and, therefore, changes in thermal behavior reflect structural changes in the chitosan network.

All studied samples, after a vacuum drying procedure, were pretreated at a temperature of 100°C until a constant weight was reached and then heated

up to 700 °C under air flow at a rate of 20 °C/min (Figure 19b). The chitosan sample (CS hydrogel) was totally oxidized and shows two major weight losses in the range 200-350 °C and 400-600 °C. Hydroxyapatite in the chitosan matrix (CS-HA hydrogel) shifts the degradation step toward higher temperatures confirming, as reported in the literature, the hindering effect of hydroxyapatite in the thermal oxidation of the polymer matrix; the residual weight of 35 wt % corresponds to the hydroxyapatite loading in the hydrogel. For hydrogels obtained with chitosan-PAMAM chains (samples CS-D1.5-HA, CS-D2.5-HA, and CS-D3.5-HA), it is possible to highlight two regions where mass loss occurs. In the temperature range of 200-350 °C, mass loss proceeds with a similar profile of samples CS and CS-HA due to the initial thermodegradation of the chitosan matrix; strong mass loss was then observed at increasing temperature ranges for CS-D1.5-HA (350 °C < T < 400 °C), CS-D2.5-HA (385 °C < T < 450 °C) and CS-D3.5-HA (400 °C < T < 500 °C) respectively. The dendrimeric structure in chitosan chains lowers the thermal oxidation resistance of hydroxyapatite-promoted hydrogels, as the presence of hyperbranched PAMAM dendrimers hinders tight packing between chitosan chains, thereby increasing the chain spacing of the biopolymer, which, in turn, increases chain mobility and cleavage. A residual weight of approximately 50 wt % hydroxyapatite was observed for all chitosan-PAM-hydroxyapatite hydrogels, indicating that the spacer effect of dendrimeric moieties allows more hydroxyapatite to be incorporated within the network of chitosan chains.

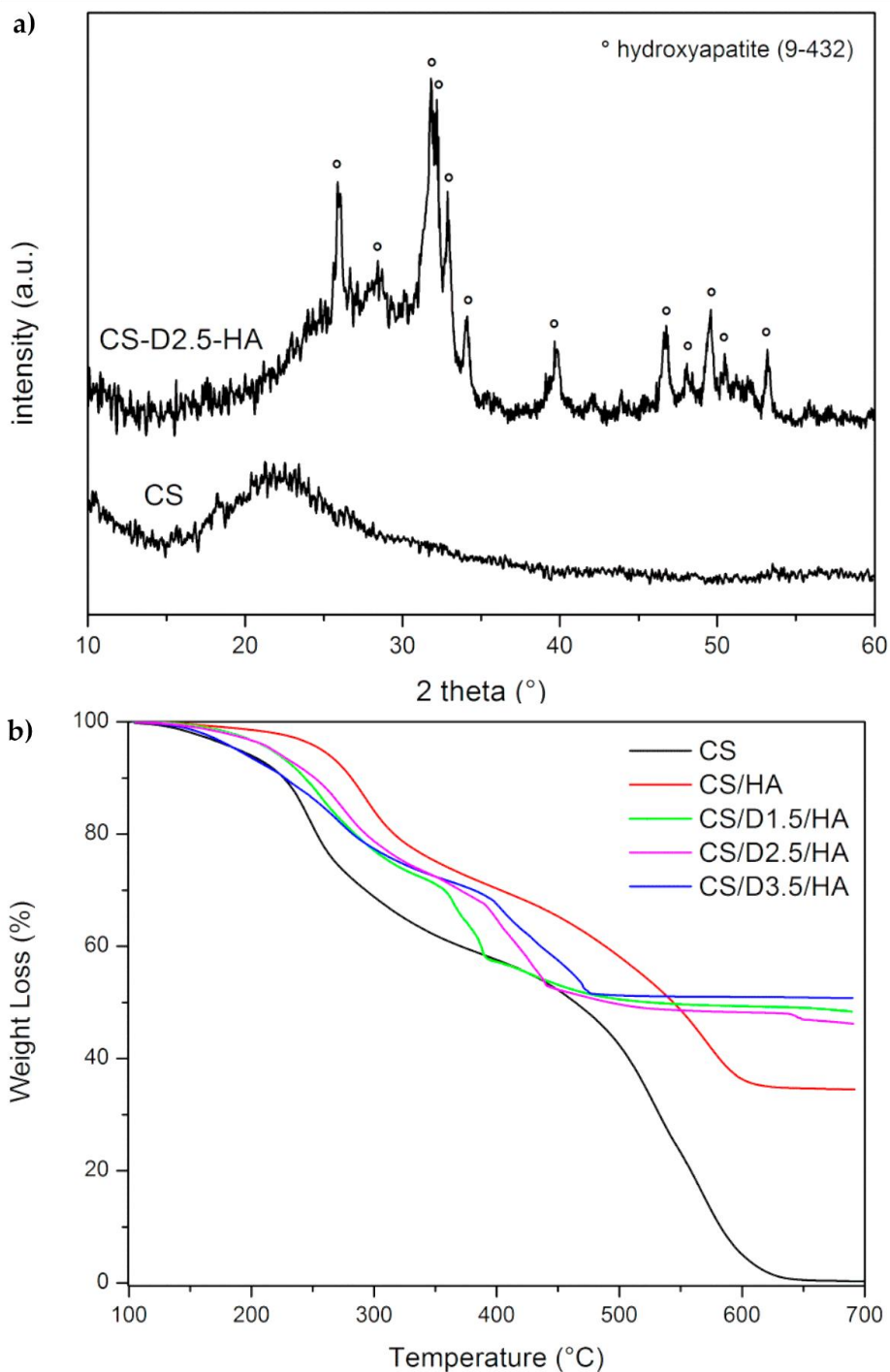


Figure 19. (a) XRD spectra of CS-D-HA hydrogel; (b) TGA curves for CS, CS-HA and CS-D-HA hydrogels. All experiments were performed under air atmosphere.

To study the effect of dendrimeric portions on drug release behavior, hydrogels were loaded with an aqueous solution of ketoprofen (160 mg/2 mL) at a concentration of 4% by weight relative to the weight of the samples, and their release properties were compared. Drug release was studied at a temperature of 37 °C, in phosphate buffer solution (pH = 7.4), and using the dialysis bag diffusion technique with an orbital shaker rotating at 30 rpm. The amount of drug released was quantified by UV-Vis absorption spectra, measuring the absorbance of the drug at 260 nm (Fig. 20). All samples showed similar drug release profiles within the first 16 hours, despite the presence of crystalline hydroxyapatite; this behavior could be associated with the chitosan matrix regulating drug release out of the hydrogel. After this first phase, the cumulative values of released ketoprofen were found to be in the range of 78 to 95 wt %. Hydrogels based on chitosan-PAMAM chains showed a higher amount of released ketoprofen than hydrogels based on unmodified chitosan because of the spacing effect of the dendrimeric structures between the chitosan chains.

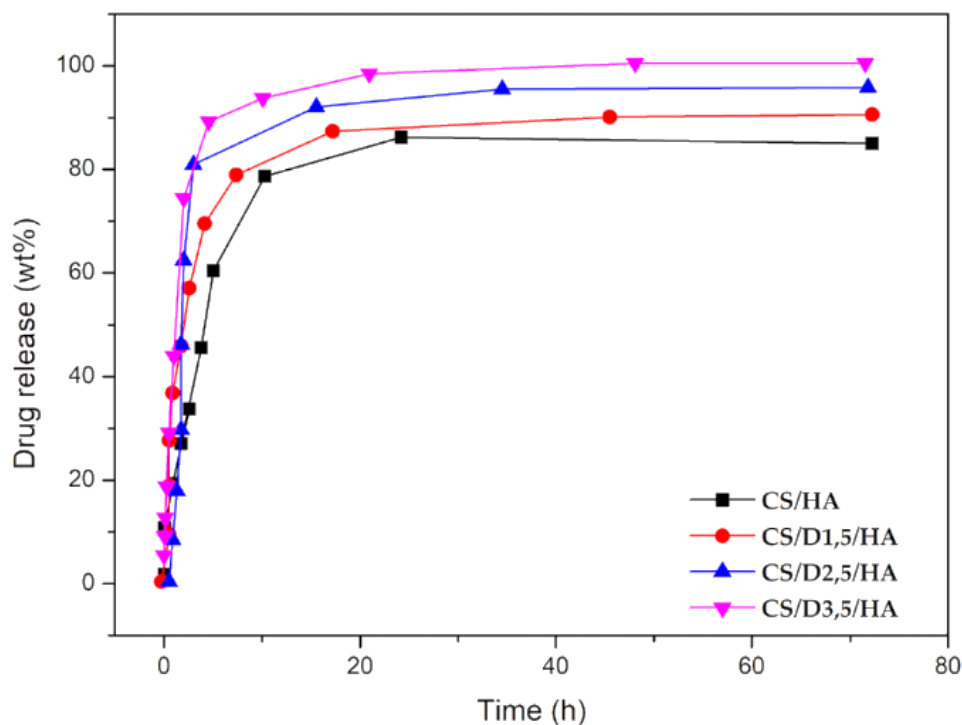


Figure 20. Ketoprofen release from CS-HA- and CS-D-HA-based hydrogel in PBS (pH 7.4), at 37°C.

Scaffolds designed as injectable space-filling agents for implant therapy should possess not only biological but also mechanical properties to match the specific properties of the site to be filled. Through rheological testing, it is possible to study the deformation of a body under the action of a stress. Therefore, the rheological properties of the synthesized hydrogels were studied by performing measurements of the rheological properties in dynamic stress and frequency scan modes to verify the linear viscoelastic region (LVR) and calculate the main rheological properties (i.e. frequency response of G' and complex viscosity). The LVR was determined on cross-linked samples. Figure 21a plots the modulus G' as a function of frequency

for different samples. The stress of 10 Pa to be applied to the samples, within the LVR, was considered as shown in the figure.

This trend was always the same at both the low frequency of 0.1 rad/sec and the higher frequency of 10 rad/sec (Figure 21b). For example, G' at a frequency of 0.1 rad/sec increases from 112 Pa to 151 Pa after the addition of hydroxyapatite to chitosan and then decreases again to 69 Pa after the addition of hydroxyapatite and PAMAM dendrimer.

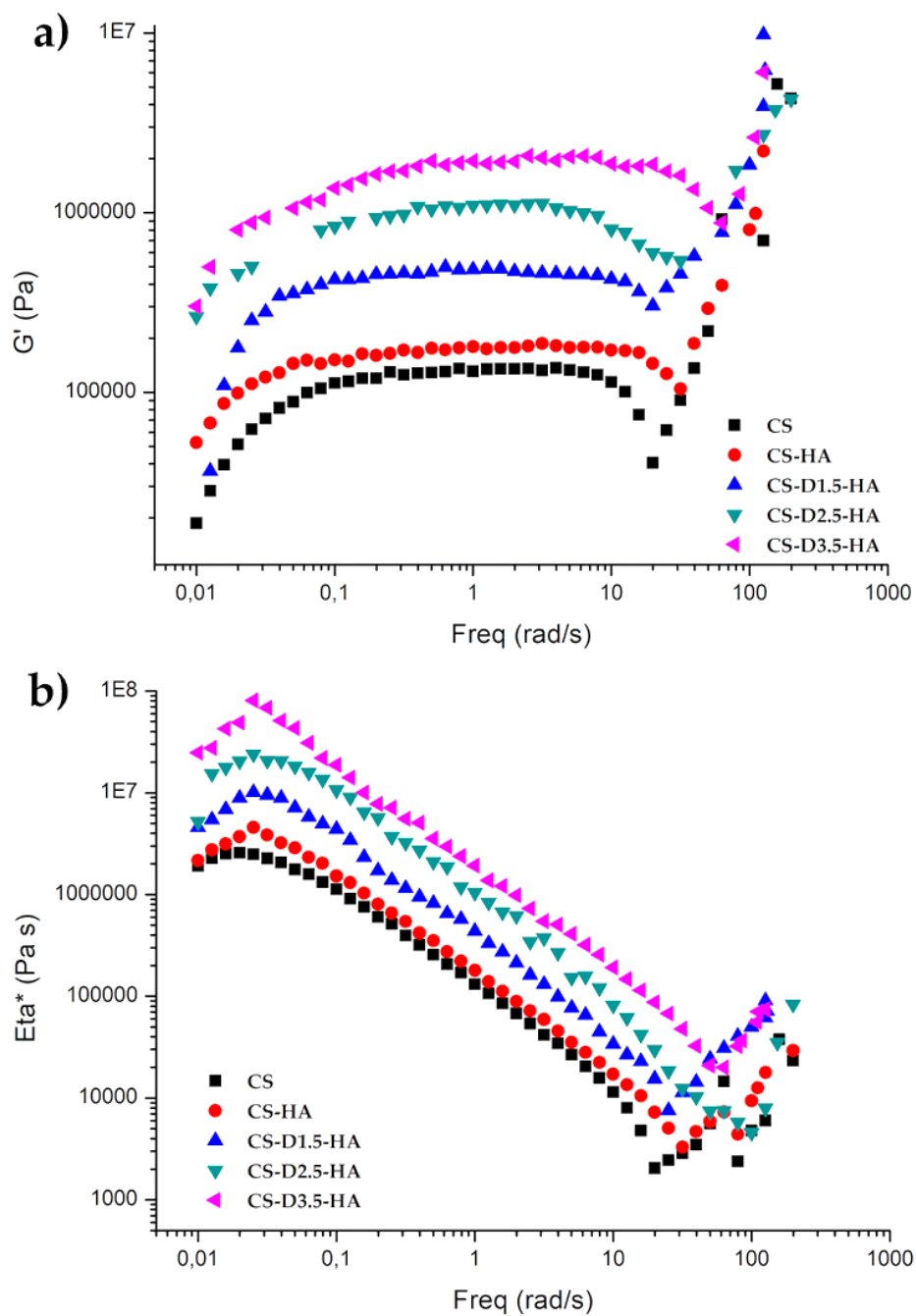


Figure 21. Elastic G' modulus (a) and complex viscosity (Eta^*) (b) vs. frequency for CS, CS-HA, CS-D1.5-HA, CS-D2.5-HA and CS-D3.5-HA samples.

Similarly, at a frequency of 10 rad/sec it increases from 114 Pa to 171 Pa and then decreases again to 102 Pa. This trend is repeated in the values reported in Table 2. Chitosan has a soft texture and ductile behavior. The rheological test results suggest that the addition of HA to chitosan improves the stiffness and, thus, the viscosity of this polymer. Therefore, the CS-HA material has lower ductility than pure CS. The presence of the three different generations of dendrimers in the CS-D(1.5/2.5/3.5)-HA hydrogel again changes the rheological response: the steric hindrance of the dendrimers decreases the overall degree of cross-linking of the polymer matrix, decreasing its structural complexity. Thus, the stiffness (and viscosity) of CS-D(1,5/2,5/3,5)-HA again decreases, resulting in materials that are more ductile, even more so than pure CS.

Table 2. Sample code, composition and rheological features

Sample Code	Freq. 0.1 rad/s		Freq. 10 rad/s	
	G' (Pa)	η^* (10^6 Pa·s)	G' (Pa)	η^* (10^6 Pa·s)
CS	112,752	1.128	114,072	0.011409
CS/HA	151,501	1.519	171,425	0.017144
CS-D1.5-HA	424,121	4.401	428347.7	0.033921
CS-D2.5-HA	838,935	10.665	808,642	0.081778
CS-D3.5-HA	1.36962×10^6	18.821	1.8724×10^6	0.191665

5.5 Synthesis and characterization of functionalized polyhedral oligosilsesquioxane (POSS) based on Chitosan

As discussed in Chapter 3, polyhedral oligomeric silsesquioxanes (POSS), with formula $R_nSi_nO_{1.5}$ have been extensively investigated for the development of composite materials that can induce bone regeneration as well as serve as drug delivery agents. These suitably functionalized inorganic-organic structures can bind to polymers and improve their mechanical and rheological properties. POSS silica cages have been shown to be suitable nanofillers for a wide range of composites for biomedical applications, thus leading to the development of biomedical devices, tissue engineering scaffolds, drug delivery systems, and biosensors. Furthermore, it has been shown that these nanostructured materials can stimulate important biological responses, such as cell adhesion and apatite formation. The cycloaddition of carboxyethyl N-methyl nitron with heptaisobutyl allyl POSS was investigated for the synthesis of these chitosan-based composites (Fig. 22):

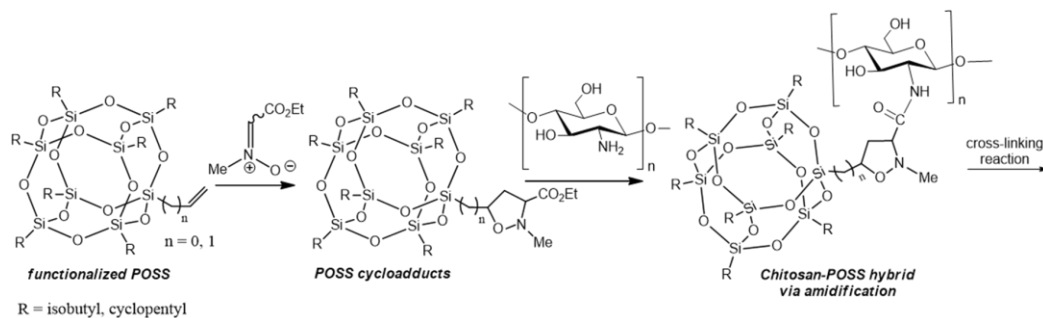


Figure 22. Synthetic process of forming POSS-based composites.

In the first synthetic process, *N, O*-isoxazolidines were obtained through microwave-assisted 1,3-dipolar cycloadditions. The presence of a carboxyethyl group on the isoxazolidine nucleus allowed the chemical bonding with the polymer leading to the CS-POSS composite material that was gelled using genipin as a cross linking agent. Finally, during the gelling process, a drug with anti-inflammatory activity was incorporated in order to study its release over time and to evaluate the ability of the system to retain the drug. The resulting hybrids were characterized by TGA, FTIR and by UV analysis.

In the second synthetic route, chitosan/POSS-based hydrogels were obtained by Michael addition reaction between the amino group of chitosan and the terminal double bond present in the POSS molecule. In order to study how different amount of POSS can regulate the chemical-physical, mechanical, morphological and biological behavior of the composites, 0.5, 1 and 1.5 weight equivalents of POSS were used compared to the used weight of CS. The reaction performed in aqueous solution and at reflux (50 °C) yielded the conjugated compounds which were purified using a dialysis bag capable of holding compounds with MW of 12,000 Da. The samples were then lyophilized for the subsequent characterizations. (Details are included in the experimental section E.S.2)

5.5.1 Characterizations

The covalent conjugation of chitosan with the POSS-ISOX compound leading to CS-POSS was confirmed by thermogravimetric analysis (TGA) performed under nitrogen flow (Fig. 23a). The thermal degradation of pure chitosan shows two stages in the range 50-400°C. The first one (range 50-100°C) is due to water loss with a weight loss of about 9%, while the second stage (range 250-400°C) shows a complete degradation of the sample with a maximum decomposition temperature at 300°C and a total weight loss of about 70%. The POSS-ISOX cycloadduct shows the initial thermal decomposition temperature at 235°C, a maximum decomposition temperature at 293°C, and complete thermal degradation at 600°C. The TGA curve of the CS-POSS hybrid material shows a different profile compared to the chitosan precursors and POSS-ISOX. For this sample, three different stages of weight loss can be observed: the first at 50-100 °C attributable to water loss, the second at 190-300 °C with a maximum decomposition at 254 °C, and the third at 300-400 °C with a maximum decomposition temperature at 371 °C and a complete degradation of the sample with a total weight loss of about 75%. The FTIR spectra of CS-POSS, compared with those of the chitosan precursors (CS) and POSS-ISOX are shown in Fig. 23b. The spectrum of CS shows a strong band at 3150-3600 cm⁻¹ corresponding to stretching of N-H and O-H bonds, peaks at 2850 and 2920 cm⁻¹ due to aliphatic C-H stretching, a band at 1575 cm⁻¹ attributable to N-H bending, a peak at 1030 cm⁻¹ corresponding to C-O stretching, and a peak at 1647 cm⁻¹ due to C=O stretching of the primary amide of the residual N-acetyl groups. The POSS-ISOX compound shows diagnostic signals at 1111 cm⁻¹ attributable to Si-O-

Si stretching of the silica cage, aliphatic C-H stretching of the isobutyl substituents at 2954 cm^{-1} and 2871 cm^{-1} , and the presence of a peak at 1747 cm^{-1} due to C=O stretching of the ester group present at the C-3 position of the isoxazolidine core.

The CS-POSS hybrid sample shows the presence of the diagnostic peak at 1680 cm^{-1} attributable to the C=O stretching of the newly formed amide bond, the presence of a peak at 1550 cm^{-1} attributable to the N-O stretching and a peak at 1250 cm^{-1} due to the absorbance of the C-N bond; in addition, a broad band at $3100\text{-}3600\text{ cm}^{-1}$ of lower intensity than the CS sample can be observed.

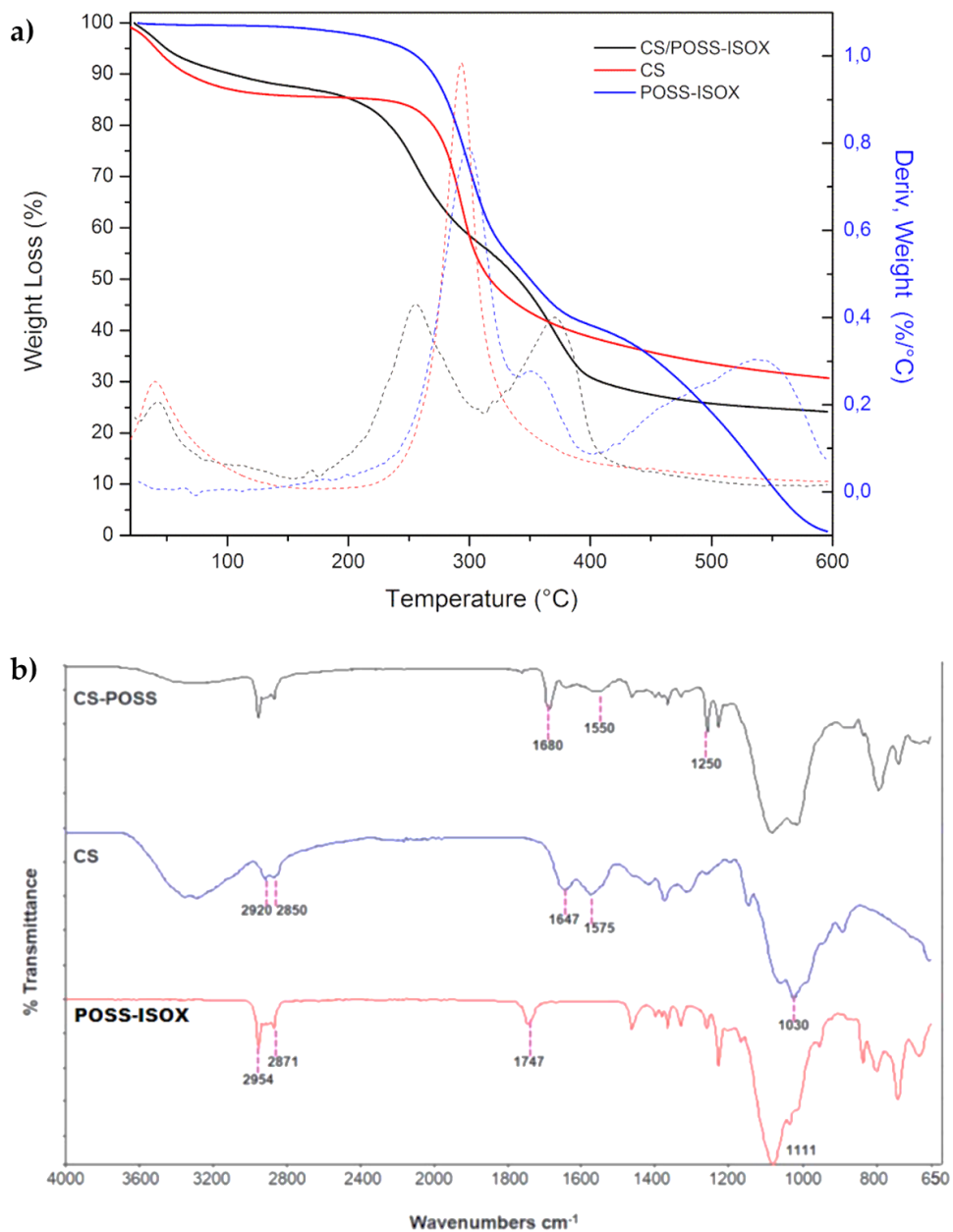


Figure 23. (a) TGA thermograms of CS-POSS, CS, and the POSS-ISOX compound performed in a nitrogen atmosphere; (b) FTIR spectra of the POSS-ISOX, CS, and CS-POSS samples.

The drug release behavior was evaluated from hydrogels obtained from CS and CS-POSS, in order to study the effect of the presence of the silica cage on

the drug release properties of chitosan-based matrices. The study was conducted at a temperature of 37°C, in phosphate buffer solution (pH 7.4) using the dialysis bag diffusion technique. The amount of drug released was quantified by UV-Vis absorption spectra by measuring the absorbance of the drug at 260 nm (Fig. 24). The hydrogel obtained from CS shows a release of approximately 65% of drug within 1 hour, and reaching 100% of released drug within 1 day. For the hydrogel obtained from CS-POSS, the release curve also showed a rapid release of large amounts of ketoprofen (about 45%) in the first hour but a more controlled release over the next 2 days, reaching a plateau at about 78% of loaded ketoprofen. The results of this study suggest the presence of specific intermolecular interactions between the functionalized silica cage and the drug and open up new possibilities for sustained release of trapped drugs within the polymer matrix during its biodegradation *in vivo*.

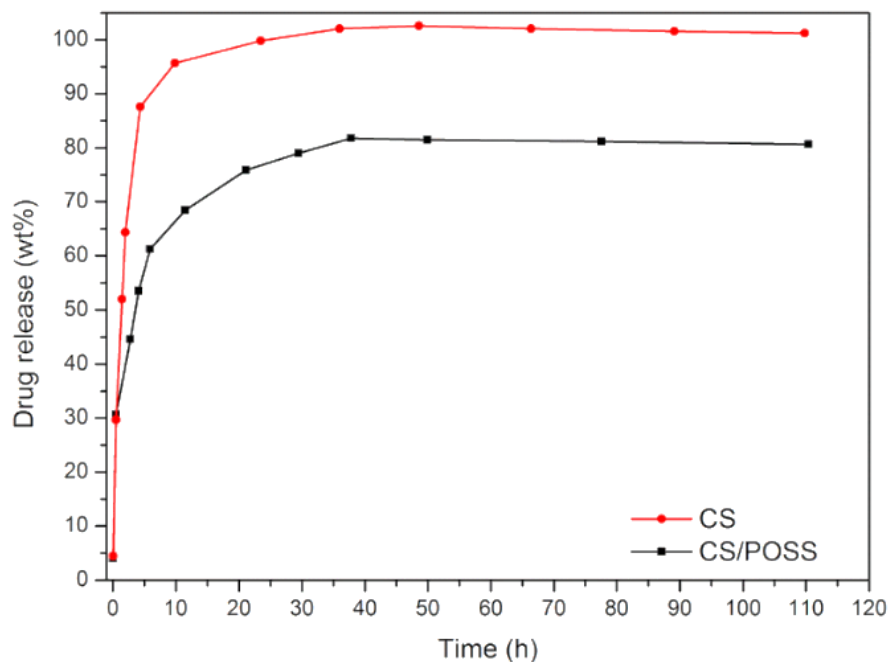


Figure 24. Release of ketoprofen from CS and CS-POSS hydrogels at 37 °C, in PBS (pH 7.4).

Human fetal osteoblastic cells (hFOB 1.19) were used as an *in vitro* model to evaluate the cytotoxicity of the synthesized CS and CS-POSS hydrogels. Both samples were gelled at room temperature and cells were plated and cultured on the formed hydrogels for 48 hours at 34 °C in an atmosphere of 5% CO₂ to simulate the natural environment of living tissues. Cells cultured in their specific medium were used as negative controls. Cytotoxicity studies showed that the hydrogels studied, as assessed using the propidium iodide (PI) DNA intercalating probe and by fluorimetric analysis (λ_{exc} 493- λ_{em} 636 nm) were not cytotoxic to osteoblasts. At the lowest dose tested, the percentages of dead cells were superimposed on control cells (5% 0.3 vs. 5.2 0.4 and 5.4 0.6 CS and CS-POSS hydrogels, respectively). As shown in Fig. 25, a very small increase in mortality rates was observed at the highest doses, highlighting the low cytotoxicity of both hydrogels. Most significantly,

compared with the highly biocompatible CS, the hybrid material increased the rates of cell death by an average of 12%. (Fig. 25)

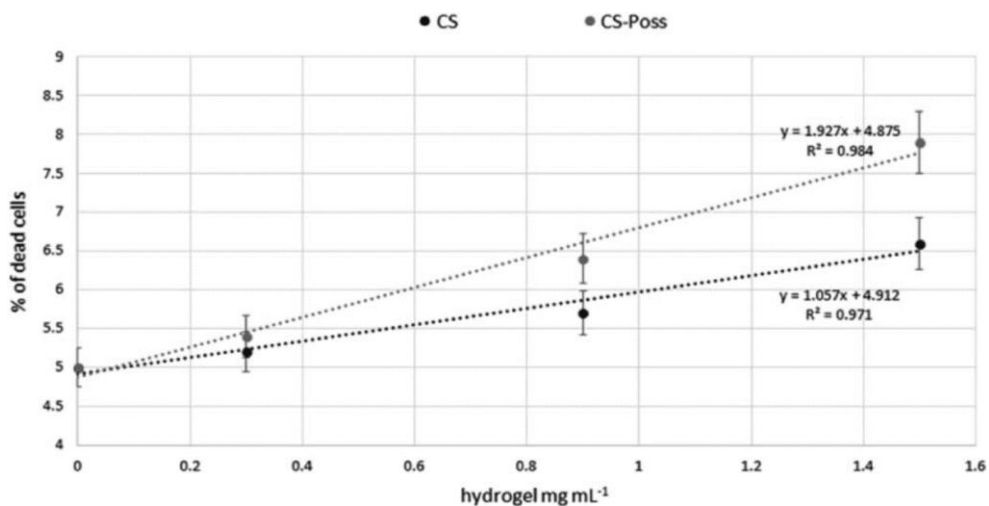


Figure 25. Percentages of dead cells grown in presence of CS and CS/POSS hydrogels.

5.6 Effect of propionaldehyde and lauraldehyde on APTES-based protective coatings.

As discussed in Chapter 4, many attempts have been made in recent years to improve the mechanical properties and fouling resistance of coatings. Poly(dimethyl siloxane) (PDMS) has been widely used due to its properties, including low modulus of elasticity and low glass transition temperature. However, the downside of poly(dimethyl siloxane) coatings has always been their poor adhesion and mechanical properties, which result in easy damage, for example during normal ship handling and navigation, reducing performance and durability, as well as their hydrophobic surface, which results in non-specific protein adsorption and wettability issues. To improve the adhesion and durability (i.e., mechanical properties) of siloxane-based coatings while maintaining their excellent antifouling properties, during my

PhD studies I focused on another strategy to impart adhesion strength by performing surface functionalization reactions with APTES. 3-aminopropyltriethoxysilane (AP) is a bi-functional silane that is of particular interest due to its adjunctive amine functionality. This alkoxide can form a three-dimensional network of oxide silicones in which there is the possibility of binding through the Si-OH and NH₂ end groups. Therefore, APTES was used, exploiting the terminal amine group by reacting it with two aldehydes, propionaldehyde (PP), characterized by a three-carbon atom hydrocarbon chain and lauraldehyde (LA), characterized, in turn, by a twelve-carbon atom hydrocarbon chain, to impart the desired hydrophobic properties. (Fig. 26) (Details are included in the experimental section E.S.3)

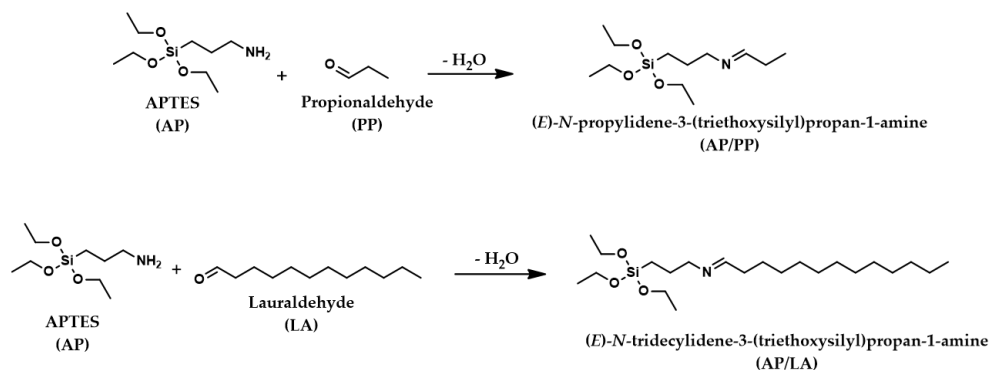


Figure 26. Synthetic scheme of AP/PP and AP/LA coatings.

5.6.1 Characterizations

The Schiff base formation reaction, was carried out firstly, between APTES and lauraldehyde. The reaction was carried out using three different concentrations of aldehyde to study how different amounts of aldehyde can regulate the chemical-physical, mechanical, morphological and biological

behavior of the coatings, and 0.5, 0.6 and 0.7 weight equivalents of aldehyde were used with respect to the used weight of APTES. The reactions were conducted in a closed vial, in the absence of solvent, at 110°C for one hour. Upon completion of the reaction, the obtained compounds were treated with the hydrolysis mixture and placed in an oven at 37°C and then characterized by DSC, TGA, FTIR, wettability, rheology and adhesion tests.

It was observed an endothermic transition around 45 °C in the DSC thermograms of APTES containing systems, that can be attributed to the melting process of the amorphous segment, as also found in the literature. However, this peak disappears at APTES concentrations above 9.7% wt. This result can be explained considering that the degree of cross-linking increases with APTES concentration, reducing the mobility of the chain and thus limiting the ability of the amorphous segments to crystallize.

In addition, DSC data of laurylaldehyde are also reported in the literature; it is characterized by two larger peaks (starting at about 270 and 285 K) attributable to a solid-solid phase transition, typical in long-chain alkyl species, and the melting temperature. Such peaks were found in the synthesized materials (Fig 27a). Further confirmation was given by TGA analyses, conducted in an inert atmosphere up to 800 °C with a speed of 10° C/min, from which the functionalization of APTES can be observed and as a function of weight loss, also the different degree of functionalization. (Fig 27b)

Thermal decomposition of pure APTES sample shows three weight loss phases in the temperature ranges of 40-140 °C, 150-340 °C and 345-600 °C. In contrast, the laurylaldehyde-functionalized samples show a first weight loss

in the temperature range of 100-183 °C and a second loss in the range of 250-550 °C, and the weight loss increases slightly as a function of the weight percentage of lauraldehyde.

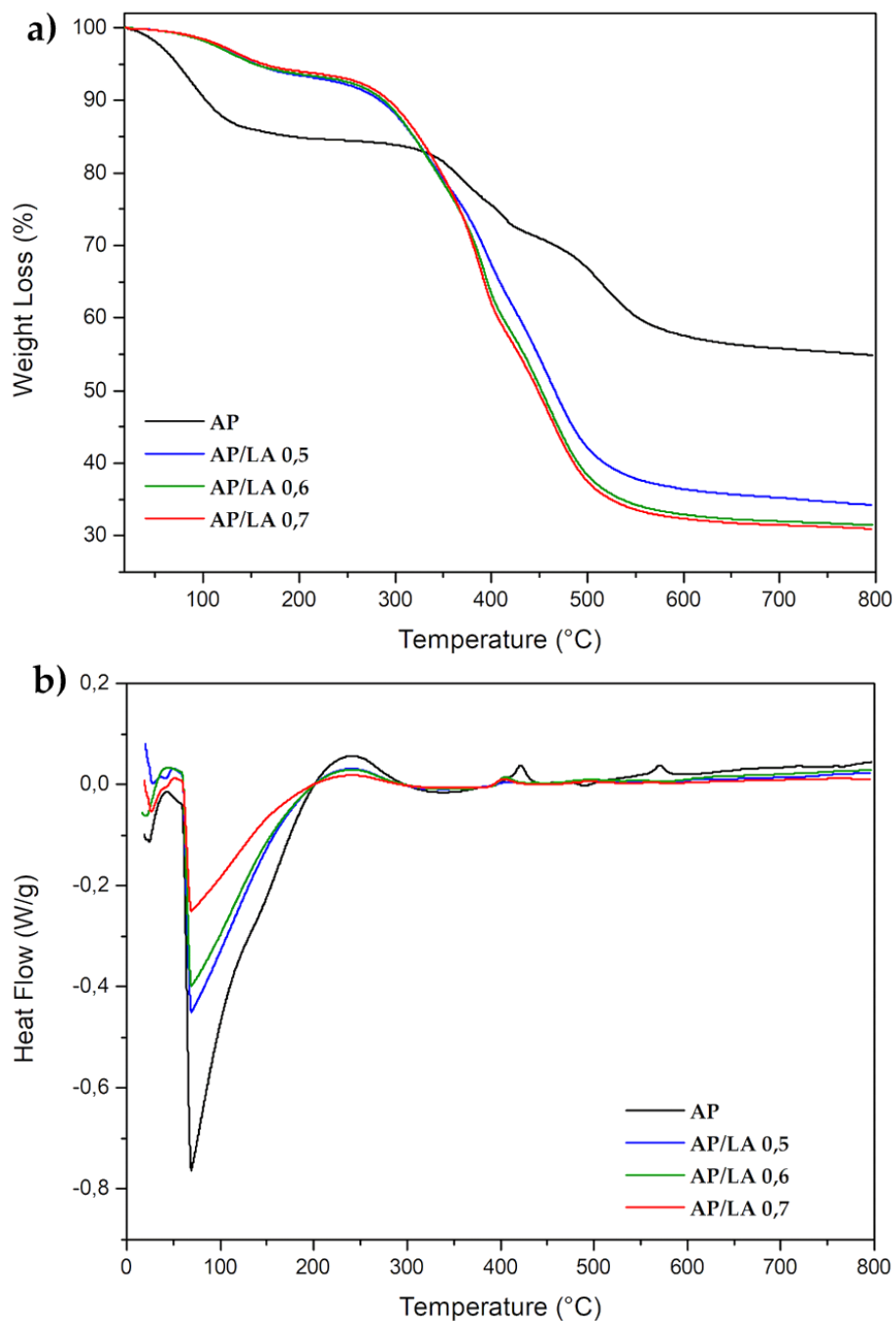


Figure 27. (a) DSC thermograms of AP/LA samples at different concentrations; (b) TGA thermograms of AP/LA samples at different concentrations. All experiments were performed in an inert atmosphere.

The FTIR spectra of the synthesized materials (Figure 28), show vibration bands typical of silica materials such as the symmetric Si-O stretching band at 805 cm^{-1} . In addition, the aliphatic $-\text{CH}_2$ stretching vibration bands of the propyl chain of the silylating agent (APTES) appear at 2927 cm^{-1} and 2855 cm^{-1} in the IR spectrum. The spectral region ($3700\text{--}2800\text{ cm}^{-1}$) is characterized by the characteristic peak of the NH_2 amine group. No bands are observed near 2975 , 1104 and 1089 cm^{-1} from the SiOC_2H_5 groups proving that APTES was completely hydrolyzed. Comparing the two spectra, the expected vibration band of the azomethine group ($-\text{C}=\text{N}-$) can be seen, which appears at 1629 cm^{-1} . Therefore, the binding between APTES and laurylaldehyde is confirmed by FT-IR spectroscopy.

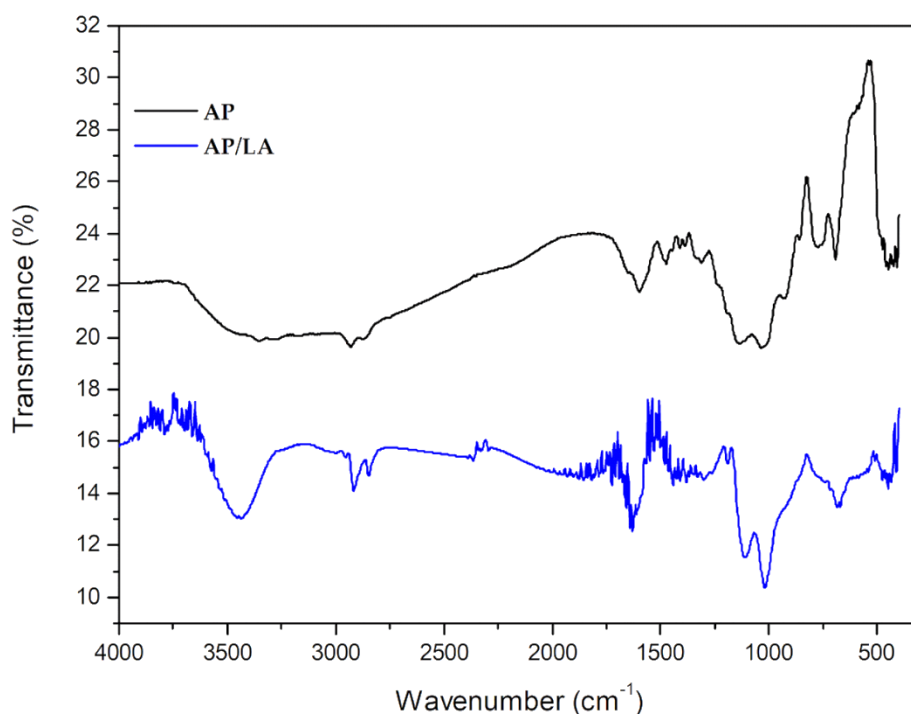


Figure 28. FTIR spectra of APTES, APTES/Laurylaldehyde.

To verify the hydrophobic behaviour of the prepared surfaces, the contact angle (θ) with water was measured. A drop of distilled water with a volume of 1 μl was deposited and the water contact angles were measured three times at different positions on a sample surface, calculating the average value. It was obtained for AP sample, a contact angle value of 107.90° , for AP/LA0.5 sample equal to 144.89° , for the sample AP/LA0.6 equal to 108.11° ; and finally for the sample AP/LA0.7, a value of 108.45° . (Fig 29) The samples all presented hydrophobic characteristics and in particular the material with values almost close to super hydrophobicity was the sample AP/LA0.5.

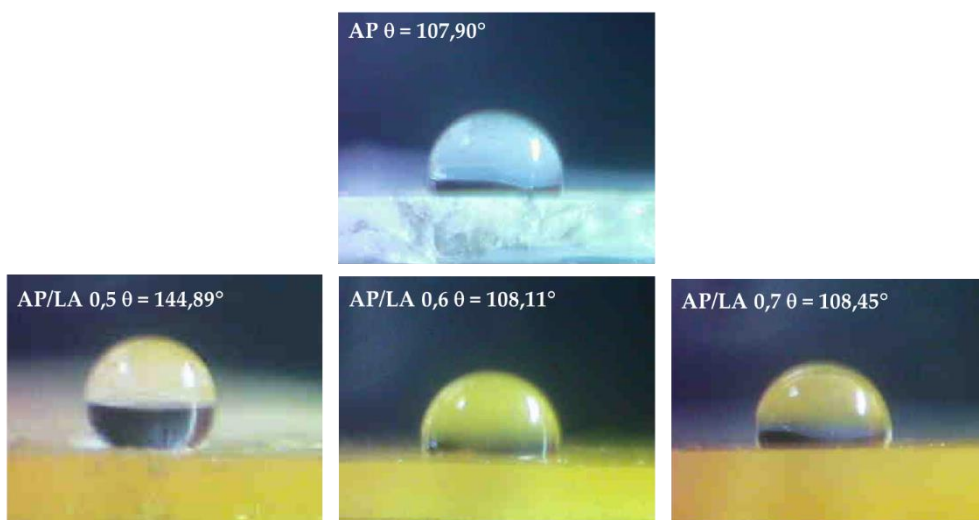


Figure 29. Images of the contact angles of AP and AP/LA at different concentrations.

Once the optimal parameters for the formation of these coatings were established, we proceeded to the synthesis of APTES with propionaldehyde, in order to highlight the effect that the different lengths of the hydrocarbon chains may have on the properties of the coatings. The imine formation reaction was conducted using 0.5 weight equivalents of aldehyde with respect to the weight of APTES, as from previous characterizations

conducted on APTES and lauraldehyde based coatings, the 1/0.5 ratio proved to be the best. Reactions were conducted in a closed vial, in the absence of solvent, at 110°C for one hour. At the end of the reaction, the obtained compounds were treated with five equivalents of a solution of H₂O/HCl (10:1), and placed in an oven at 37°C for the subsequent characterizations.

TGA and DSC analyses (Fig 30), were carried out in an inert Argon atmosphere up to 800 °C with a speed of 10° C/min, and confirmed the successful functionalization of APTES, and depending on the weight loss, also the different degree of functionalization. As discussed above, thermal decomposition of the pure APTES sample shows three phases of weight loss in the temperature ranges of 40-140 °C, 150-340 °C, and 345-600 °C. The AP/LA sample shows a first weight loss in the temperature range of 100-183 °C and a second loss in the range of 250-550 °C, while the AP/PP sample shows three phases of weight loss in the temperature ranges of 70-175 °C, 200-430 °C and 450-560 °C.

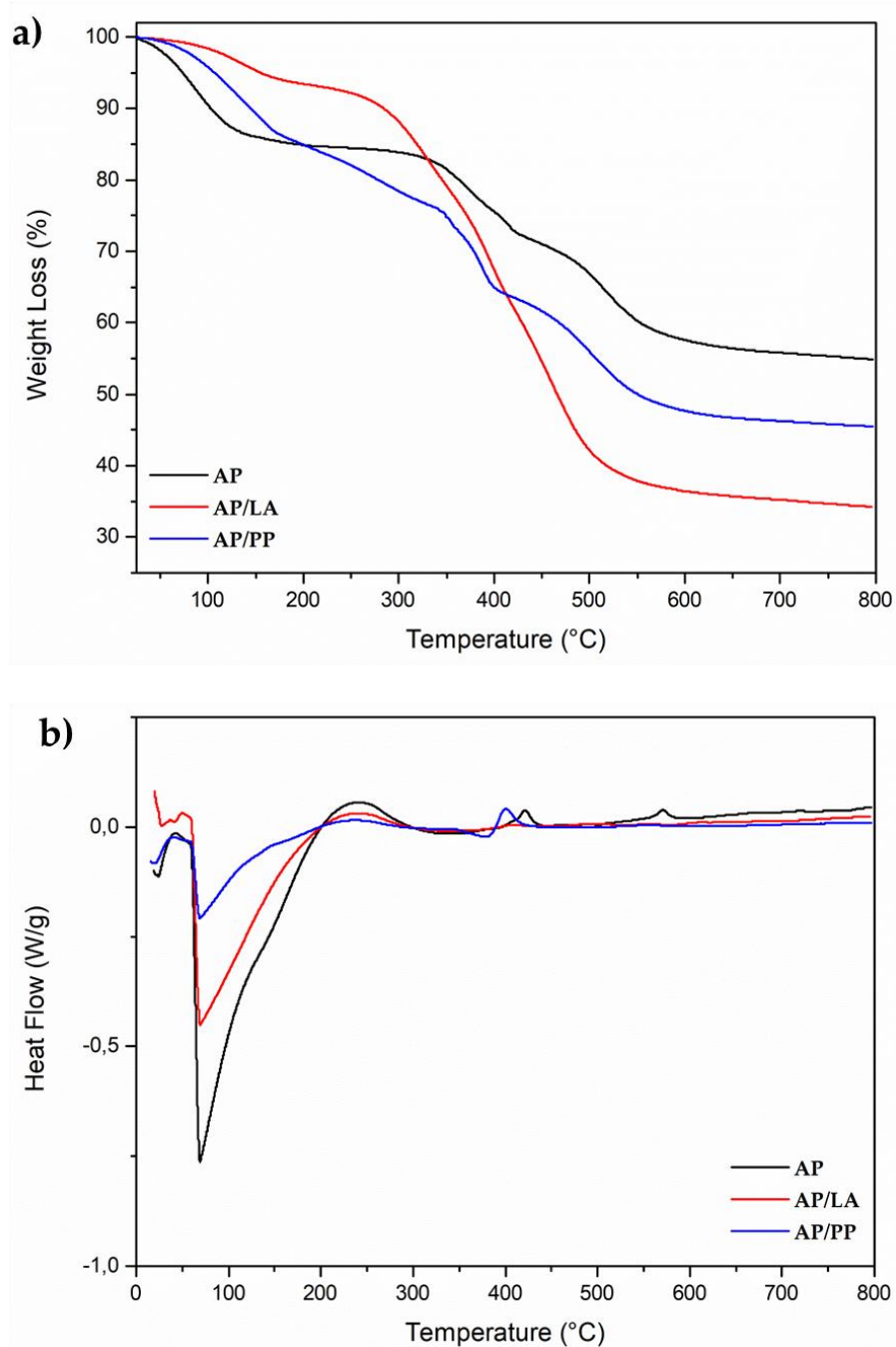


Figure 30. (a) TGA curves of AP, AP/PP, and AP/LA samples in 1:0.5 ratio; (b) DSC curves of AP, AP/PP, and AP/LA samples in 1:0.5 ratio. All experiments were performed under inert atmosphere.

In the FTIR spectra of the synthesized materials (Fig 31), the expected vibration band of the azomethine group ($-C=N-$) can be seen, which appears at 1629 cm^{-1} , confirming that binding of APTES with the different aldehydes has occurred.

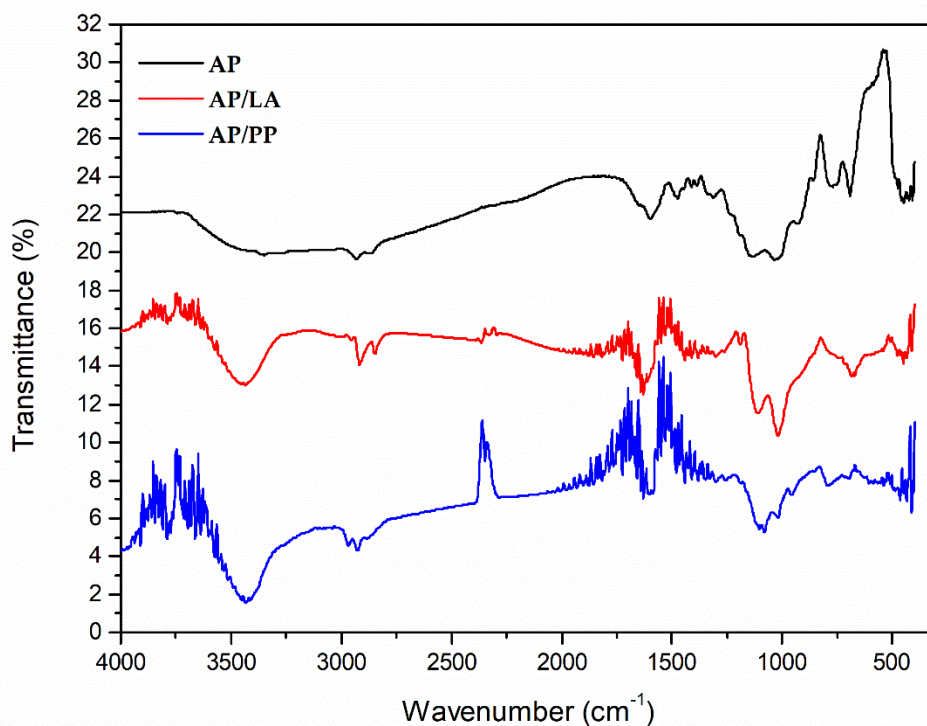


Figure 31. FTIR spectra of AP, AP/PP, and AP/LA in 1:0.5 ratio.

Functionalization of APTES chains with the aldehyde moiety increases the surface roughness compared to unmodified AP.

In fact, the AP a roughness of $R_a=0.48\text{ mm}$, while the AP/PP and AP/LA samples show an increase in roughness from the R_a value of 0.63 mm and 0.82 , respectively. In the images associated with the graph in Figure 32 and from Table 3, it can be seen that both Wenzel/Young contact angles increase while increasing the side chain length from $108.83^\circ/120.76^\circ$ in AP/PP, to $144.89^\circ/176.05^\circ$ in AP/LA, respectively.

The apparent static contact angle θ_w depends on the surface morphology. In fact, every surface has heterogeneities, and when there is full contact between the liquid and the substrate, or if there is air trapped between the surface roughnesses, the measured contact angle θ_w may differ from the ideal contact angle θ_y . The comparison of the contact angles θ_w and θ_y of the coatings shows an ideal increase in the value of contact angle θ_y over that of θ_w in a range from 120.76° (AP/PP) to 176.05° (AP/LA).

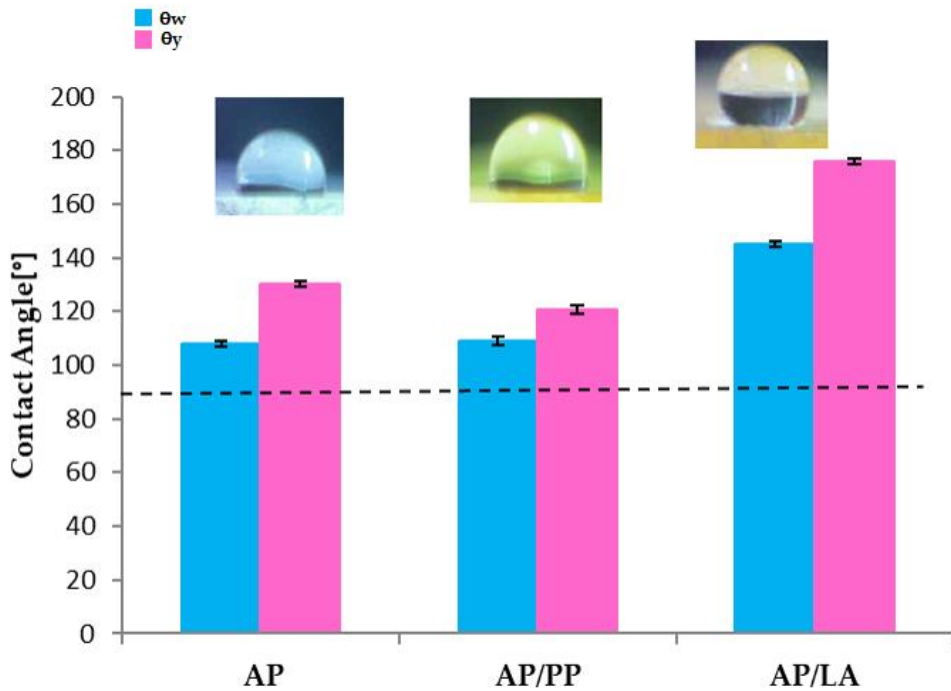


Figure 32. Comparison of contact angles θ_w and θ_y AP, AP/PP, and AP/LA in 1:0.5 ratio.

Table 3. Sample code, and Wenzel/ Young contact angles.

Sample code	θ_w (°)	θ_Y (°/μm)
AP	107.90 \pm 1.09	130.12 \pm 1.09
AP/PP	108.83 \pm 1.52	120.76 \pm 1.52
AP/LA	144,89 \pm 1.08	176.05 \pm 1.08

Figure 33 shows the graphs G'/G'' vs time. As is well known, the gel point represents the transition from fluid to solid state. The values of the gel point are listed in Table 4. This phase change is due to the crosslinking reactions that occur between AP and the two aldehydes. The gel point of pure AP sample is 2019 Pa. It grows up to in the to 2960 Pascal in the AP/PP sample and up to a value of 5348 Pa in the AP/LA sample. Thus, the increasing of the length of the aliphatic chain causes an increase in the crosslinking rate, and consequently, an increase of its structural stiffness.

This can be observed in the graph of figure 33a that is referred to the conservative modulus G' vs the cure reaction time. At parity of reaction time, the stiffness grows in the order:

$$\text{AP} < \text{AP/PP} < \text{AP/LA}$$

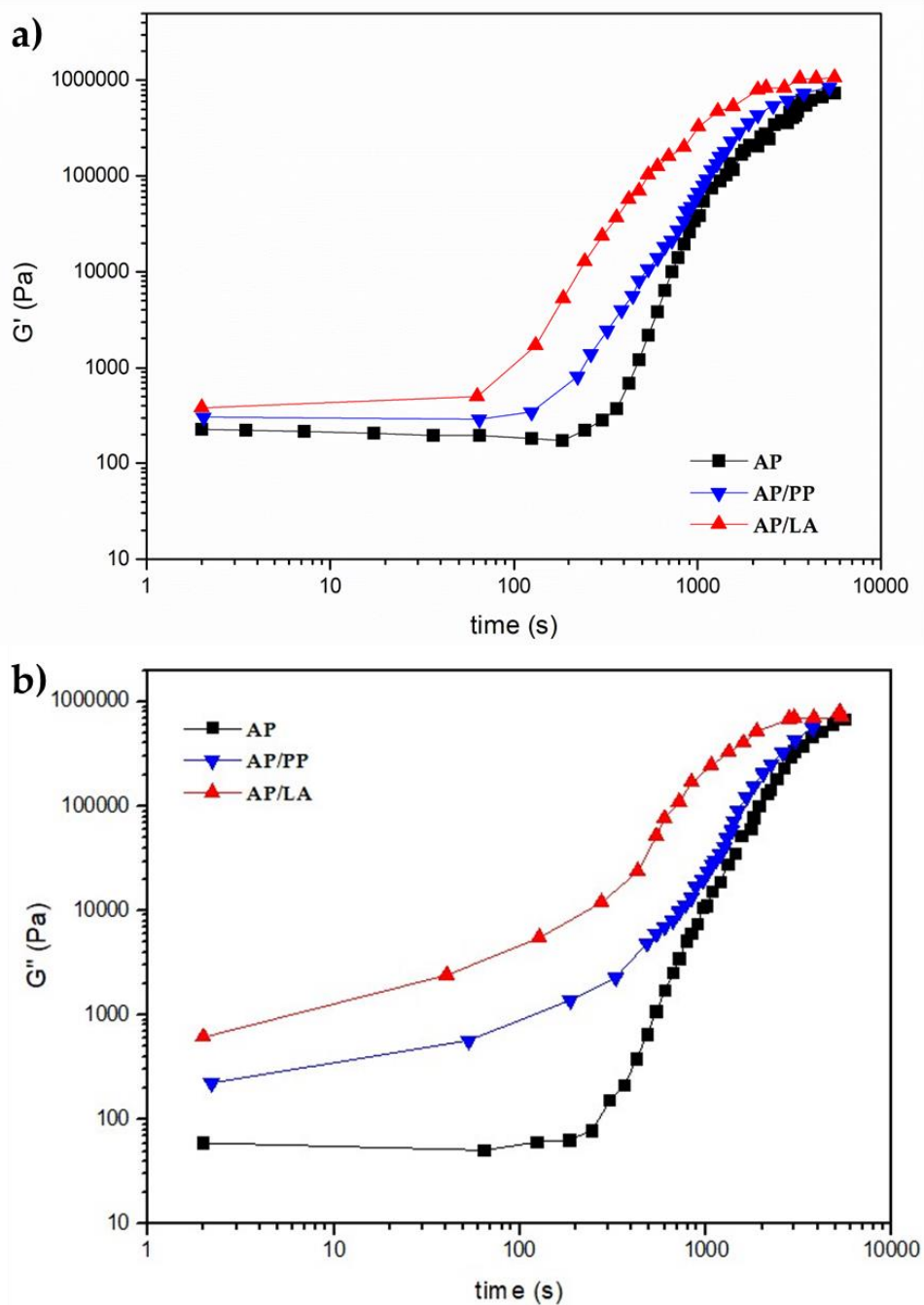


Figure 33. Elastic and loss modulus (G' and G'') vs time of AP, AP/PP, and AP/LA in 1:0.5 ratio.

The complex viscosity vs time of the synthesized coatings can also be seen from the graph in Figure 34. From the trend of the various curves, it can be

easily seen that there is a marked increase in complex viscosity as the side chain length increases in the order:

$$AP < AP/PP < AP/LA$$

Finally, Table 4 also shows the value of the complex viscosity going from a value of 36 Pa·s in the pure sample, to a value of 70 Pa·s in the AP/PP sample, to a value of 113 Pa·s in the AP/LA sample.

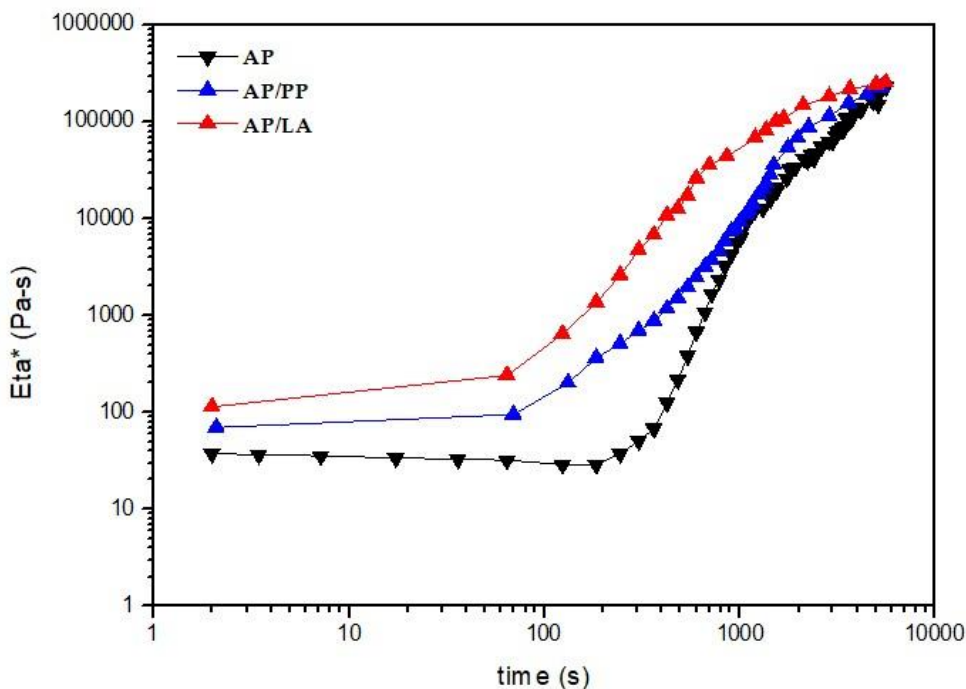


Figure 34. Complex viscosity (η^*) vs time of AP, AP/PP, and AP/LA in 1:0.5 ratio.

Table 4. Rheological parameters of the studied coatings.

Sample code	Gel point (Pa)	η^* (Pa·s) at t=0 sec
AP	2019	36
AP/PP	2960	70
AP/LA	5348	113

The pull-off method was used to evaluate the mechanical strength of adhesion of silica-based coatings with the DH36 steel substrate. The test was

performed by attaching small metallic dollies perpendicular to the metal specimens (see the image in Figure 35a). The applied force was gradually increased and monitored until it becomes larger than the bond force between the coating and the substrate: a fracture occurs and the dynamometer detaches the coating from the substrate. (Figure 35 b, c).

The nature and type of dolly fracture from the test plane, was carefully evaluated by visual inspection, according to ASTM D4541-02 or ISO4624:2016. Figure 35e shows the image of the detached metal surface, and each detached dolly after the pull-off test performed with APTES/Lauraldehyde coating adhesion. Such coating breaks at an average tensile stress of 12.80 MPa. Visual inspection of the fracture surface on both sides (dolly/substrate) reveals an average value of material removed from the dolly of approximately 70% compared to the initial joint still adhered to the dolly. This indicates that the fracture was of the adhesive type at the interface between the dolly and the liner. This type of adhesive fracture was also found for all other sets of samples.

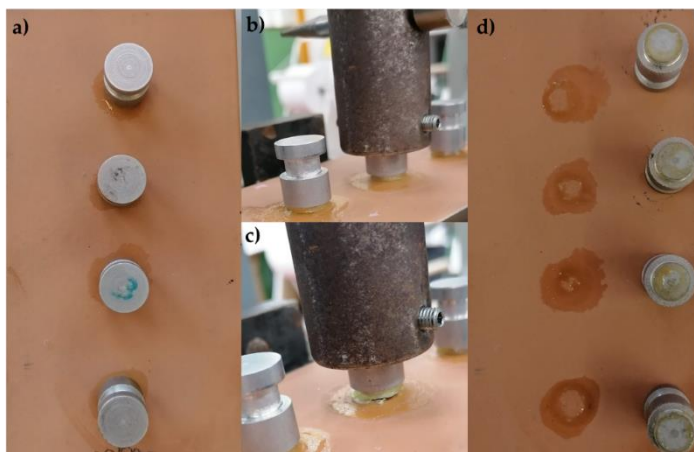


Figure 35. Pull-off Test: (a) Image of the sample AP/LA; (b, c) step of breaking the specimen from the metal substrate; (d) image of the metal specimen and the dolly after the pull off test for the sample AP/LA.

The stress/strain curves of three studied liners are plotted in the graph in Figure 36. The mechanical parameters are detailed in Table 5, where E is the Young's modulus [MPa]; σ_y is the yield stress; $\varepsilon_y\%$ is the yield percentage deformation; σ_{\max} is the maximum stress [MPa]; σ_r is the stress at break [MPa]; $\varepsilon_r\%$ is the percentage deformation at break [%]; L_r is the load at break [N]; W_r is the work at break [J]. The mechanical behavior, which is highly significant ($p < 0.0001$), became that of a more rigid, strong and tough coating than pure APTES. It is possible to notice how:

-Young's modulus improves from 36 and 46 MPa, in APTES and APTES/Propionaldehyde coating, respectively, up to 154 MPa in APTES/Lauraldehyde coating;

-the strength at break improves from 0.09 MPa, in the pure APTES to up to 0.18 and 0.16 MPa in the APTES/Propionaldehyde and APTES/Lauraldehyde coatings, respectively.

-the strength at yielding grows from 0.11 MPa in the pure APTES to up to 0.21 and 0.48 MPa in the APTES/Propionaldehyde and APTES/Lauraldehyde coatings, respectively.

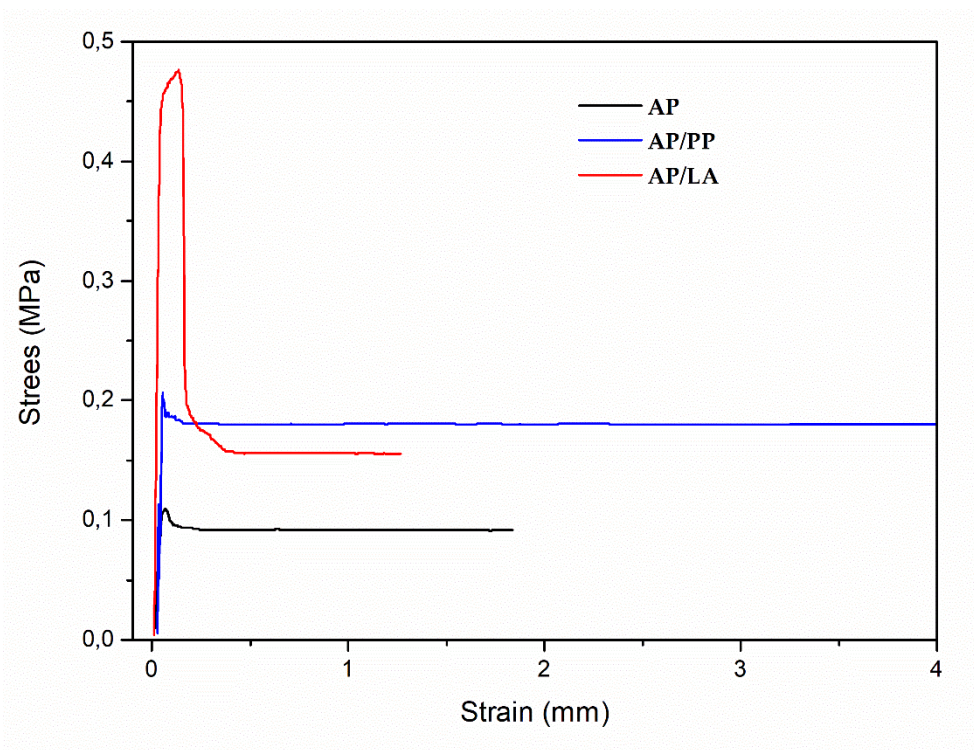


Figure 36. Stress/strain curves of AP, AP/PP, and AP/LA coatings.

Table 5. Mechanical characterization of AP, AP/PP, and AP/LA coatings.

Sample code	E [MPa]	σ_y [MPa]	ϵ_y [%]	σ_{max} [MPa]	σ_r [MPa]	ϵ_r [%]	load r [N]	L_r [J]
AP	36,11±1,69	0,11±0,01	0,71±0,039	0,11±0,008	0,09±0,005	18,61±1,22	7,07±0,27	0,0128±0,0010
AP/PP	46,94±1,44	0,21±0,01	0,17±0,001	0,21±0,006	0,18±0,007	13,20±0,05	5,23±0,48	0,0024±0,0013
AP/LA	154,55±2,79	0,48±0,02	1,35±0,041	0,48±0,033	0,16±0,063	12,80±0,10	11,93±0,10	0,0020±0,0007

The results of the adhesion tests again showed that the length of the aliphatic side chain in the coatings induces a significant change in its mechanical strength, due to the structural change shown by the rheological data.

Thus, in agreement with the rheological and calorimetric tests, the presence of carbon chains also plays a key role in the adhesive tests as it facilitates the

crosslinking of APTES. Therefore, the effectiveness of this silane modification, improves the adhesion strength of the coatings. Again, the adhesion strength grows in the order:

$$AP < AP/PP < AP/LA$$

5.7 Effect of glutaraldehyde on APTES based protective coatings.

Another strategy to confer adhesion strength using APTES was to use glutaraldehyde as a linker, as it is known that with the help of this bifunctional aldehyde, it is possible to uniformly immobilize biomolecules on the surface of these coatings. Therefore, APTES (AP) was used in this study by exploiting the terminal amine group, by reacting it with glutaraldehyde (GA) to help the crosslinking process. (Fig. 37) (Details are included in the experimental section ES.3)

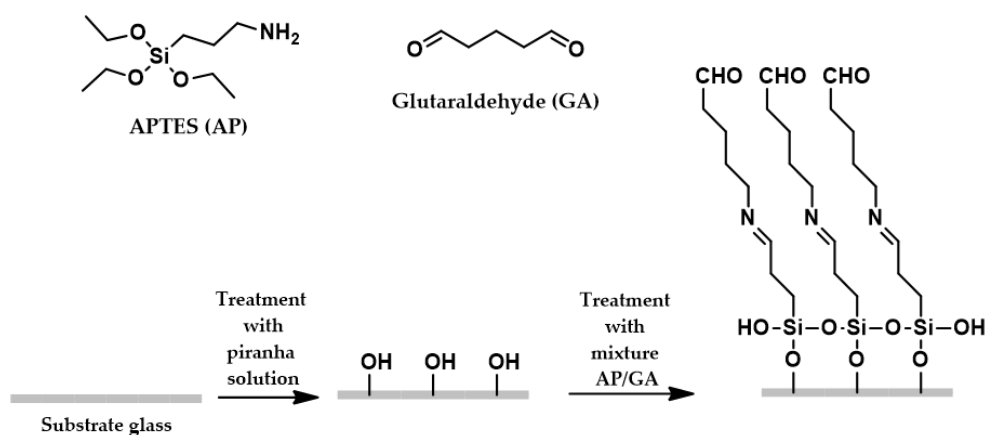


Figure 37. Schematic representation of APTES and Glutaraldehyde coatings.

5.7.1 Characterizations

(3-Aminopropyl)-Triethoxysilane (AP)-based coatings were synthesized at wt % increasing glutaraldehyde (GA), and were characterized by optical microscopy, contact angle analysis, rheological studies, and adhesion tests. The results obtained showed the effectiveness of the AP modification; in particular, the AP/GA 0.3 sample showed the best performing properties among the synthesized materials in terms of adhesion, wettability, rheological properties and thermal stability.

The AP and AP/GA coatings were deposited on glass substrates, previously activated by a mixture constituted by $\text{H}_2\text{SO}_4/\text{H}_2\text{O}_2$ in a 3:1 ratio. Figure 38 shows the sequence of images of the AP and AP/GA samples during their cross-linking reaction at room temperature and were taken every 15 min after mixing of the two components; images of the pure AP coating were taken as reference. All samples showed a uniform structure on the glass substrate, without cracks. The reaction between glutaraldehyde and APTES results in a change in the colour of the coating, from opaque white (typical of AP coating) to red. The colour change appears much earlier with increasing glutaraldehyde content. This suggests that the higher the GA content, the faster the crosslinking reaction between GA and AP. Specifically, the starting times are: ≥ 90 minutes in AP/GA 0.01, ≥ 75 minutes in AP/GA 0.03 and AP/GA 0.05, ≥ 45 minutes in AP/GA 0.1, and about 30 minutes in the AP/GA 0.3 sample, as indicated by the arrows within Figure 38. These changes of colour suggested us a different time of cross-linking necessary for the different GA contents. In particular, the highest is the GA amount, earlier the cross-linking reaction occurs, as suggested by the chromatic variation.

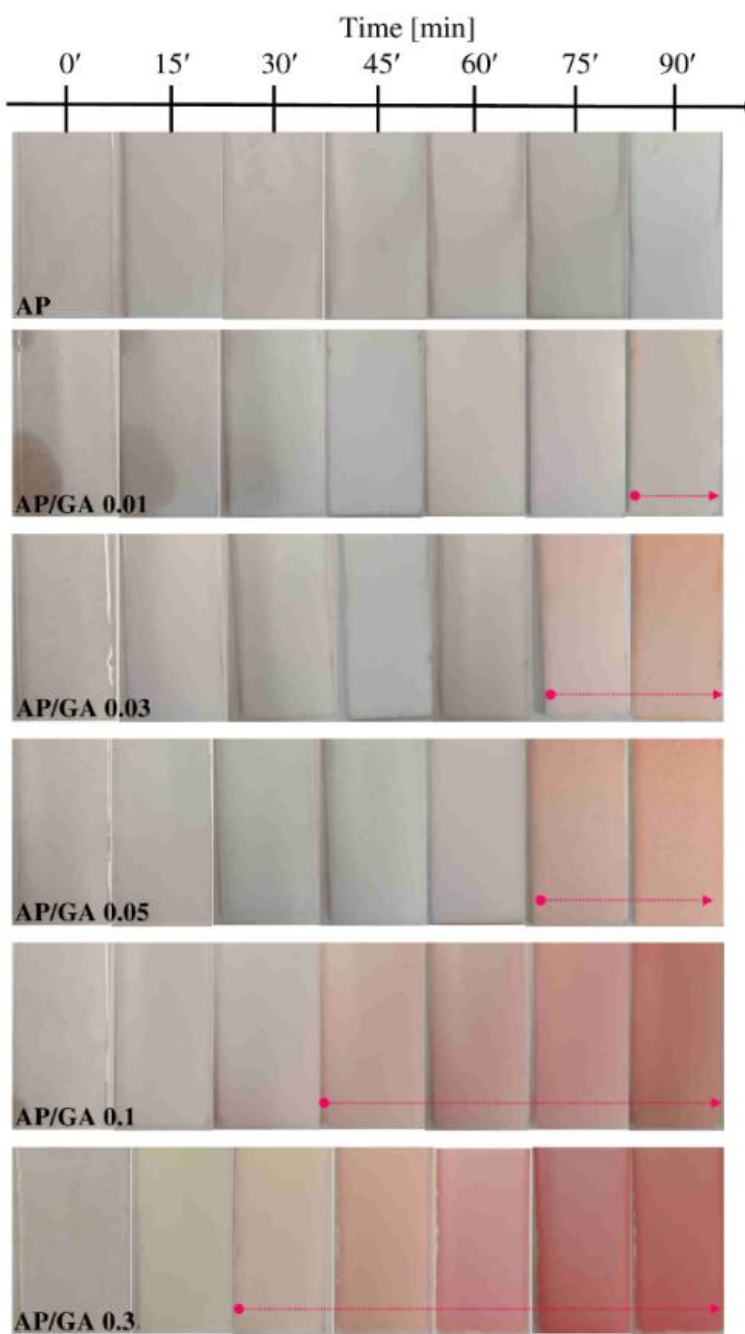


Figure 38. Images of AP and AP/GA coatings deposited on glass, taken every 15 minutes after mixing the two components.

TGA analyses were performed on the AP/GA coatings at different wt% of GA, and the thermal behavior was compared with the AP system. Thermal decomposition of the samples shows weight loss in the range 50/200 °C, with a shoulder at 150 °C. (Fig. 39a) In addition, the glutaraldehyde cross-linked samples show three weight loss phases in the temperature ranges of 40-150 °C, 180-200 °C, and 300-600 °C, and the weight loss increases slightly as a function of wt % GA.

In agreement with the TGA analyses, the DSC thermograms, (Fig. 39b), reveals the initial loss below 220 °C that is related to water adsorbed on the silicon surface, to the residual trapped ethanol, and to the partial decomposition of unreacted APTES. The second phase of mass loss is between 220 and 900 °C: it represents the degradation of the residual starting materials and the decomposition of the organo-functional group. The results showed that the modified silica is thermally stable above 500 °C.

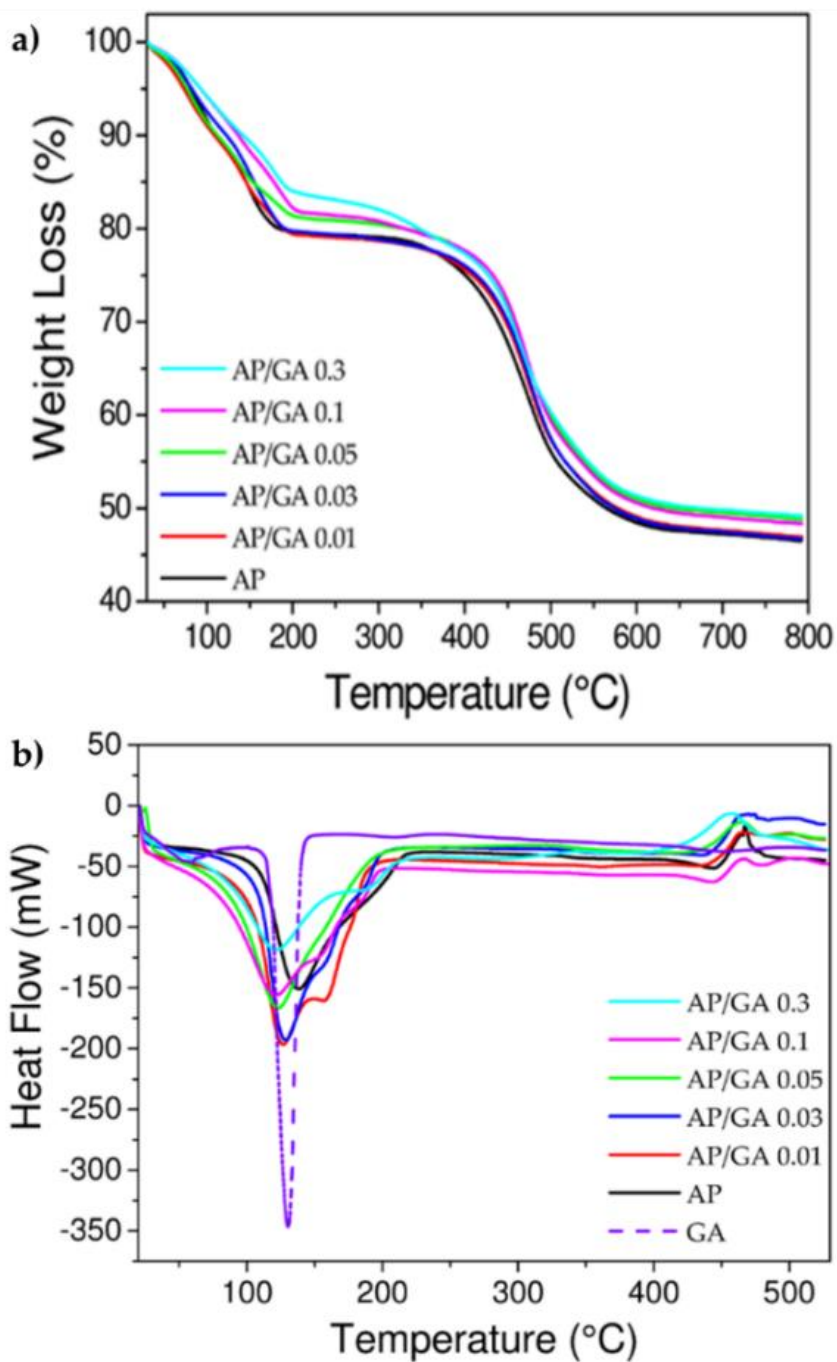


Figure 39. TGA (a) and DSC (b) thermograms for AP, GA and AP/GA coatings. All experiments were performed under inert atmosphere.

Functionalization of APTES chains with the aldehyde moiety leads to a highly significant increase in surface roughness compared to the unmodified AP.

The roughness (R_a) decreases when the aldehyde concentration increases (Figure 40). In fact, all AP/GA samples, compared to AP ($R_a=4.08 \mu\text{m}$), show a decrease in roughness from the R_a value of $3.96 \mu\text{m}$ for AP/GA 0.01 to the R_a value of $2.41 \mu\text{m}$ for AP/GA 0.3.

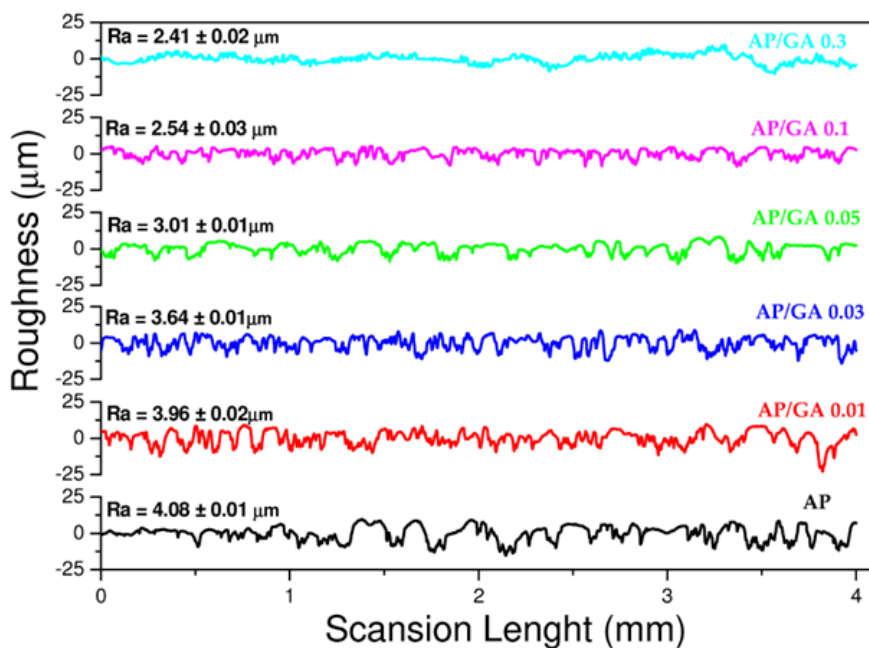


Figure 40. Surface roughness profiles of AP and AP/GA samples at different wt % of GA.

In the images associated with the graph in Figure 41 and from Table 6, it can be seen that all AP/GA coatings exhibit a higher and highly significant contact angle (and thus wettability), compared to the AP coating whose contact angle is less than 90° (27.34°). Considering that, hydrophobic coatings show a contact angle $\theta < 90^\circ$ while hydrophilic ones have $\theta > 90^\circ$, AP has hydrophilic characteristics, which changes after glutaraldehyde treatment to hydrophobic ones. Both Wenzel/Young contact angles increase

with increasing amount of GA, from $96.23^\circ/91.57^\circ$ in AP/GA 0.01, to $119.34^\circ/101.75^\circ$ in AP/GA 0.3, respectively.

The apparent static contact angle θ_w depends on the morphology of the surface. Indeed, every surface has heterogeneities, and when there is complete contact between the liquid and the substrate, or if there is air trapped between the surface roughness, the measured contact angle θ_w differs from the ideal contact angle θ_Y . The comparison of the contact angles w and Y of AP and AP/GA coatings at different wt % GA shows an ideal decrease in the value of the contact angle θ_Y relative to that of θ_w in a range from 91.57° (AP /GA 0.01) to 101.75° (AP/GA 0.3), which instead increases only in the pure AP sample.

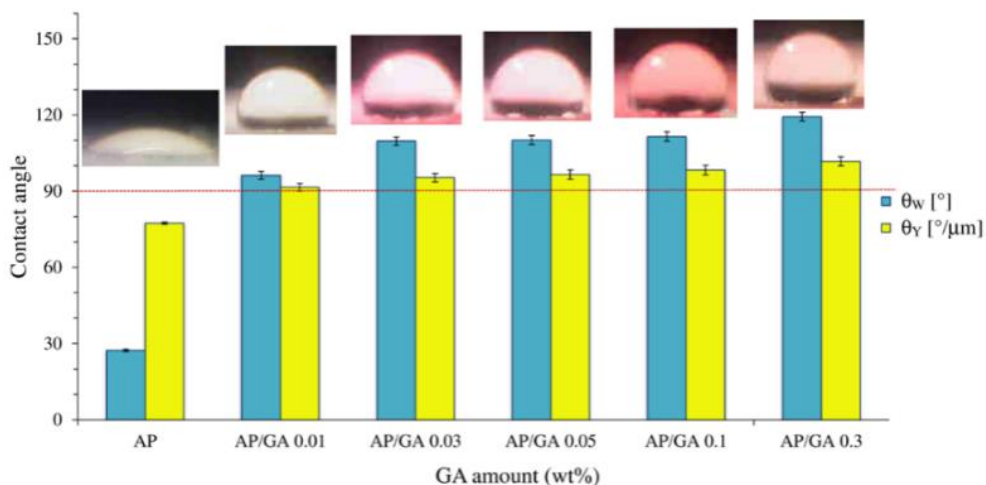


Figure 41. Comparison of contact angles θ_w and θ_Y of AP/GA coatings at the different GA content.

Table 6. Sample code, and Wenzel/ Young contact angles.

Sample code	θ_w (°)	θ_Y (°/μm)
AP	27.34 ± 0.90	77.41 ± 0.90
AP/GA 0.01	96.23 ± 3.02	91.57 ± 3.02
AP/GA 0.03	109.70 ± 3.35	95.37 ± 3.35
AP/GA 0.05	110.11 ± 3.60	96.55 ± 3.60
AP/GA 0.1	111.53 ± 3.70	98.31 ± 3.70
AP/GA 0.3	119.34 ± 3.49	101.75 ± 3.49

When AP and GA molecules start to react with each other, the coating goes from the fluid state, to the gel state and finally to the solid state, as shown in Figure 42 (complex viscosity vs time). Each curve can be distinguished into three parts: an initial plateau (zone I) where the material has the lowest viscosity and a still liquid consistency. A second transition phase (zone II) in which there is a sudden and rapid increase in viscosity up to a further plateau (zone III) in which the material reaches maximum hardening due to solidification after the completion of the cross-linking reaction. From the trend of the various curves, it can be easily seen that there is a marked increase in complex viscosity and a narrowing of the gap between zone I and zone III as the GA content increases. This result is in agreement with the photographic images in Figure 38 which show that the higher glutaraldehyde content leads to a progressive increase in crosslinking speed and time.

Finally, Table 8 also shows the value of the conservative modulus G' after 10,000 seconds of reaction between AP and GA. If 0.1 wt % of GA is added

to the pure APTES, it grows from $\approx 3,800$ Pascal to $\approx 6,300$ Pascal, almost doubling its initial value. Again, the modulus of pure APTES grows further as GA content increases: it increases by one order of magnitude in AP/GA 0.03 and AP/GA 0.05 samples (i.e., 20,569 Pa and 51,776 Pa, respectively), by two orders of magnitude in PA/GA 0.1 ($\approx 200,000$ Pa), and finally, by three orders of magnitude in AP/GA 0.3 (≈ 1 MPa). This results is in agreement with the above discussed complex viscosity results.

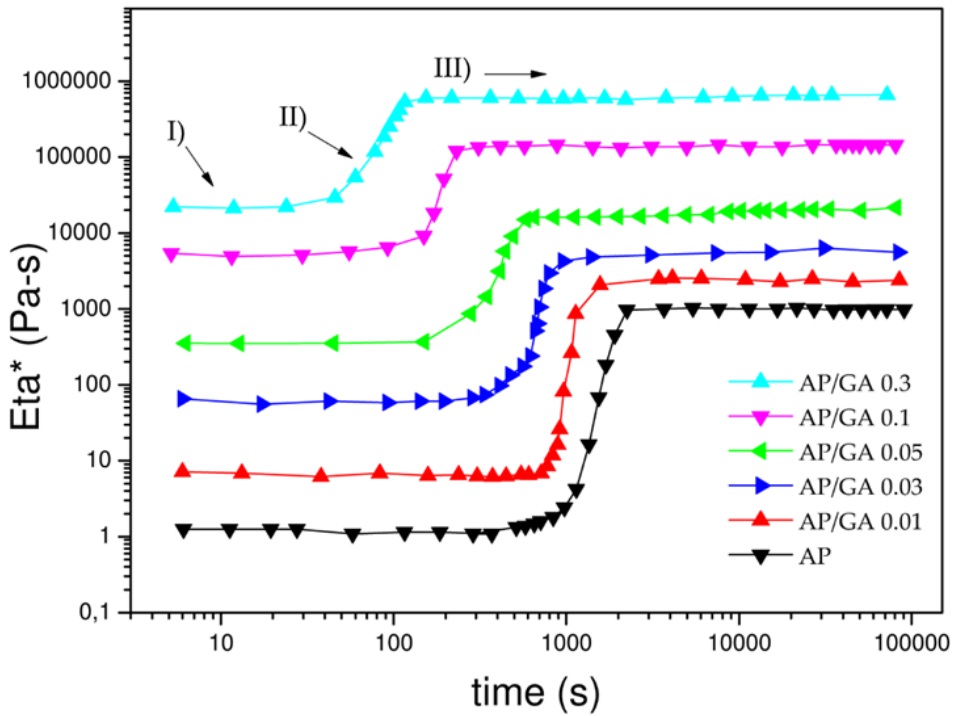


Figure 42. Complex viscosity (η^*) vs time of AP, AP/GA samples.

Table 7. Rheological parameters of the studied coatings.

Sample code	Gel point (Pa)	Time gel point (s)	G' at 10,000 s (Pa)
AP	7.743	6.5691	3,821.04
AP/GA 0.01	232.921	1,647.58	6,229.05
AP/GA 0.03	1,117.603	1,036.202	20,569.88
AP/GA 0.05	13,376.22	696,547	51,776.18
AP/GA 0.1	70,848.82	297.632	236,828.10
AP/GA 0.3	265,307.53	146.82	1,143,717.29

The pull-off method was used to evaluate the mechanical adhesion strength of silica-based coatings with the DH36 steel substrate. The test was performed as reported in Section 5.6.1 and as shown in Figure 43.

The nature and type of fracture from the test surface, was evaluated by visual inspection, according to ASTM D4541-02 or ISO4624:2016.

The AP/GA 0.3 coating breaks at an average tensile stress of 17.38 MPa. Visual inspection of the fracture surface on both sides (dolly/substrate) reveals an average value of material removed from the carriage of about 70% compared to the initial joint still adhered to the carriage. This indicates that the fracture was of “adhesive” type, which occurs at the interface between the dolly and the liner. This type of adhesive fracture was also found for all other sets of samples.

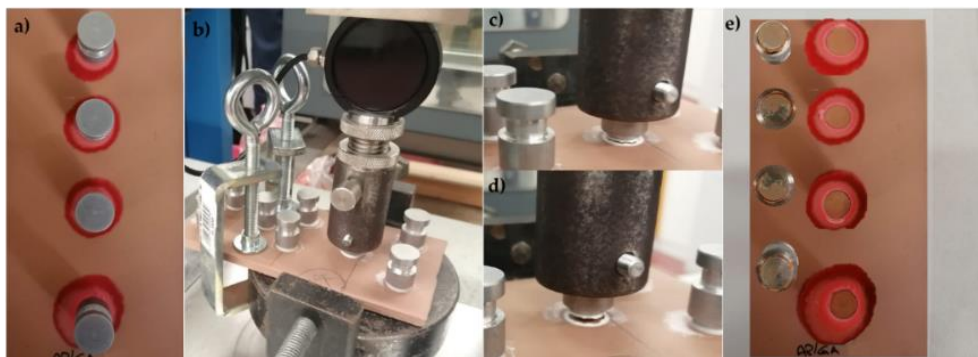


Figure 43. Pull-off Test: Image of the sample AP/GA 0.3 (a); fixing and stretching phase of the dolly in the dynamometer (b); step of breaking the specimen from the metal substrate (c, d); image of the metal specimen and the dolly after the pull off test for the sample AP/GA 0.3

The stress/strain curves of three studied liners are plotted in the graph in Figure 44. The mechanical parameters are detailed in Table 8, where E is the Young's modulus [MPa]; σ_y is the yield stress; $\varepsilon_y\%$ is the yield percentage deformation; σ_{\max} is the maximum stress [MPa]; σ_r is the stress at break [MPa]; $\varepsilon_r\%$ is the percentage deformation at break [%]; L_r is the load at break [N]; W_r is the work at break [J].

The adhesive behavior of the AP and AP/GA 0.01 coating appears to be very close, as both show typical ductile material yielding at 0.11-0.32 MPa and 0.72-1.03% of yield stress and strain, respectively. The yielding disappears in coatings with higher GA contents (≥ 0.05 wt %), as can be seen in the enlarged insert plots.

The highly significant mechanical behavior became that of a stiffer, stronger, and more tenacious coating than pure AP. It is possible to notice how:

-Young's modulus improves from 36-64 MPa, in AP and AP/GA 0.01 coating, respectively, up to 167 MPa in AP/GA 0.3 coating;

-the fracture toughness improves from 0.09-0.27 MPa, in the AP and AP/GA 0.01 coatings, respectively, up to 1.7 MPa in the AP/GA 0.3 coatings;

-the work at break improved from 0.013-0.016 J, in the AP and AP/GA 0.01 coating, respectively, up to 0.21 J in the AP/GA 0.3 coating. The results of the adhesion tests again showed that the presence of glutaraldehyde in the coatings induces a significant change in its mechanical strength, due to the structural change shown by the rheological data. In fact, the presence of GA at the highest load (at AP/GA 0.3) increases the tensile strength and elastic modulus of pure AP by 1788%, and 363%, respectively, compared to pure APTES (see details in Table 8). These pull-off test results confirm as GA improves APTES stiffness and adhesive power of the coating.

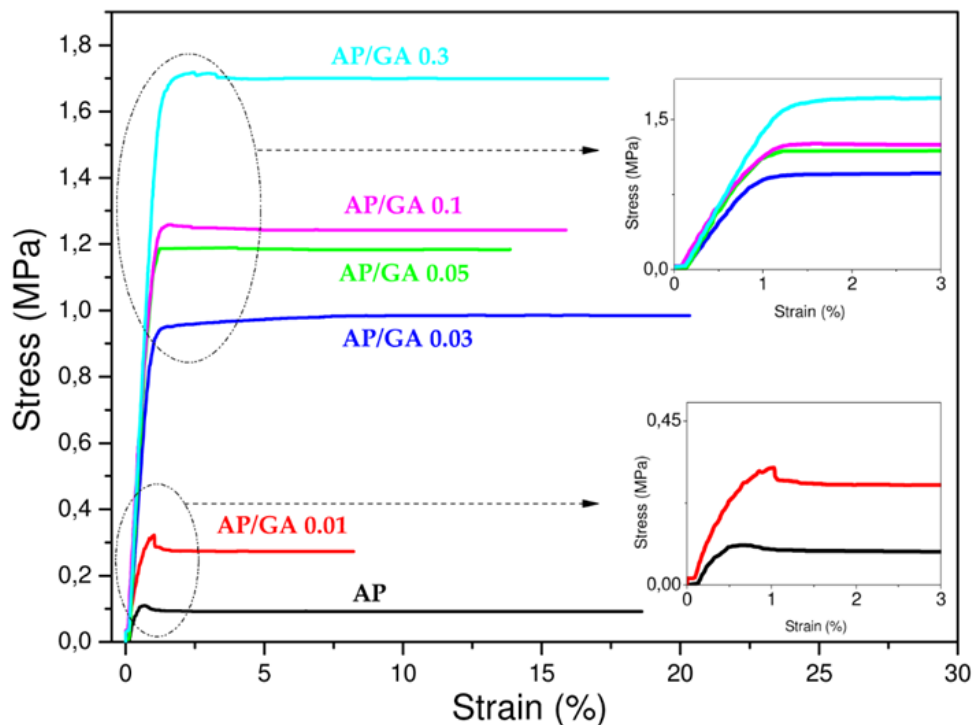


Figure 44. Stress/strain curves of AP and all the AP/GA coatings with a magnification of the yielding area in the inset graphs.

Table 8. Mechanical characterization of AP and AP/GA coatings.

Sample code	E [MPa]	σ_r [MPa]	ϵ_r [%]	L_r [N]	W_r [J]
AP	36.11±2.61	0.09±0.005	18.61±1.50	7.07±0.67	0.0128±0.0001
AP/GA0.01	64.70±3.80	0.27±0.02	8.21±0.48	20.93±1.66	0.0165±0.0001
AP/GA0.03	120.19±9.28	0.99±0.07	20.32±2.06	75.52±7.26	0.1467±0.0002
AP/GA0.05	155.44±11.40	1.18±0.08	13.87±1.03	90.75±5.20	0.1250±0.0001
AP/GA0.1	163.68±13.33	1.24±0.47	15.88±0.28	95.30±10.35	0.1448±0.0001
AP/GA0.3	167.48±11.73	1.70±0.51	17.38±1.09	130.33±7.07	0.2154±0.0001

6. CONCLUSIONS AND FUTURE REMARKS

Aim of this PhD thesis, was to develop biomaterials for the biomedical and environmental fields. Specifically, this PhD thesis is divided into three sections, based on the materials studied, which find their applications in the biomedical and environmental fields: Carbon-based nanomaterials for drug delivery, Chitosan-based hydrogel for tissue engineering and Coatings against Marine Fouling.

GQD, due to their exceptional physical, chemical electrical, optical, and biological properties and the presence of many reactive groups on the surface graphene surface that allow their multimodal conjugation with various functional groups, chemotherapeutic agents, targeting ligands, biocompatible polymers, light-sensitive agents, fluorescent dyes, and functional nanoparticles, represent valuable agents for cancer diagnosis and treatment. As discussed, a GQD-based drug delivery system (DDS) with excellent water dispersibility has been synthesized, and the results obtained represent another step toward more innovative targeted therapies for cancer treatment, opening up new possibilities in the use of poorly water-soluble anticancer drugs with low cellular uptake, systemic toxicity, and undesirable side effects. It was observed that the drug delivery system, GQD-PEG-

BFG@Pyr-RF, exhibited cytotoxic activity against the three cancer cell lines studied with significantly higher potency in alveolar cancer cells than the anticancer drug alone. In addition, the introduction of an ester or phosphonate moiety in green reaction conditions could open new avenues for the use of these nanomaterials for gene and drug delivery, as well as for imaging or for therapeutic purposes.

A new generation of chitosan-based hydrogels was successfully synthesized by first coupling the biopolymer matrix with hydroxyapatite and/or magnetite via the *in situ* precipitation technique and using the biocompatible genipin as cross-linking agent. The obtained results revealed that all surfaces of the scaffold support cell attachment and proliferation, confirming the non-toxic nature of the scaffolds over time, demonstrating superior bioactivity and making these scaffolds as suitable and promising material for guided bone growth. In particular, the composite based on chitosan/hydroxyapatite/magnetite demonstrated superior bioactivity, making it a suitable and promising material for guided bone growth.

The chitosan biopolymer matrix was also functionalized with hyperbranched PAMAM dendrimer moieties with different sizes and with well-dispersed hydroxyapatite. It was demonstrated that the chitosan-

dendrimer-hydroxyapatite hydrogels are capable of coupling the known osteoconductive properties of hydroxyapatite with the drug release behavior and good processability of chitosan-dendrimer hydrogels, opening up new approaches in the field of tissue engineering based on biopolymer scaffolds. In particular, the CS/D3.5/HA sample showed improved thermal stability, a higher amount of released ketoprofen compared to the unmodified chitosan-based hydrogels due to the spacer effect of the dendrimeric structures between the chitosan chains, and from the rheological properties point of view, it showed an increase in strength and viscosity as a result of lowering the mutual movement of the biopolymer chains due to the steric hindrance of the dendrimer.

Furthermore, POSS silica cage functionalization was also exploited to afford substrates containing functional groups suitable for covalent binding to the chitosan structure. *In vitro* drug release studies and preliminary biological tests preliminary biological tests performed on osteoblast cultures, demonstrated the ability of the system to release drugs in a controlled manner and the lack of cytotoxicity of the hybrid material. The pure CS hydrogel exhibits burst drug release (approximately 65%) within 1 hour that reached 100% drug release within 1 day. For the CS-POSS hydrogel, the

release curve also showed a rapid release of large amounts of ketoprofen (45%) in the first hour but a more controlled release over the next 2 days, reaching a plateau at approximately 78% of loaded ketoprofen. The results of this study suggest the presence of specific intermolecular interactions between the functionalized silica cage and the drug and open up new possibilities for long-term sustained release of drugs trapped within the polymer matrix during its biodegradation *in vivo*.

In the field of protective coatings against biofouling, materials based on APTES have been prepared, with the aim of overcoming the problems of the mechanical properties of the well-known PDMS. The synthesized coatings, in particular the sample AP/LA and AP/GA 0.3 have been found to be the best performing in terms of adhesion, wettability, rheological properties and thermal stability. The AP/LA sample shows a contact angle (θ_w) of 144.89° which correlated to the roughness (θ_y) becomes 176.05° , and in terms of adhesion, the Young's modulus equal to 154 MPa, compared to 36 MPa of the pure AP sample. A contact angle (θ_w) of 119.34° was calculated for the AP/GA 0.3 sample versus 96.23° for the AP/GA 0.01 sample, in terms of adhesion, Young's modulus equal to 167 MPa versus 36-64 MPa, in AP and AP/GA 0.01 coating.

Further studies will be aimed at the optimization of these systems, especially regarding the development of multifunctional coatings able to combine different design properties in a single coating. Finally, in order to evaluate the resistance against marine fouling, biological assays will be performed.

7. EXPERIMENTAL SECTION

E.S.1 Materials and methods

All reagents and starting materials were purchased from commercial suppliers and were used without further purification. The MWCNTs used for GQDs synthesis were obtained by catalytic chemical vapour deposition (CCVD) starting from isobutane as the carbon source and using Fe/Al₂O₃ as the catalyst. The purification procedure gave pristine MWCNTs with >95% purity. GQDs were obtained from MWCNTs by treatment with a 1:3 ratio mixture of HNO₃/H₂SO₄.

E.S.1.1 Chemical, Physical, and Morphological Characterization

¹H NMR spectra were recorded on a Varian instrument operating at 500 MHz, and chemical shifts were reported in ppm relative to TMS as a standard. Thin-layer chromatography was done using Merck silica gel 60-F254 pre-coated in aluminium plates, and preparative separations were performed by flash chromatography with Merck silica gels of 0.063-0.200 mm and 0.035-0.070 mm. GQDs morphology was investigated by high-resolution transmission electron microscopy (HRTEM) using a JEOL JEM 2010 analytical electron microscope (LaB6 electron gun), operating at 200 kV, equipped with a Gatan 794 Multi-Scan CCD camera for digital imaging. Samples for TEM analyses were obtained by placing a few drops of GQD, dispersed in isopropanol, on 400 mesh carbon-coated copper grids. Thermogravimetric investigations were performed on a TA Q500 instrument, at 10 °C/min, 100 to 1000 °C, in argon. Zeta potential measurements and titration analyses were performed using the Zeta sizer 3000 instrument (Malvern). Titration analyses were performed over the

range of pH values 6-8. Infrared spectra were obtained using the Perkin-Elmer 2000 Fourier transform infrared (FT-IR) spectrometer using the KBr pellet method. Photoluminescence (PL) measurements were performed using a NanoLog Horiba modular spectrofluorometer under excitation of a xenon lamp at room temperature. GQD-based samples were prepared at a concentration of 100 ng/mL. Micro Raman measurements were obtained in reflection mode by exciting the samples with a solid-state laser at $\lambda_{\text{exc}} = 470$ nm. The purity of the Pyr-RF sample was determined by HPLC (Varian ProStar 325) equipped with a C-18 bound phase column (Waters, XTerra C18 MS, 3.5 μm , 4.5 \times 50 mm). Gradient elution was performed with acetonitrile and water as the mobile phase and was monitored at 254 nm.

E.S.1.2 Synthesis of GQD

GQDs were synthesized from pristine Multi-Walled Carbon Nanotube (MWCNT) by treatment with a solution of $\text{HNO}_3/\text{H}_2\text{SO}_4$ in a 1:3 ratio. The suspension was placed in a reaction vessel at 60 °C for 4 days under reflux. After dilution with deionized water, the mixture was filtered using a 0.1 mm Millipore membrane under vacuum. Then, the filtrate was treated with a NaOH solution to neutral pH and subjected to centrifugation at 3000 rpm. The resulting mixture was diluted with deionized water and purified using a dialysis bag with a molecular weight (MW) of 12,000 Da.

E.S.1.3 Synthesis of GQD-PEG

A solution of GQDs (6 mg) in DMF (10 mL) was treated with *N*-(3-dimethylaminopropyl)-*N'*-ethylcarbodiimide hydrochloride (EDC·HCl, 3 mg, 0.016 mmol) and triethylamine (ETA, 2.2 L, 0.016 mmol), and the mixture was allowed to stir at room temperature for 15 min. Then, hydroxy

benzotriazole (HOBt, 2.2 mg, 0.016 mmol) and a catalytic amount of 4-dimethylaminopyridine (DMAP) were added to the mixture, which was allowed to stir for 1 h. The suspension was then treated with 10.3 mg of *O*-(2-aminoethyl)-*O'*-[2-(BOC-amino) ethyl] decaethylene glycol (0.016 mmol) and allowed to stir at room temperature for 4 days. The obtained residue was diluted with deionized water and purified using dialysis bags with a MW of 12,000 Da for 8 h. The BOC-protective group was subsequently removed by treating the mixture with HCl (4 M) in dioxane for 1 h at room temperature, resulting in the GQD-PEG sample.

E.S.1.4 Synthesis of GQD-PEG-BFG

A solution of potassium *tert*-butoxide (0.046 mmol) in 5 mL of THF was allowed to stir for 1 min at room temperature. Then, BFG (6 mg, 0.023 mmol) and dispersion of GQD-PEG (6 mg) in pure water were added, and the mixture was left to stir at room temperature for 1 h. After removal of THF, under vacuum, the mixture was diluted with water and purified using a dialysis bag (MW of 12,000 Da) for 8 h.

E.S.1.5 Synthesis of Pyr-RF

A solution of riboflavin (15 mg, 0.04 mmol) in CH₂Cl₂ (20 mL) was treated with EDC·HCl (7.6 mg, 0.04 mmol) and ETA (5 L, 0.4 mmol), and the solution was allowed to stir at room temperature for 15 minutes. Next, DMAP (4.8 mg, 0.04 mmol) and HOBt (4 mg, 0.04 mmol) were added, and the mixture was stirred for an additional hour. Finally, 12 mg of 1-pyrene butyric acid (0.04 mmol) was added, and the suspension was left under magnetic stirring for 5 days at room temperature. The mixture was then extracted with CH₂Cl₂ (3 50 mL), and the organic layers were dried with MgSO₄ and concentrated,

under vacuum, obtaining the crude product. Purification by medium-pressure liquid chromatography (MPLC) on a silica gel column using a mixture of CH₂Cl₂/CH₃OH (98:2) as eluent yielded the pure conjugated compound 5-(7,8-dimethyl-2,4-dioxo-3,4-dihydrobenzo[g]pteridin-10(2H)-yl)-2,3,4-trihydroxypentyl-5-(pyren-1-yl)pentanoate (Pyr-RF) with 98% purity as determined by HPLC analysis. ¹H NMR (300 MHz, CDCl₃) δ = 8.72 (br s, 1H), 8.12 (d, 1H, *J* = 7.4 Hz), 7.83-7.68 (m, 9H), 6.85 (s, 1H), 6.40 (s, 1H), 4.46 (dd, 1H, *J* = 11.92, 6.8 Hz), 4.08-3.89 (m, 2H), 3.87-3.83 (m, 1H), 3.80-3.75 (m, 3H), 3.70-3.66 (m, 2H), 3.06-2.98 (m, 2H), 2.36-2.33 (m, 5H), 2.26 (s, 3H), 1.75-1.68 (m, 4H). (Fig. S1)

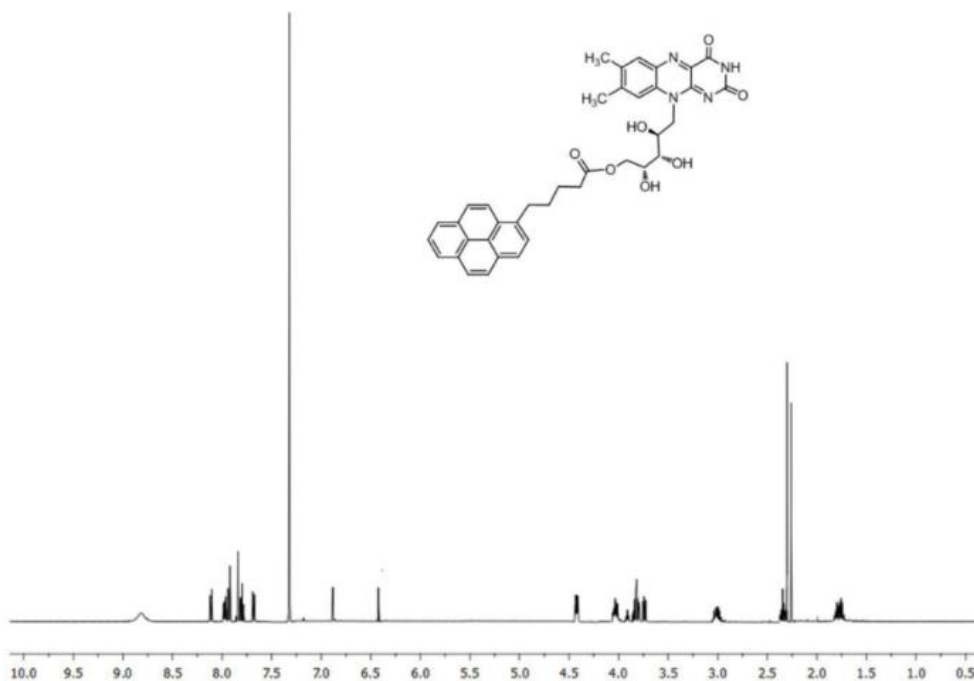


Figure S1. ¹H NMR spectrum of Pyr-RF sample.

E.S.1.6 Synthesis of GQD-PEG-BF@Pyr-RF and GQD-Pyr-RF

A solution of GQD-PEG-BFG (10 mg) or GQD (10 mg) in phosphate buffered saline (PBS) pH 7.4 (5 mL) was treated with a solution of Pyr-RF (10 mg) dissolved in 5 mL of PBS at room temperature for 5 days. The amount of Pyr-RF bound to the GQD surface was found to be of 19.2 wt % for GQD-PEG-BFG@Pyr-RF and of 8.5% for GQD-Pyr-RF. (Fig. S2)

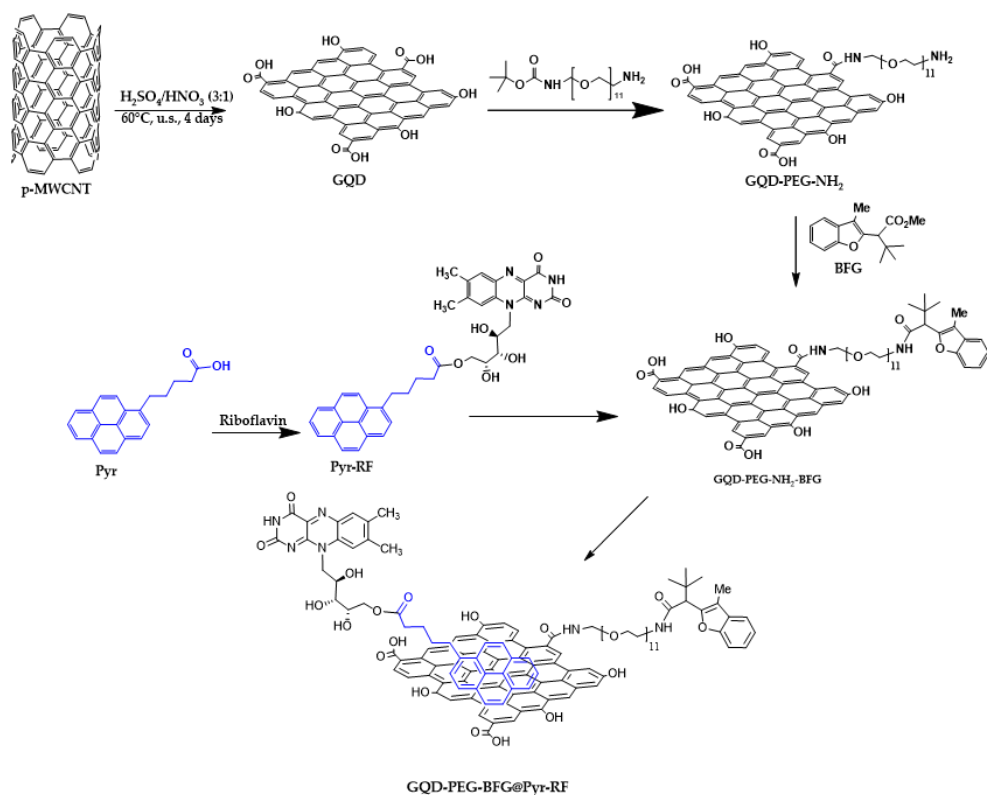


Figure S2. Synthesis of GQD-PEG-BF@Pyr-RF.

E.S.1.7 Synthesis of *C*-(diethoxyphosphoryl) propylidene, *N*-benzyl nitron 1b

Triethylphosphite (5 mL, 28.9 mmol) was added dropwise to an excess of neat 2-(2-bromoethyl)-1,3-dioxolane 3 (6.5 mL, 57.8 mmol) at room temperature and under argon. Then, the mixture was heated up to 110°C until the NMR analysis of the reaction mixture confirmed the complete disappearance of triethyl phosphite. The diethylethylphosphonate derivative pale oil 4 was obtained by distillation, through a Vigreux column under reduced pressure, of the crude reaction mixture (yield 58%). ^1H NMR (CDCl_3) δ = 4.95 (t, J = 4 Hz, $\text{PCH}_2\text{CH}_2\text{CHO}$, 1H), 4.06–4.15 (m, OCH_2CH_3 , 4H), 3.84–3.99 (m, $\text{OCH}_2\text{CH}_2\text{O}$, 4H), 1.79–2.00 (m, PCH_2CH_2 , 4H), 1.32 (t,

$J = 7$ Hz, OCH_2CH_3 , 6H); ^{13}C NMR (75.5 MHz; CDCl_3) $\delta = 103.7$ (d, $^3\text{JP-C-C-C} = 19$), 65.5, 61.9 (d, $^2\text{JP-O-C} = 6$ Hz), 27.3 (d, $^2\text{JP-C-C} = 4$ Hz), 19.9 (d, $^1\text{JP-C} = 144$ Hz), 16.8 (d, $^3\text{JP-O-C-C} = 6$ Hz).

An aqueous HCl 2 M and acetone 10:1 v:v solution (50 mL) of diethyl [2-(1,3-dioxolan-2-yl)ethyl]phosphonate 4 (3 g, 12.6 mmol) was heated for 3 h at 50 °C. Then, after cooling, the reaction mixture was extracted using CH_2Cl_2 (3x50 mL); the organic layers were dried over MgSO_4 and concentrated under vacuum to give the aldehyde 5 as a pale oil (88% yield) that was used for the successive reaction without any further purification. To a solution of sodium acetate (1.2 g, 15 mmol) in CH_2Cl_2 (30 mL), cooled at 0 °C, were added the N-benzyl hydroxylamine hydrochloride (24 g, 15 mmol) and successively the aldehyde 5 (2 g, 10 mmol) dropwise. The reaction mixture was then stirred for 1 h at 0 °C and then at room temperature overnight. After this time, the solvent was removed under reduced pressure and the residue was purified by silica gel flash chromatography ($\text{CHCl}_3/\text{MeOH}$ 95:5) to give the pure nitrone 1b (yield 95%). ^1H NMR (500 MHz, CDCl_3) $\delta = 7.47$ – 7.11 (m, H-benzen + $\text{PCH}_2\text{CH}_2\text{CH}$, 6H), 4.17–3.91 (m, PhCH_2 + OCH_2CH_3 , 6H), 3.11–2.91 (m, $\text{PCH}_2\text{CH}_2\text{CH}$, 2H), 1.98–1.74 (m, PCH_2CH_2 , 2H), 1.36–1.19 (m, OCH_2CH_3 , 6H). ^{13}C NMR (125 MHz, CDCl_3) $\delta = 139.5$ (d, $^3\text{JP-C-C-C} = 9$ Hz), 137.3, 129.8, 128.2, 128.1, 69.0, 61.6 (d, $^2\text{JP-O-C} = 6$ Hz), 34.5 (d, $^2\text{JP-C-C} = 7$ Hz), 26.8 (d, $^1\text{JP-C} = 94.9$ Hz), 16.3 (d, $^3\text{JP-O-C-C} = 6$ Hz).

E.S.1.8 Synthesis of isox-GQDs 2a and isox-GQDs 2b

An aqueous solution of GQDs (30 mg/30 mL) was treated with a mixture of GA/TMG in a 2:1 molar ratio (2 mL). Then, after removal of water under reduced pressure, 300 mg of nitrone 1b or 2b was added and the mixture was heated under microwave irradiation for 1 hour at 90 °C, 150 W. The resulting suspension was diluted with deionized water and then purified by dialysis

for 2 days, using a dialysis bag (MW of 12,000 Da). The presence of nitrons 2a or 2b was confirmed by ^1H NMR characterization.

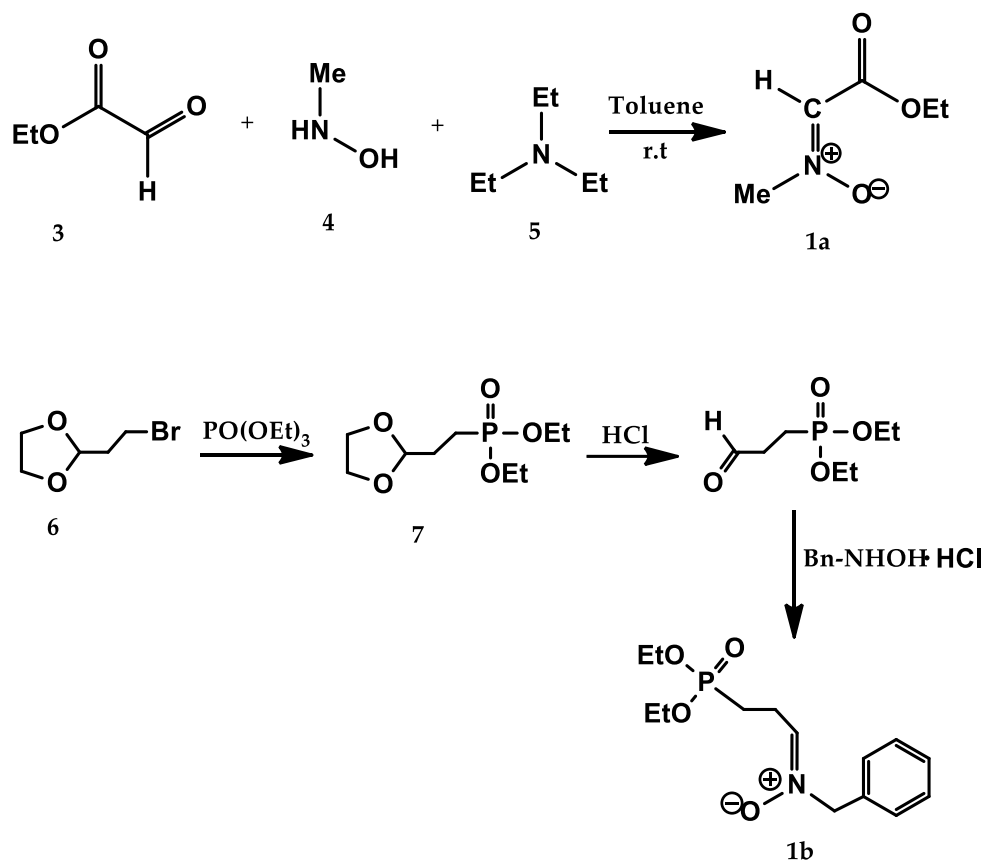


Figure S3. Synthesis of nitron 1a and 1b.

E.S.2 Materials and methods

The reagents chitosan (medium molecular weight, deacetylation 75%–85%), acetic acid (99.9%), hydroxyapatite (99%), calcium nitrate tetrahydrate (99%), ammonium phosphate dibasic (99%), iron (II) chloride (99%), iron (III) chloride (99%), ethylenediamine (99.5%), methyl acrylate (99%), calcium nitrate tetrahydrate (>99%), potassium tert-butoxide (>98%), methanol (99%), tetrahydrofuran (>99%), ammonium phosphate dibasic (>98%), ammonia solution (>99.5%), allyl-heptaisobutyl-POSS (>99.5%), vinyl-heptaisobutyl POSS (>99.5%) and ketoprofen (>99%), were purchased from Sigma Aldrich (St. Louis, MO, USA); genipin (>98%) was purchased from Carbosynth (St. Gallen, Switzerland). All reagents and solvents were used without further purification. NMR spectra were recorded on a Varian Unity Inova instrument operating at 500MHz and chemical shifts were reported in ppm (σ) using TMS as internal standard. The infrared spectra were obtained using a Fourier-Transform Infrared (FT-IR) spectrometer VERTEX 80/80v (Bruker Optik GmbH, Ettlingen, Germany), by the method of KBr pellets in the range of 4000–500 cm^{-1} . X-ray diffraction (XRD) experiments were performed using a BrukerD8 Advance diffractometer (Bruker, Karlsruhe, Germany) at room temperature with a Bragg–Brentano theta-2theta configuration and Cu Ka radiation (40 V, 40 mA). The XRD patterns were collected in the range 10°–60° with a step of 0.2 °/s. The obtained diffraction peaks were compared with those in the Joint Committee on Powdered Diffraction Standards (JCPDS) database. Thermogravimetric analyses (TGA) were performed using a TAQ500 instrument (TA Instruments, New Castle, DE, USA) from 100 to 700 °C, with a rate of 20 °C per minute, under an air atmosphere. Optical images

were recorded by means of a Hirox digital microscope, mod. KH8700 (Hirox, Tokyo, Japan) by mounting a MX(G)-5040Z lens at room temperature. Rheological property measurements were carried out by means of a rotational rheometer (Mod. SR5, Rheometric scientific, Piscataway, NJ, USA) with parallel plate geometry at 37 °C. UV spectra have been performed by a Thermo Nicolet mod., Evolution 500 spectrophotometer, measuring the drug absorbance at 260 nm.

E.S.2.1 Synthesis of CS Sample

240 mg of chitosan powder was dissolved in an aqueous solution of 2% acetic acid for 30 min at 45 °C. Afterwards, 24 mg (0.1 mmol) of genipin or 0.33 mg was slowly added into the mixture.

E.S.2.2 Synthesis of CS/HA Samples

240 mg of chitosan was dissolved in an aqueous solution of 2% acetic acid for 30 min at 45 °C. Subsequently, 1.56 mmol of $\text{Ca}(\text{NO}_3)_2 \cdot 4\text{H}_2\text{O}$ and 0.5 mmol of $(\text{NH}_4)_2\text{HPO}_4$ was added under vigorous agitation. The solution was stirred for 30 min until the calcium and phosphate salts were entirely dissolved. After this, 24 mg (0.1 mmol) of genipin was slowly added into the mixture. The formed CS/HA composite was treated with a 2% NH_3 solution for 1 h at room temperature and then was rinsed with deionized water until reaching pH 7. CS/HA sample starting from HA powder (240 mg) incorporated in chitosan during the cross-linking step was also synthesized.

E.S.2.3 Synthesis of CS/HA/MGN Samples

The same process as for the CS/HA samples above was followed until the calcium and phosphate salts were completely dissolved. Then, 24 mg (0.1 mmol) of genipin was slowly added into the solution that now also contained

FeCl₂ (0.04 mmol) and FeCl₃ (0.09 mmol) to produce the CS/HA/Fe₃O₄ composite scaffolds. These were subsequently treated with a 2% NH₃ solution for 1 h at room temperature and then rinsed with deionized water until reaching pH 7. Additionally, CS/HA/MGN sample was prepared from HA/Fe₃O₄ co-precipitated powders (240 mg) that were synthesized by a previously described procedure and incorporated into chitosan during the cross-linking as above.

E.S.2.4 Synthesis of PAMAM Dendrimers and Chitosan–PAMAM Chains

Chitosan chains functionalized with poly-(amidoamine) dendrimers (PAMAM) were synthesized from PAM-CO₂Me dendrimers of generation 1.5, 2.5, and 3.5 that were produced by repetition of two processes: (a) Michael addition of methyl acrylate (MA) to the amino groups of the initiator core ethylenediamine(EDA) and (b) amidation reaction of ester moieties with the amino groups of EDA. Briefly, Michael addition was performed by reaction of EDA (6 g, 0.1 mol) with MA (86 g, 1.0 mol) at 0 °C under vigorous agitation for 10 min. Then, methanol (100 mL) was added, the mixture temperature was allowed to rise to room temperature, and the mixture was left under stirring for 24 h. The solvent and the excess of MA were removed under vacuum at 50 °C, yielding the methyl-ester-terminated PAMAM with generation 0.5 (G0.5). Then, EDA (13 g, 0.22 mol) was carefully added to the solution of PAMAM G0.5 (10 g, 0.024 mol in methanol (200 mL) at 0 °C and the mixture was left stirring for 72 h at room temperature. The solvent and the excess EDA were removed under reduced pressure at 70 °C to afford the PAMAM dendrimer G1.0. The

Michael and amidification reactions were, step by step, repeated, to obtain the methyl-ester-terminated PAMAM dendrimer with generation G1.5, G2.5 and G3.5. After removal of the solvent and the excess MA, under vacuum at 50 °C, the samples were characterized by FTIR and ^1H NMR and used for the subsequent conjugation with chitosan without further purification (^1H NMR (500 MHz, CDCl_3 , ppm) δ H: 3.66 (48H, s), 3.28–3.26 (24H, m), 2.77–2.74 (60H, m) 2.49–2.42 (80H, m)). Each of the so-formed dendrimers of PAMAM- CO_2Me was treated with a solution of potassium tert-butoxide (80 mg, 0.71 mmol) in 5 mL of THF and was left under stirring in air for 1 min at room temperature. A dispersion of chitosan (1 g) in deionized water (5 mL) was then added to each mixture containing the different generation of dendrimer (0.35 mmol), which was left to stir at room temperature for 2 h. Then, after removal of the solvent under vacuum, the mixture was diluted with water and purified using a dialysis bag (MW of 12,000 Da) for 8 h. (^1H NMR (500 MHz, D_2O , ppm) δ H: 5.0 (CS-H1, m), 3.94–3.92 (CS-H2, CS-H6, m), 3.85–3.71 (CS-H3, CS-H4, CS-H4, m), 3.65 (PAMAM, s), 3.26–3.25 (PAMAM, m), 2.76–2.74 (PAMAM, m) 2.53–2.40 (PAMAM, m), 1.85 (CS-C(O)CH₃, s)).

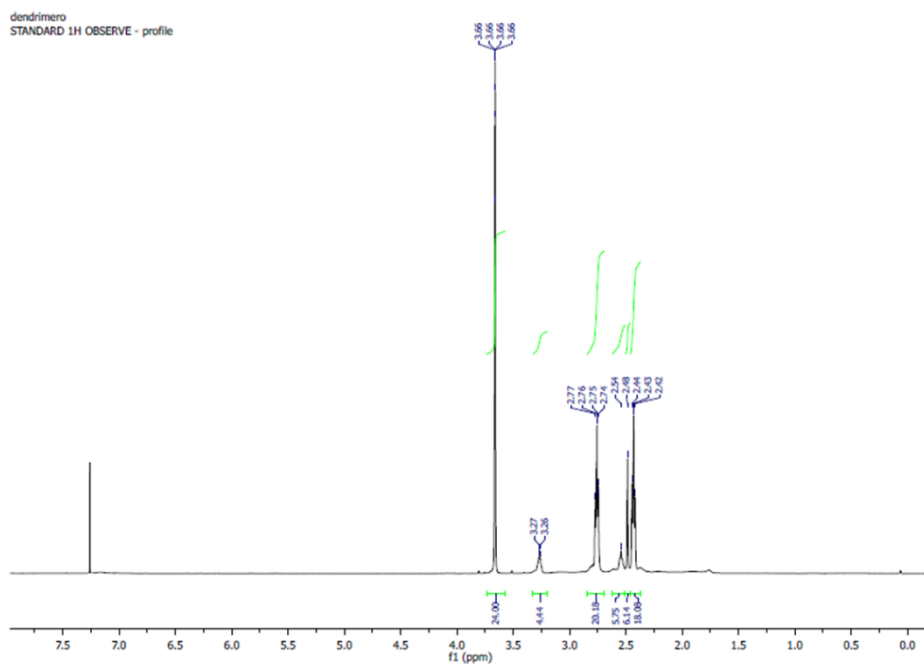


Figure S4. ^1H NMR spectrum of poly(amidoamine) dendrimers (PAMAM)

E.S.2.5 Synthesis of Ketoprofen-Doped Hydrogel (CS-HA-Keto and CS-D1.5-HA-Keto, CS-D2.5-HA-Keto, CS-D3.5-HA-Keto Samples)

CS-HA and ketoprofen-doped CS-D1.5-HA, CS-D2.5-HA, and CS-D3.5-HA hydrogels were synthesized by adding ketoprofen lysine salt (160 mg, 0.67 mmol) dissolved in 2 mL deionized water to the mixture before the addition of genipin. The ketoprofen-doped hydrogels were rinsed with deionized water until the disappearance of the drug in the wash solutions as assessed by NMR analysis, and the samples were dried at 37 °C for 24 h at a vacuum drying pressure of 65 mbar until constant weight. The amount of ketoprofen present in the hydrogels was calculated as the difference between the initial amount of drug dispersed in the mixture during hydrogel formation and the amount of unbound drug present in the filtrate after washing procedures,

and this value was also confirmed after drug release studies. The drug concentration was found to be 4 wt%.

E.S.2.6 Synthesis of isoxazolidinyl-POSS 3a, b, 4a, b and 5b.

A mixture of nitron 1 (200 mg, 1.52 mmol) and allyl-heptaisobutyl POSS (132 mg, 0.15 mmol) 2a or vinyl-heptaisobutyl POSS (128 mg, 0.15 mmol) 2b, dissolved in toluene (2 mL) was reacted for 90 min at 100 W under microwave irradiation at an internal temperature of 100-110 °C. The mixture was then evaporated and the resulting solid was purified by flash chromatography on silica gel using cyclohexane/ethyl acetate (80 : 20) as eluent, to afford isoxazolidines 3a, 4a from allylheptaisobutyl POSS 2a and isoxazolidines 3b, 4b and 5b from vinyl-heptaisobutyl POSS 2b.

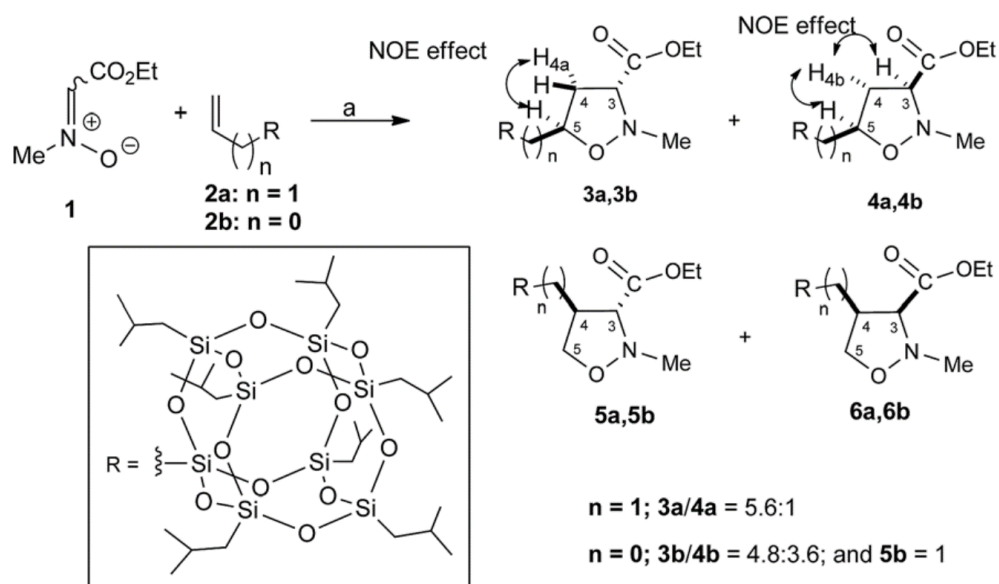


Figure S5. Synthesis of isoxazolidinyl-POSS 3a, 4a, 3b, 4b and 5b. Reagents and conditions: toluene, 100 W, 110 °C, 90 min. [(3a: 85%; 4a: 15% yield); (3b: 48.0%, 4b: 36.0% and 5b: 10.0% yield)].

E.S.2.7 Synthesis of CS-POSS hybrid.

A solution of potassium *tert*-butoxide (80 mg, 0.71 mmol) in 5 mL of THF was left under stirring in air for 1 min at room temperature. Then, compound 3a was added to the dispersion (175 mg, 0.17 mmol) which left under stirring at r.t. for 1 h. Then, a dispersion of chitosan (350 mg, medium molecular weight) in deionized water (5 mL) was added to the mixture, which was left to stir at r.t. for another 2 h. After vacuum solvent removal, the mixture was purified using a dialysis bag (MW of 12 000 Da) for 8 hours. After removal of water under vacuum at 50 °C, the mixture was dried at 50 °C for 24 h at the vacuum drying pressure of 65 mbar.

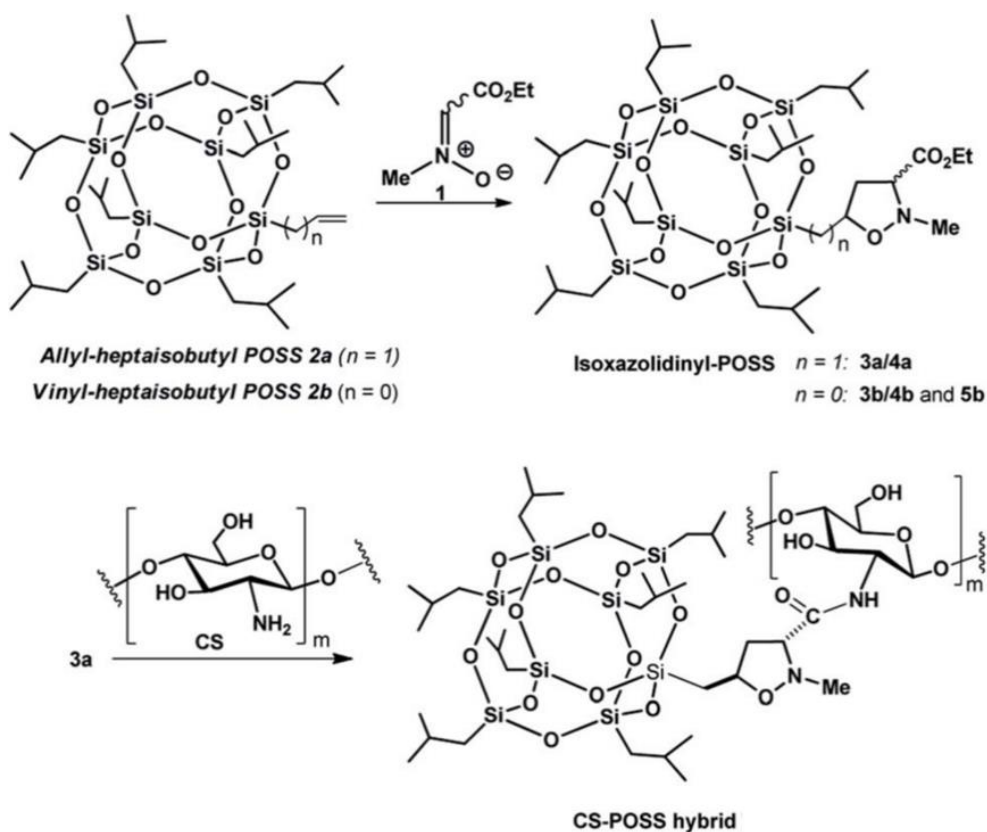


Figure S6. Synthesis of CS-POSS hybrid.

E.S.2.8 Synthesis of CS and CS-POSS Hydrogels.

CS and CS/POSS hydrogels were prepared following the same procedure as reported in section E.S.2.1.

E.S.3 Materials and methods

The reagents (3-aminopropyl)-triethoxysilane (98%) (AP), propionaldehyde (97%) (PP), lauraldehyde ($\geq 95\%$) (LA), hydrochloric acid (37%), and glutaraldehyde solution (25% in H₂O) (GA) were purchased from Sigma Aldrich (St. Louis, MO, USA). All reagents and solvents were used without further purification.

E.S.3.1 Characterization and Testing

The surface roughness (R_a) was calculated by the portable and compact roughness tester, SurfTest SJ-210- Series 178 (Mitutoyo S.r.l., Milan, Italy):

$$Ra = \frac{1}{N} \sum_{i=1}^n |Y_i| \quad (1)$$

where R_a represents the arithmetic mean of the absolute values of the deviations of the evaluation profile (Y_i) from the mean line. The measurement conditions were setted according to the JIS2001 roughness standard, five sampling lengths, lengths of cut-off ($\lambda_s = 2.5 \mu\text{m}$, $\lambda_c = 0.8 \mu\text{m}$) and a stylus translation speed of 0.5 mm/sec. On average, n. 4 roughness profiles per type of sample were performed and then an average profile was obtained.

Thermogravimetric analysis (TGA) was performed using the TAQ500 instrument (TA Instruments, New Castle, DE, USA), under argon flow at a flow rate of 100 ml/min. All samples tested, after a vacuum drying procedure, were heated up to 800 °C with a heating rate of 20 °C/min.

Differential Scanning Calorimetry (DSC) was performed using the TAQ500 instrument (TA Instruments, New Castle, DE, USA), under nitrogen flow at

a flow rate of 50 ml/min, from room temperature to 550 °C, with a heating rate of 10 °C/min and water cooling.

The wet ability of the samples was evaluated by the contact angle “theta” (θ) measurement (according to the international standard ASTM D7334), (Prototype, Messina, Italy), by depositing a drop of deionized water of 1 μ l on the horizontal surface of the sample, by means of a micro lithic syringe (Hamilton, 10 μ l). Contact angle θ have been evaluated by the sessile drop method (ASTM D7334):

$$\theta_w = 2\arctg\left(\frac{2h}{d}\right) \quad (2) \quad ; \quad \theta_Y = \arccos\left(\frac{\cos\theta_w}{r}\right) \quad (3)$$

where d are the diameter and h are the height (both in mm) of the drop, θ_w is the Wenzel angle apparent dependent on the roughness of the surface, r is the surface roughness, and θ_Y is the Young contact angle of equilibrium on perfectly smooth surface.

These measurements have been performed on coatings deposited on DH36 steel metal substrate previously coated with a commercial primer Jotacote Universal N10 two-component epoxy with polyamine hardener (3:1), and tie coat Safeguard Universal ES, a two-component epoxy vinyl with a polyamide hardener (5:1) (supplied by Jotun Italia Srl). For each coating, the resulting contact angle is the average value of approximately 10-20 measurements made with deionized water.

Rheological property measurements were carried out by means of a rotational rheometer (Mod. SR5, Rheometric scientific, Piscataway, NJ, USA) with parallel plate geometry at room temperature.

A dynamic stress sweep test (frequency of 1 Hz) was performed within the stress range of 0.5 Pa–1000 Pa, to check the linear viscoelastic region (LVR), in which the stored elastic modulus, G' , and the viscous loss modulus, G'' , are independent of the applied shear stress. From these tests, a stress value of 50 Pa was chosen for the AP/PP and AP/LA samples, and a stress value of 4 Pa was chosen for the AP/GA samples, within the LVR, to test the coatings, and according to literature data. Thus, frequency sweep tests (in stress control) were carried out in the frequency range 0.01–200 rad/sec at the constant stress value of 50 or 4 Pa. The rheological properties (frequency response of G' and of G'') were checked 30 min after the cross-linking beginning. Each test was carried out in duplicate.

The adhesion test was performed were conducted by a Lloyd LR10K universal testing machine (Ametek-Lloyd Instruments Ltd, Fareham Hampshire, UK), in accordance with ASTM D4541-02 (or ISO4624:2016) by attaching steel metal dolly, perpendicularly on DH36 steel metal samples (80x10 mm, thickness 5 mm). DH36 steel samples have been fully coated with a thin layer (of about 323.17 μm micron) of commercial primer (Jotacote Universal N10, Jotun Italia Srl) and tie coat (Safeguard Universal ES, Jotun Italia Srl) on which was deposited a layer thin of coatings as topcoat (of about 190 μm). The dollies, before adhering to the coating, were rubbed, and cleaned with a cotton swab dipped in alcohol and then dried with a dry cloth. The following experimental conditions were used, according to the use of the LLOYD LR10K machine: Load cell 10KN, Preload 1.00 N, Speed 1mm/min, Diameter \approx 9.88 mm, Breakage: load yields up to 20%. For the investigation to be statistically valid and therefore correctly carried out, three sample (for

each type) of at least six dollies was extracted, then the average of the values detected was carried out.

E.S.3.2 Synthesis of AP/PP and AP/LA coatings

Schiff base formation reactions were conducted by reacting 1 ml of APTES (0.0045 mol) with 0.16 ml of PP (0.5 eq, 0,13 mol) and 0.5 ml of LA (0.5 eq, 0,42 mol) in a closed vial, in the absence of solvent, at 110°C for one hour. Upon completion of the reaction, the obtained compounds were treated with a H₂O/HCl hydrolysis mixture. After that, the samples were applied on the glass supports, previously activated with a solution constituted of H₂SO₄/H₂O₂ in a 3:1 ratio and left to crosslink for the next 12 hours.

E.S.3.3 Synthesis of AP/GA coatings

APTES/Glutaraldehyde samples (AP/GA) with different AP:GA ratio was synthesized fixing the amount of APTES to 1 mL of APTES (0.0045 mol) and varying the amount of GA to 0.3 mL (0.00075 mol), 0.1 mL (0. 00025 mol), 0.05 mL (0.00013 mol), 0.03 mL (0.00008 mol), 0.01 mL (0.0000275 mol); solutions of APTES and glutaraldehyde were maintained at room temperature under magnetic stirring for 30 minutes. After that, the samples were applied on the glass supports, previously activated with a solution constituted of H₂SO₄/H₂O₂ in a 3:1 ratio and left to crosslink for the next 12 hours yielding in order the samples AP/GA 0.3, AP/GA 0.1, AP/GA 0.05, AP/GA 0.03 and AP/GA 0.01.